DESIGN AND ASSESSMENT OF FLOW-THROUGH CATALYTIC SYSTEM USING PALLADIUM NANOPARTICLE CATALYST CONFINED ON A POROUS SILICA SUPPORT

By

Xiaoran Zhang

A DISSERTATION

Submitted to
Michigan State University
in partial fulfillment of the requirements
for the degree of

Chemistry-Doctor of Philosophy

2017

ABSTRACT

DESIGN AND ASSESSMENT OF FLOW-THROUGH CATALYTIC SYSTEM USING PALLADIUM NANOPARTICLE CATALYST CONFINED ON A POROUS SILICA SUPPORT

By

Xiaoran Zhang

Catalysis has the potential to play a significant role in the converting biomass feedstock to commodity chemicals and fuels. There are a few requirements for the catalysts to fulfill during the biorefinery process: optimal reactivity and high selectivity under relatively mild reaction conditions. These properties can be optimized through the choice of catalyst and the morphology of the catalyst support, immobilization chemistry, solvent system for the reaction, and reaction conditions. The purpose of this work is to create and demonstrate a flow-through catalytic reaction system that enhances the target heterogeneous reaction under mild reaction conditions, and to assess the performance of catalyst reactivity and selectivity.

To design the flow-through catalytic system, we created a silica-polymer composite inverse opal structure with relatively low defect density to be used as a catalyst support. The construction of the inverse opal structures involved the self-assembly of a template with colloidal polystyrene nanospheres, deposition of the poly(ethylene glycol)-silica sol gel composite precursors in the interstitial spaces between the colloidal spheres, and removal of the template nanospheres by dissolution. The addition of PEG into the silica sol gel modifies the morphology of inverse opal structures to reduce defect density. The resulting inverse opals were characterized by scanning electron microscopy (SEM). By optimizing the composition and molecular weight of polymer, the composite inverse opal

structure was improved to reduce the number of defects compared to a silica sol gel inverse opal.

The inverse opal structure was replaced by a porous glass frit because of the improved structural integrity of the latter as well as its reduced resistance to flow when used in a flow-through catalytic format. Using Glucose Oxidase (GOx) as a catalyst, a porous glass frit was shown to be a practical, functional catalyst support that compared favorably to the inverse opal support. We chose porous glass frits as catalyst supports for further studies with flow-through catalytic reactions.

Using a porous glass frit support, the catalytic performance of palladium nanoparticles was evaluated in a flow-through reaction format. The reactivity and selectivity of the catalyst was assessed by heterogeneous hydrogenation of p-coumaric acid and cinnamaldehyde under mild conditions and in different solvents. A microelectric actuator control system was used to maintain H2(g) level in the reaction stream. The results of this work demonstrate high efficiency and the requisite selectivity for the reactions used. This work represents an initial step in the development of a catalysis system for biomass conversion and biorefinery processing.

ACKNOWLEDGEMENTS

I would like to acknowledge a few people who gave me a lot of help while I have pursued my graduate career. First and foremost, I would like to express the deepest appreciation to my graduate research advisor, Dr. Gary J. Blanchard, for his support, encouragement and optimism. Without his guidance and persistent help this dissertation would not have been possible. I would like to thank my committee members, Dr. Thomas Hamann, Dr. Kevin Walker, Dr. Dana Spence and Dr. Merlin Bruening, for all of their assistance along the way.

My fellow Blanchard group members have been an essential part of my graduate research and life. We have had numerous enlightening discussions on research and have been a great help to each other. I would like to thank the following former and current Blanchard research group for their advice and support: Dr. Douglas Gornowich, Dr. Christine Hay, Dr. Iwan Setiawan, Dr. Chen Qiu, Dr. Stephen Baumler, Dr. Krystyna Kijewska, Fredy Pratama, Hannah Mize, Ke Ma, Barrack Stubbs and Briana Capistran.

In addition, I would like to express my gratitude to the facility staff who help me with the instrumentation for my research. Dr Dan Jones and Dr Tony Schilmiller of the MSU Mass Spectrometry facility trained me for use of chromatography and mass spectrometry instruments. Dr. Kathryn Severin helped me with various analytical instruments in the Analytical/Physical labs in the Chemistry building. Dr. Xudong Fan, Carol Flegler and Abigail Vanderberg at the Michigan State University Center for Advanced Microscopy helped me with electron microscopy characterization.

Last but not least, I would like to thank all of my friends that encouraged me and supported me throughout my life journey in graduate school and the happy time together. I would especially like to thank my parents, Guocai Zhang and Ying Gao, and my husband, Dr. Xiaoming Liu, for their endless love, encouragement and everything they did for me.

TABLE OF CONTENTS

LIST OF TABLES

LIST OF FIGURES

LIST OF SCHEMES

CHAPTER 1: Introduction and background

1.1 Biorefinery

Global energy consumption remains heavily dependent on fossil fuels such as petroleum, coal and natural gas. Due to the finite extent of the world crude oil reserve, increasing cost of extraction, environmental concerns, unsustainable growth and uneven product distribution, there is great interest in identifying alternative energy sources. Immediate benefits to the use of alternative energy sources include a reduced dependence on fossil fuels, mitigation of climate change and the utilization of renewable resources.[1] Biomass, the only carbon-rich resources on earth other than fossil fuels, is abundant, low cost and is a potential alternative energy source for carbon-based fuels and raw materials for manufacturing.[2] The paradigm shift from fossil fuels to biomass resources will be important to the global environment and sustainable economy through the utilization of renewable resources and the creation of new opportunities for the chemical industry and related industries.[3] The key to the realization of this goal lies in the creation of bio-refineries, facilities or networks of facilities that converts biomass to biofuels and other value-added materials.[4] The notion of a bio-refinery is analogous to a petroleum refinery, where the catalytic conversion of raw materials to high-value products is central to industrial development and operation as well as consumer use. There are fundamental chemical differences between crude oil and biomass that preclude the direct application of current refinery technology to bioprocessing. For example, hydrocarbons obtained from crude oil are nonpolar, volatile, thermally robust, and unfunctionalized. In contrast, biofeedstocks are typically polar, nonvolatile, and are susceptible to degradation on exposure to acid- and/or heat.[5] Oxygen content is biggest difference between biorenewable feedstock materials and crude oil.[6] Typical biofeedstocks contain from 10% to 44% oxygen. In order to convert biomass into useful biofuels and other compounds, there is an urgent need to develop technologies for industrial and marketable products that convert biomass to reduced hydrocarbons under mild conditions and at the scale required. The replacement of petroleum processing with biofeedstock processing will require technological breakthroughs that will depend on, among other things, the creation of catalytic reaction sequences that are capable of performing sequential reduction reactions.

The majority of products formed from biomass, such as sugars, organic acids, polyols and other partially oxidized organic species, are characterized by the presence of multiple oxyden-containing functionalities. The conversion of such products to produce hydrocarbons via selective deoxygenation, without C-C bond cleavage and in some instances condensation, will require the development of efficient multistep reactions that will require catalysts and design formats that are not currently available.[6]

Catalytic routes and catalysts for bio-refinery operation need to be developed to optimize turnover rate and extent of completion under mild reaction conditions. Because of the low volatility and thermal stability of biomass materials, heterogeneous catalysts will be required that operate on solution phase (dissolved) feedstock, limiting the temperatures and pressures accessible. Consistent with the principles of green chemistry, the catalysts to be used for bio-refinery applications should be implemented in a manner that allows facile separation and product recovery under mild conditions.[7]

The current goals for renewable bio-refineries are improving the heterogeneous catalysts used and optimizing catalytic systems to fulfill the two key requirements of high selectivity and quantitative reactivity to transform biomass derivatives into hydrocarbons.

Fortunately, only a few elementary transformations are required to make a bio-refinery functional. These are deoxygenation/oxidation, hydrogenation/dehydration, hydrogenolysis, carbonylation/decarbonylation, and condensation. This research project will mainly focus on the hydrogenation and deoxygenation reactions of prototypical organic species that can be used as models for biomass compounds.

1.2 Catalytic cassettes system

The work in this dissertation focuses on the design of a catalytic cassette system capable of converting biomass feedstock into desired products through a series of reactions, where the reactions of interest will ultimately be performed sequentially. The catalysts chosen for this work are either metal nanoparticles or enzymes, and they are immobilized in the porous catalyst support structures. The catalyst-loaded supports can, in principle, be arranged in sequences that allow the sequential performance of elementary reactions relevant to the conversion of biofeedstocks in a single-pass process (Scheme 1). If the catalysts selected are sufficiently selective and are optimized for specific elementary reactions, the supported catalysts will be integrated into a flow-through reactor to transform biomass-derived feedstock to desired products. The ultimate goal is that the modular bio-refinery system can achieve a functional and predetermined cascade of elementary reactions by using the order of reaction-specific cassettes in flow reactors.

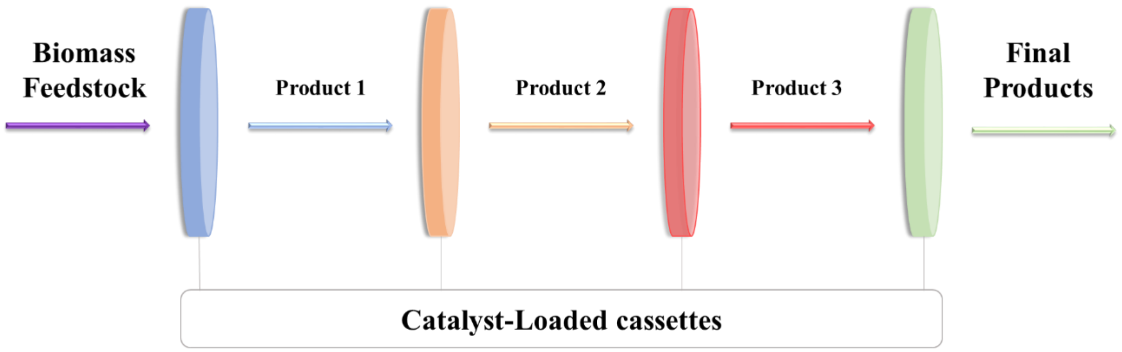

Figure 1.1 Schematic of proposed catalytic cassette system capable of converting biomass feedstock into desired products through a series of sequential reactions. The products from a given reaction are designed to be feedstock for the next cassette.

A key goal of this strategy is to develop catalytic systems that minimize the formation of side products and operate quantitatively, to minimize the need for post-reaction cleanup prior to performing the next reaction. It is clear that these are challenging goals, and the identification of catalysts with high selectivity and optimal reactivity is the necessary first step. This dissertation will discuss the selectivity and reactivity of nanoparticle catalysts in later part of this chapter and their catalytic performance on hydrogenation and deoxygenation catalytic reaction of phenolic compounds in Chapters 4 and 5. The catalyst alone is not the only requirement for success. The catalyst support can also play an important role in the development of a model bio-refinery system. To enhance the reactivity, catalysts were incorporated into porous structures to create flow-through cassettes. Two silica-based porous catalyst support materials, inverse opals and porous glass frits, were studied for the immobilization of catalysts. Comparisons of catalytic performance will be made in Chapter 3.

1.2.1 Inverse opal

The inverse opal structures, also known as three-dimensionally ordered microporous (3DOM) materials, has captured the interest of scientists for many reasons over last decade.[8] These structures offer a high extent of ordering and structural regularity, and significant control over the characteristic pore size and void volume. Inverse opals are formed in several steps; layered assembly of a colloidal crystal template of monodisperse microspheres; filling the void space between microspheres with the matrix material of choice; and removal of microsphere template.[9] Such structures are grown routinely in the Blanchard labs.[10-12] In this work, a low-defect inverse opal structure was modified to function as catalyst support in a flow-through cassette system.[13]

There are several advantages to the inverse opal structure for catalyst support applications. These include a three-dimensional nanoporous structure to achieve usefully high surface area/volume ratio for catalyst loading. For a reactant stream flowing through an inverse opal structure, the characteristic internal dimensions and highly porous structure gives rise to usefully long reactant pathways to increase the probability of reactant-catalyst interactions in the heterogeneous reactor.[9]

Tunable pore size is another advantage of inverse opal structures compared to other catalyst supports, such as zeolites. Zeolites[14-15] are used widely as catalyst supports based on their relatively high surface area and porosity, but these materials are limited in terms of control over the characteristic pore size by the chemical identity of the inorganic matrix, which is not adjustable. With inverse opals, pore size is controlled by the size of the templating spheres used in constructing the structure. The diameter of the templated voids is related to the number of interactions a reactant is expected to experience with (surface-bound) catalyst. If the diameter of the inverse opal void is less than the diffusion length of the reactant, there will be multiple reactant-catalyst collisions during the reactant's residence time in the void volume. Because of the probability of a catalytic event occurring is proportional to the number of reactant-catalyst interactions, the smaller the void volume, the higher probability of a catalytic event occurring.

Inverse opals can be constructed using a wide variety of materials, including metals such as Au,[16] Ni,[17] Pt,[10, 16] Pd,[18] Co,[18] Cu[19] and oxides such as silica,[20] titania,[21] zirconia[22] and alumina,[23] or conductive oxides such as ITO[24] and FTO.[25] The ability to form inverse opal structures using either conductive or dielectric materials provides versatility in their range of application, including electrochemical and bio-catalytic reactions. In addition, inverse opal structures are capable surface functionalization to render their surfaces useful for the immobilization of nanoparticle catalysts or enzymes.

1.2.2 Porous glass frits

Silica-based porous materials have been utilized as heterogeneous catalyst supports by loading with nanoparticles and enzymes.[26] Porous oxide supports offer the potential for enhanced catalytic activity because their characteristically small internal dimensions create moderately high surface area combined with porosity sufficient for flow-through reaction applications. Porous oxides are classified into three categories based on pore size. These are micro- (less than 2 nm diameter), meso- (2 nm to 50 nm diameter) and macro-porous (greater than 50 nm diameter) materials.[27] Porous glass frit is the leaching product of phase-separated alkali borosilicate glass,[28] and it can be readily incorporated into flow-through catalytic cassette systems.

Commercially available fine pore size (0.9 μm to 8 μm diameter) meets the requirement of controlled pore size at an adequate level of precision. As mentioned above, smaller pore sizes increase the substrate-catalyst interaction and probability of a catalytic reaction event. The pore diameter also limits the achievable flow rate and if too small, flow rate can become a limiting factor. Commercial porous glass frit achieves a balance between pore size and permeability. In contrast to inverse opal structures, porous glass frit exhibits highly favorable thermal, mechanical and chemical stability on exposure to mineral acids and organic solvents. Porous glass frits are physically robust and mechanically much more stable than inverse opal structures when utilized in flow-through cassettes. Porous glass frits are also easy to process using standard techniques to regenerate surface silanol functionality.[29] Porous glass frits can be surface-modified to accommodate the binding of nanoparticles and enzymes.[29-30] For catalytic reactions, post-reaction cleanup and catalyst reusability are primary concerns in heterogeneous catalysis and porous glass frits are amenable to such processing.

1.3 Metal nanoparticles catalyst

Metal nanoparticles have been used as heterogeneous catalysts for a long time because of their characteristically high surface area-to-volume ratios compared to the same bulk metal. For metal atoms organized in a close-packed configuration, for a 2 nm diameter nanoparticle, *ca*. 60% of all metal atoms are on the surface, while for a 1 μm diameter particle, fewer than 0.1% of the metal atoms occupy surface sites.[31] Nanoparticles thus exhibit a higher degree of atom economy than larger structural formats, and such considerations are important for rare elements.[32-34] It has been found that for heterogeneous catalytic reactions, the reaction efficiency is sensitive to the nanoscale morphology of the catalyst nanoparticle because the coordination of reactants to the surface-active site(s) depends on the ability to form chemical bonds or coordinate with surface metal atoms.[35,36] Therefore, careful control of nanoparticle size and shape is essential and we have investigated this matter to a limited extent. In some instances, stabilizing agents can be used to control nanoparticle growth and nucleation process thermodynamically.[37-38]

There is a significant body of work focused on heterogeneous catalysis using precious metal nanoparticles, with emphasis being placed on nanoparticle stability, selectivity and activity when bound to various supports.[39] Pd nanoparticles exhibit favorable heterogeneous catalytic activity for the selective hydrogenation of C=C bonds, the Heck reaction, Suzuki-Miyaura coupling reactions and hydrodeoxygenation reactions.[40-42] These capabilities make Pd especially useful for biomass catalysis.[43]

1.3.1 Fabrications and Characterization

Wet chemical nanoparticle preparations are performed as the chemical reduction of metal salts, decomposition of metastable organometallic compounds, with various stabilizers, such as ligands, polymers, or surfactants present to control nanoparticle size and morphology.[33] Lin has prepared uniform colloidal Pd nanoparticles (NPs) in the size range of 2.5 nm to 3 nm by thermal decomposition with biotin as the stabilizing agent.[44] In that work, as-synthesized Pd NPs were immobilized in a microfluidic reactor with the carboxylic acid functionality of the passivating biotin binding to the decorated reactor wall surface. The catalytic activity of biotinylated Pd NPs was evaluated using the hydrogenation of 6-bromo-1-hexene at room temperature and one atmosphere of hydrogen pressure. First-run conversion of 85% with 100% selectivity was achieved.[44]

Polymers are widely used in the fabrication of size- and shape- controlled metal nanoparticles. For example, Hirai *et al*. reported Pd NPs were fabricated by reducing $PdCl_2$ with poly(N-vinyl-2-pyrrolidone) (PVP).[45] PVP is used commonly as steric stabilizer or capping agent to prevent aggregation because it is a water soluble linear polymer that contains hydrophilic functionality.[46] The catalytic reactivity of the resulting Pd NPs was evaluated by hydrogenation of 1,3-cyclooctadiene at atmospheric pressure. With increasing polymer molecular weight the thickness of PVP layer absorbed on the Pd NPs increased and the initial hydrogenation rate decreased because the polymer film limits the diffusion of 1,3-cyclooctadiene to the reactive surface of nanoparticle.[45]

To minimize the use of toxic chemicals, green synthesis of nanomaterials can be performed using plant extract(s) as reducing agent and stabilizing agents. Such compounds include polyphenols, polysaccharides and others that contain hydroxyl functionality. The shape, size and stability of nanoparticles is controlled through the pH, temperature, reaction time and concentrations of plant extract and metal salts used.[47] Mahmoud *et al*. reported the green synthesis of Pd NPs (2.5 nm - 14 nm size range) using *Hippophae rhamnoides Linn* leaf extract as the reducing and stabilizing agent. The heterogeneous catalytic activity of the resulting Pd NPs was evaluated using the Suzuki–Miyaura coupling reaction in water.[40] Coupling reactions of different aryl halides with phenylboronic acid gave high yields (85%-97%) in the presence of as-synthesized Pd NPs at 100 °C in alkaline medium.

Particle size is the most basic and one of the most important pieces of information available for metal nanoparticles. Transmission electron microscopy (TEM) can provide an accurate assessment of particle size and shape as well as crystal lattice existence and orientation.[48] Particle size distribution information is also available from TEM data and energy dispersive X-ray spectroscopy (EDS) can be used to confirm the elemental composition of metal nanoparticles. Dynamic Light Scattering (DLS) can, in certain cases, also be used for particle size and size distribution determination. For multicomponent mixed metal NPs, the ratio of metals present can be determined by inductively coupled plasma atomic emission spectroscopy (ICP-AES). With this technique, the metal NPs are dissolved in strong acid, such as *aqua regia*. To information on the crystalline properties of metal NPs, X-ray diffraction (XRD) can be used to determine crystal structures using the Scherrer Equation.[49] For functionalized nanoparticles, Fourier Transform Infrared (FT-IR) spectroscopy can be used to probe surface adsorption of ligands and functional groups on metal nanoparticles.[50] In addition, quantitative determination of the amount of organic coating and its thermal stability can be performed using Thermogravimetric analysis (TGA).[51] There are a number of different techniques available that can be used to acquire information on metal nanoparticles that are synthesized in the course of this work.

1.3.2 Supports for metal nanoparticles

As mentioned above, the supports for nanoparticle catalyst can also affect catalytic activity and selectivity. There is a significant body of literature extant on Pd NPs on oxide supports, including silica[52] and alumina.[53] Silica-based supports are used more widely than alumina and they exist in various forms, ranging from silica sol-gels to MCM-41 and zeolites.[54]

The classic methods used to synthesize nanoparticles in porous oxides is the wetting of the solid support with a solution containing the metal salt precursor, which is reduced *in situ*. This technique is referred to as wetness impregnation and simultaneous precipitation of the metal and the support.[55-56] This method tends to yield a distribution of nanoparticle sizes and shapes. Several simple and reliable methods of nanoparticle synthesis and immobilization on supports will be discussed as examples in Chapter 4.

The functionalization of oxide support surfaces can prevent metal nanoparticles from leaching and can improve the activity and reusability of the catalyst-support system. Mandal *et al*. reported Pd NPs bound to Na-Y zeolites modified with 3-aminopropyltrimethoxysilane (APTMS).[57] Catalyst on amine-functionalized zeolites has demonstrated high activity and reusability as heterogeneous catalysts for hydrogenation and Heck reactions. As noted previously, Lin used biotinylated-Pd NPs immobilized in a microfluidic reactor with biotin linked to the surface functionalized with (3-aminopropyl) trimethoxysilane (APTMS).[44]

Polymers have also been used for anchoring nanoparticles to supports in various ways, such as polymer brushes and grafts, monoliths and porous polymers, natural polymers (*e.g.* polyphenols, polysaccharides) and conjugated polymers.[56] Polymer chains are, in many instances, flexible and contain functional groups that can immobilize nanoparticles through a variety of chemical interactions. For example, the Ballauff group reported Pd NPs immobilized on spherical polyelectrolyte brushes (SPB). The SPB has a solid poly(styrene) core with a dense layer of polyelectrolytes formed by long chains of poly(2-methylpropenoyloxyethyl) trimethylammonium chloride (PMPTAC) grafted onto the core. $PdCl_4^{2-}$ ions initially bind to the positively charged polymer chains, and the metal ion is subsequently reduced and dispersed within in the polymer brush region.[58-59]

The use of ionic liquids for catalysis has drawn much attention over the past decade.[60-62] Their characteristics, such as low vapor pressure, favorable solubility and acidity/coordination properties, suggest a range of applications in developing green catalytic technology.[63] Huang *et al*. conducted a study of the immobilization of Pd NP catalyst onto molecular sieves using the ionic liquid 1,1,3,3-tetramethylguanidinium lactate

(TMGL) in order to perform a solvent-free hydrogenation reaction.[64] The catalyst was evaluated through the solvent-free hydrogenation of alkenes and demonstrated 100% conversion of cyclohexene without significant loss of activity after another four runs.

The development of supported catalyst systems is well underway, and the contribution of this dissertation to the effort lies in the demonstration of metal nanoparticle catalysts and enzyme catalysts bound to porous silica support structures. The evaluation of two types of silica support, inverse opals (Chapter 2) and porous glass frits (Chapters 4 and 5), points the way to further work with the ultimate goal of creating a flow-through, multi-step bio-refinery that can function under conditions consistent with green chemistry.

REFERENCES

REFERENCES

1. Armaroli, N.; Balzani, V., The future of energy supply: Challenges and opportunities. *Angew Chem Int Edit* **2007,** *46* (1-2), 52-66.

2. Stocker, M., Biofuels and Biomass-To-Liquid Fuels in the Biorefinery: Catalytic Conversion of Lignocellulosic Biomass using Porous Materials. *Angew Chem Int Edit* **2008,** *47* (48), 9200-9211.

3. Ragauskas, A. J.; Williams, C. K.; Davison, B. H.; Britovsek, G.; Cairney, J.; Eckert, C. A.; Frederick, W. J.; Hallett, J. P.; Leak, D. J.; Liotta, C. L.; Mielenz, J. R.; Murphy, R.; Templer, R.; Tschaplinski, T., The path forward for biofuels and biomaterials. *Science* **2006,** *311* (5760), 484-489.

4. Cherubini, F., The biorefinery concept: Using biomass instead of oil for producing energy and chemicals. *Energy Conversion and Management* **2010,** *51* (7), 1412-1421.

5. Irfan, M.; Glasnov, T. N.; Kappe, C. O., Heterogeneous Catalytic Hydrogenation Reactions in Continuous-Flow Reactors. *Chemsuschem* **2011,** *4* (3), 300-316.

6. Vlachos, D. G.; Chen, J. G.; Gorte, R. J.; Huber, G. W.; Tsapatsis, M., Catalysis Center for Energy Innovation for Biomass Processing: Research Strategies and Goals. *Catalysis Letters* **2010,** *140* (3), 77-84.

7. Garkhedkar, A. M.; Shingote, S. K.; Rane, V. H.; Kelkar, A. A.; Ranade, V. V., Intensifying Hydrogenation of Cinnamaldehyde to Cinnamyl Alcohol: Catalyst, Solvent and Operating Conditions. *Indian Chemical Engineer* **2015,** *57* (3-4), 219-239.

8. Stein, A.; Li, F.; Denny, N. R., Morphological Control in Colloidal Crystal Templating of Inverse Opals, Hierarchical Structures, and Shaped Particles. *Chemistry of Materials* **2008,** *20* (3), 649-666.

9. Stein, A., Sphere templating methods for periodic porous solids. *Microporous and Mesoporous Materials* **2001,** *44*, 227-239.

10. Dimos, M. M.; Blanchard, G. J., Evaluating the Role of Pt and Pd Catalyst Morphology on Electrocatalytic Methanol and Ethanol Oxidation. *The Journal of Physical Chemistry C* **2010,** *114* (13), 6019-6026.

11. Dimos, M. M.; Blanchard, G. J., Examining the Electrocatalytic Oxidation of Selected Diols at Nanoporous and Planar Pt Electrodes. *The Journal of Physical Chemistry C* **2011,** *115* (22), 11247-11256.

12. Dimos, M. M.; Blanchard, G. J., Electro-catalytic oxidation of 1,2-propanediol at nanoporous and planar solid Pt electrodes. *Journal of Electroanalytical Chemistry* **2011,** *654* (1), 13-19.

13. Zhang, X.; Blanchard, G. J., Polymer Sol–Gel Composite Inverse Opal Structures. *ACS Applied Materials & Interfaces* **2015,** *7* (11), 6054-6061.

14. Tao, Y. S.; Kanoh, H.; Abrams, L.; Kaneko, K., Mesopore-modified zeolites: Preparation, characterization, and applications. *Chem Rev* **2006,** *106* (3), 896-910.

15. Corma, A., From microporous to mesoporous molecular sieve materials and their use in catalysis. *Chem Rev* **1997,** *97* (6), 2373-2419.

16. Bartlett, P. N.; Baumberg, J. J.; Birkin, P. R.; Ghanem, M. A.; Netti, M. C., Highly Ordered Macroporous Gold and Platinum Films Formed by Electrochemical Deposition through Templates Assembled from Submicron Diameter Monodisperse Polystyrene Spheres. *Chemistry of Materials* **2002,** *14* (5), 2199-2208.

17. Yan, H.; Blanford, C. F.; Holland, B. T.; Parent, M.; Smyrl, W. H.; Stein, A., A Chemical Synthesis of Periodic Macroporous NiO and Metallic Ni. *Advanced Materials* **1999,** *11* (12), 1003-1006.

18. Bartlett, P. N.; Birkin, P. R.; Ghanem, M. A., Electrochemical deposition of macroporous platinum, palladium and cobalt films using polystyrene latex sphere templates. *Chemical Communications* **2000,** (17), 1671-1672.

19. Jiang, P.; Cizeron, J.; Bertone, J. F.; Colvin, V. L., Preparation of Macroporous Metal Films from Colloidal Crystals. *Journal of the American Chemical Society* **1999,** *121* (34), 7957-7958.

20. Johnson, S. A.; Ollivier, P. J.; Mallouk, T. E., Ordered Mesoporous Polymers of Tunable Pore Size from Colloidal Silica Templates. *Science* **1999,** *283* (5404), 963-965.

21. Wijnhoven, J. E. G. J.; Vos, W. L., Preparation of Photonic Crystals Made of Air Spheres in Titania. *Science* **1998,** *281* (5378), 802-804.

22. Holland, B. T.; Blanford, C. F.; Stein, A., Synthesis of Macroporous Minerals with Highly Ordered Three-Dimensional Arrays of Spheroidal Voids. *Science* **1998,** *281* (5376), 538-540.

23. Holland, B. T.; Blanford, C. F.; Do, T.; Stein, A., Synthesis of Highly Ordered, Three-Dimensional, Macroporous Structures of Amorphous or Crystalline Inorganic Oxides, Phosphates, and Hybrid Composites. *Chemistry of Materials* **1999,** *11* (3), 795-805.

24. Juárez, B. H.; López, C.; Alonso, C., Formation of Zinc Inverted Opals on Indium Tin Oxide and Silicon Substrates by Electrochemical Deposition. *The Journal of Physical Chemistry B* **2004,** *108* (43), 16708-16712.

25. Yang, Z.; Gao, S.; Li, W.; Vlasko-Vlasov, V.; Welp, U.; Kwok, W.-K.; Xu, T., Three-Dimensional Photonic Crystal Fluorinated Tin Oxide (FTO) Electrodes: Synthesis and Optical and Electrical Properties. *ACS Applied Materials & Interfaces* **2011,** *3* (4), 1101-1108.

26. Wan, Y.; Zhao, On the Controllable Soft-Templating Approach to Mesoporous Silicates. *Chemical Reviews* **2007,** *107* (7), 2821-2860.

27. An, K.; Somorjai, G. A., Nanocatalysis I: Synthesis of Metal and Bimetallic Nanoparticles and Porous Oxides and Their Catalytic Reaction Studies. *Catalysis Letters* **2015,** *145* (1), 233-248.

28. Inayat, A.; Reinhardt, B.; Uhlig, H.; Einicke, W.-D.; Enke, D., Silica monoliths with hierarchical porosity obtained from porous glasses. *Chemical Society Reviews* **2013,** *42* (9), 3753-3764.

29. Hartmann, M.; Kostrov, X., Immobilization of enzymes on porous silicas - benefits and challenges. *Chemical Society Reviews* **2013,** *42* (15), 6277-6289.

30. Parlett, C. M. A.; Bruce, D. W.; Hondow, N. S.; Lee, A. F.; Wilson, K., Support-Enhanced Selective Aerobic Alcohol Oxidation over Pd/Mesoporous Silicas. *ACS Catalysis* **2011,** *1* (6), 636-640.

31. Bernstein, E. R., *Atomic and molecular clusters*. Elsevier: New York;Amsterdam, Netherlands;, 1990; Vol. 68.

32. Thomas, J. M.; Johnson, B. F. G.; Raja, R.; Sankar, G.; Midgley, P. A., High-Performance Nanocatalysts for Single-Step Hydrogenations. *Accounts of Chemical Research* **2003,** *36* (1), 20-30.

33. Bönnemann, H.; Richards, Ryan M., Nanoscopic Metal Particles − Synthetic Methods and Potential Applications. *European Journal of Inorganic Chemistry* **2001,** *2001* (10), 2455-2480.

34. Lin, R., *Rational design of colloidal noble metallic nanocatalysts and development of a microfluidic platform for fundamental assessment of catalytic activity*. 2013.

35. Nishimura, S.; Ebitani, K., Recent Advances in Heterogeneous Catalysis with Controlled Nanostructured Precious Monometals. *ChemCatChem* **2016,** *8* (14), 2303-2316.

36. Liu, P.; Qin, R.; Fu, G.; Zheng, N., Surface Coordination Chemistry of Metal Nanomaterials. *Journal of the American Chemical Society* **2017,** *139* (6), 2122-2131.

37. Jana, N. R.; Chen, Y.; Peng, X., Size- and Shape-Controlled Magnetic (Cr, Mn, Fe, Co, Ni) Oxide Nanocrystals via a Simple and General Approach. *Chemistry of Materials* **2004,** *16* (20), 3931-3935.

38. Burda, C.; Chen, X. B.; Narayanan, R.; El-Sayed, M. A., Chemistry and properties of nanocrystals of different shapes. *Chemical Reviews* **2005,** *105* (4), 1025-1102.

39. Aresta, M.; Dibenedetto, A.; Dumeignil, F., *Biorefinery: From Biomass to Chemicals and Fuels*. 1. Aufl. ed.; Walter de Gruyter GmbH Co.KG: Berlin/Boston, 2012.

40. Nasrollahzadeh, M.; Sajadi, S. M.; Maham, M., Green synthesis of palladium nanoparticles using Hippophae rhamnoides Linn leaf extract and their catalytic activity for the Suzuki–Miyaura coupling in water. *Journal of Molecular Catalysis A: Chemical* **2015,** *396*, 297-303.

41. Zhao, C.; Kou, Y.; Lemonidou, A. A.; Li, X.; Lercher, J. A., Highly Selective Catalytic Conversion of Phenolic Bio-Oil to Alkanes. *Angewandte Chemie International Edition* **2009,** *48* (22), 3987-3990.

42. de Souza, P. M.; Rabelo-Neto, R. C.; Borges, L. E. P.; Jacobs, G.; Davis, B. H.; Resasco, D. E.; Noronha, F. B., Hydrodeoxygenation of Phenol over Pd Catalysts. Effect of Support on Reaction Mechanism and Catalyst Deactivation. *ACS Catalysis* **2017,** *7* (3), 2058-2073.

43. Yan, N.; Xiao, C.; Kou, Y., Transition metal nanoparticle catalysis in green solvents. *Coordination Chemistry Reviews* **2010,** *254* (9), 1179-1218.

44. Lin, R.; Freemantle, R. G.; Kelly, N. M.; Fielitz, T. R.; Obare, S. O.; Ofoli, R. Y., In situ immobilization of palladium nanoparticles in microfluidic reactors and assessment of their catalytic activity. *Nanotechnology* **2010,** *21* (32).

45. Hirai, H.; Yakura, N.; Seta, Y.; Hodoshima, S., Characterization of palladium nanoparticles protected with polymer as hydrogenation catalyst. *Reactive and Functional Polymers* **1998,** *37* (1), 121-131.

46. Xiong, Y.; Washio, I.; Chen, J.; Cai, H.; Li, Z.-Y.; Xia, Y., Poly(vinyl pyrrolidone): A Dual Functional Reductant and Stabilizer for the Facile Synthesis of Noble Metal Nanoplates in Aqueous Solutions. *Langmuir* **2006,** *22* (20), 8563-8570.

47. Siddiqi, K. S.; Husen, A., Green Synthesis, Characterization and Uses of Palladium/Platinum Nanoparticles. *Nanoscale Research Letters* **2016,** *11* (1), 482.

48. Cho, E. J.; Holback, H.; Liu, K. C.; Abouelmagd, S. A.; Park, J.; Yeo, Y., Nanoparticle Characterization: State of the Art, Challenges, and Emerging Technologies. *Molecular Pharmaceutics* **2013,** *10* (6), 2093-2110.

49. Patterson, A. L., The Scherrer Formula for X-Ray Particle Size Determination. *Physical Review* **1939,** *56* (10), 978-982.

50. Mudunkotuwa, I. A.; Minshid, A. A.; Grassian, V. H., ATR-FTIR spectroscopy as a tool to probe surface adsorption on nanoparticles at the liquid-solid interface in environmentally and biologically relevant media. *Analyst* **2014,** *139* (5), 870-881.

51. Mansfield, E.; Tyner, K. M.; Poling, C. M.; Blacklock, J. L., Determination of Nanoparticle Surface Coatings and Nanoparticle Purity Using Microscale Thermogravimetric Analysis. *Analytical Chemistry* **2014,** *86* (3), 1478-1484.

52. Lang, H.; May, R. A.; Iversen, B. L.; Chandler, B. D., Dendrimer-Encapsulated Nanoparticle Precursors to Supported Platinum Catalysts. *Journal of the American Chemical Society* **2003,** *125* (48), 14832-14836.

53. Yashima, M.; Falk, L. K. L.; Palmqvist, A. E. C.; Holmberg, K., Structure and catalytic properties of nanosized alumina supported platinum and palladium particles synthesized by reaction in microemulsion. *Journal of Colloid and Interface Science* **2003,** *268* (2), 348-356.

54. Astruc, D.; Lu, F.; Aranzaes, J. R., Nanoparticles as Recyclable Catalysts: The Frontier between Homogeneous and Heterogeneous Catalysis. *Angewandte Chemie International Edition* **2005,** *44* (48), 7852-7872.

55. Barau, A.; Budarin, V.; Caragheorgheopol, A.; Luque, R.; Macquarrie, D. J.; Prelle, A.; Teodorescu, V. S.; Zaharescu, M., A Simple and Efficient Route to Active and Dispersed Silica Supported Palladium Nanoparticles. *Catalysis Letters* **2008,** *124* (3), 204-214.

56. White, R. J.; Luque, R.; Budarin, V. L.; Clark, J. H.; Macquarrie, D. J., Supported metal nanoparticles on porous materials. Methods and applications. *Chemical Society Reviews* **2009,** *38* (2), 481-494.

57. Mandal, S.; Roy, D.; Chaudhari, R. V.; Sastry, M., Pt and Pd Nanoparticles Immobilized on Amine-Functionalized Zeolite: Excellent Catalysts for Hydrogenation and Heck Reactions. *Chemistry of Materials* **2004,** *16* (19), 3714-3724.

58. Mei, Y.; Lu, Y.; Polzer, F.; Ballauff, M.; Drechsler, M., Catalytic Activity of Palladium Nanoparticles Encapsulated in Spherical Polyelectrolyte Brushes and Core−Shell Microgels. *Chemistry of Materials* **2007,** *19* (5), 1062-1069.

59. Yu, M.; Lu, Y.; Schrinner, M.; Polzer, F.; Ballauff, M., Spherical Polyelectrolyte Brushes as Carriers for Catalytically Active Metal Nanoparticles. *Macromolecular Symposia* **2007,** *254* (1), 42-45.

60. Vekariya, R. L., A review of ionic liquids: Applications towards catalytic organic transformations. *Journal of Molecular Liquids* **2017,** *227*, 44-60.

61. Amarasekara, A. S., Acidic Ionic Liquids. *Chemical Reviews* **2016,** *116* (10), 6133-6183.

62. Ma, K.; Jarosova, R.; Swain, G. M.; Blanchard, G. J., Charge-Induced Long-Range Order in a Room-Temperature Ionic Liquid. *Langmuir* **2016,** *32* (37), 9507-9512.

63. Zhang, Q.; Zhang, S.; Deng, Y., Recent advances in ionic liquid catalysis. *Green Chemistry* **2011,** *13* (10), 2619-2637.

64. Huang, J.; Jiang, T.; Gao, H.; Han, B.; Liu, Z.; Wu, W.; Chang, Y.; Zhao, G., Pd Nanoparticles Immobilized on Molecular Sieves by Ionic Liquids: Heterogeneous

Catalysts for Solvent-Free Hydrogenation. *Angewandte Chemie International Edition* **2004,** *43* (11), 1397-1399.

CHAPTER 2: Polymer-Sol Gel Composite Inverse Opal Structures

2.1 Abstract

We report on the formation of composite inverse opal structures where the matrix used to form the inverse opal contains both silica, formed using sol-gel chemistry, and poly(ethylene glycol), PEG. We find that the morphology of the inverse opal structure depends on both the amount of PEG incorporated into the matrix and its molecular weight. The extent of organization in the inverse opal structure, which is characterized by scanning electron microscopy and optical reflectance data, is mediated by the chemical bonding interactions between the silica and PEG constituents in the hybrid matrix. Both polymer chain terminus Si-O-C bonding and hydrogen bonding between the polymer backbone oxygens and silanol functionalities can contribute, with the polymer mediating the extent to which Si-O-Si bonds can form within the silica regions of the matrix due to hydrogen bonding interactions.

2.2 Introduction

Organic-inorganic hybrid materials have been studied for decades and applied to optical, electronic and mechanical technologies.[1] The goal of creating such hybrid composite materials is to combine the most useful properties of each constituent material to produce materials with superior performance for specific applications.[2] Sol-gel chemistry is useful in the construction of some composite materials because of its low temperature processing and its ability to combine with functionalized organic species, including polymers. The broad range of sol-gel chemistry available allows for the versatile design of hybrid inorganic/organic materials containing metal alkoxides and alkoxysilanes,[3] providing broad control over the properties of the resulting materials.[4] In any such work, the characteristic length scale of the compositional heterogeneity is critically important, as is the chemical nature of the interface between different compositional regions.[5] For this reason, it is necessary to evaluate such systems experimentally, especially when they are used in the formation of intricate structures such as inverse opals.

We are interested in inverse opal, also called three-dimensionally ordered macroporous (3DOM) structures because of their ability to combine several chemical and physical properties that are useful in catalyst support applications. Specifically, inverse opals are moderately high surface area, they can form flow-through structures with controllable void volumes and pore diameters, and the surface reactivity can allow for the chemical attachment of selected catalytic species. In addition, the close-packed ordered porous structure with the pore size of a few nanometers to micrometers endows 3DOM materials with useful optical and photonic crystal properties.[6] This material structure can be utilized in optical information processing and storage devices, sensors, fuel cell electrodes, catalyst supports and bioactive materials.[7-9] The construction of inverse opals is well established, and there is an extensive literature extant on sol gel chemistry.[10,11] When using sol gel chemistry to create inverse opal structures, it is frequently challenging to create macroscopic regions that are free of defects and cracks. Such features limit the utility of the resulting structure because they provide channels that can bypass functionalized regions of the structure. A major reason for the formation of defects in inverse opal structures is that the support on which the inverse opal is formed does not undergo dimensional change as the sol cures and contracts, and the resulting stresses in the inverse opal structure are alleviated by cracking and defect formation. One goal of our work is to create inverse opal structures that can serve as flow-through catalyst supports and that do not exhibit high defect densities and/or cracks.

In an effort to create inverse opal structures on a porous alumina support that are characterized by a lower defect density than those formed using silica sol gel chemistry alone, we have explored the use of poly(ethylene glycol), PEG, as a matrix additive. Our data reveal a reduction in visible defect and crack density with the addition of PEG, and the extent of structural improvement is found to depend on the amount of PEG and its molecular weight. The primary focus of this work is on understanding the dependence of the hybrid matrix composition on the quality of the inverse opal structure formed.

2.3 Experimental Methods

Experimental materials. Styrene (C_8H_8, ≥99%, Sigma-Aldrich), potassium persulfate ($K_2S_2O_8$), sodium *p*-styrene sulfonate ($C_8H_7SO_3Na$), potassium bicarbonate ($KHCO_3$), sodium hydroxide solution (1 wt% NaOH in water), 2,2-azobisisobutyronitrile (AIBN, 98%, Aldrich), tetraethylorthosilicate (TEOS, ≥99%, Aldrich), ethanol (anhydrous), hydrochloric acid (12 M, Columbus Chemical Industries), poly(ethylene glycol) methyl ether (average M_n = 750 g/mol, Aldrich) poly(ethylene glycol) (BioUltra, 2,000 g/mol, Sigma) poly(ethylene glycol) (10,000 g/mol, Fluka), toluene (≥99.5%, Mallinckrodt), and water (Milli Q), were used as received, without further purification. Whatman® Anodisc filter membranes (porous alumina substrate, d=13 mm, pore size 200 nm, unsupported) were used as the inverse opal supports.

Nanoporous silica structure fabrication. Polystyrene colloidal spheres with an average diameter of 290 nm were synthesized by an emulsion polymerization method.[12] Styrene was washed using a 1% sodium hydroxide solution and distilled prior to use to remove the stabilizer. Distilled styrene monomer was added into 100 mL DI water and heated to 72 ºC. Potassium bicarbonate and sodium *p*-styrene sulfonate were dissolved in DI water, preheated to 72 ºC and transferred to the styrene-containing solution. The reaction is initiated by AIBN and refluxed at 72 ºC for 28 h. The resulting solution was evaporated to dryness using a rotary evaporator.

Colloidal crystal templates were made by the evaporation method.[13,14] Porous alumina substrates were placed vertically into 0.25 wt% polystyrene solution. After evaporation at 65 ºC for 10 hours, close-packed colloidal crystal templates were formed on the porous alumina substrates as uniform films that exhibited strong diffraction of light.

The silica-PEG hybrid matrix was prepared using sol-gel chemistry.[15,16] Silica sol-gel solutions were made for deposition with a range of PEG loadings (0 wt%, 10 wt%, 20 wt% and 30 wt%, each with M_n = 2,000 g/mol PEG) and with a range of PEG molecular weights (750 g/mol, 2,000 g/mol and 10,000 g/mol, each at 10 wt%). After the dissolution of PEG in ethanol (7.5 mL), precursor solutions were obtained by mixing TEOS (1.15 mL), Milli Q water (0.9 mL), 12 M HCl (65 μL) and PEG for 1 hour. The polystyrene (PS) nanosphere template on a porous alumina substrate (PAS), PS/PAS for short, was supported on a glass frit and a vacuum is applied (water aspirator).[17] The sol-gel solution is added drop-wise on the PS/PAS structure so that the sol-gel can fill the interstitial spaces within the nanosphere array. The resulting assembly is dried at 50 ºC for 48 hours, then placed in toluene for 24 hours to remove the polystyrene nanospheres.

Transmission Electron Microscopy (TEM): TEM images were obtained using an ultra-high resolution JEOL 2200FS transmission electron microscope located in the Center for Advanced Microscopy at Michigan State University (MSU). Acceleration voltage was 200 kV.

Scanning Electron Microscopy (SEM): Samples were sputter-coated with Os for 20 seconds and SEM images were obtained using an ultra-high resolution JEOL 7500F scanning electron microscope housed in the Center of Advanced Microscopy at Michigan State University. Acceleration voltage was 5 kV for all images.

Attenuated Total Reflectance Infrared Spectroscopy (ATR-IR): ATR-IR spectra were obtained using a Perkin Elmer Spectrum One FT-IR spectrometer over the spectral range of 650 cm^{-1} to 1500 cm^{-1}. Spectral resolution for all measurements was 4 cm^{-1} and each spectrum was the result of 1024 acquisitions.

Ultraviolet-Visible (UV-vis) spectroscopy: UV-visible reflectance spectra were obtained using a Perkin Elmer Lambda 35 UV/Visible spectrometer. Data were acquired from 200 nm to 1000 nm, with a spectral resolution of 1 nm.

Thermogravimetric Analysis (TGA): TGA measurements were performed using a TA Q500 instrument (TA Instruments) in high-resolution mode with a thermal ramp rate of 25 ºC/min between room temperature and 750 ºC, under dry nitrogen. For these measurements, samples were measured before and after thermal curing at 200 °C for two hours.

Dynamic light scattering（DLS）: The size of the polystyrene spheres was measured using Malvern Zetasizer Nano ZS. The spheres were suspended in an aqueous solution for analysis.

2.4 Results and Discussion

We are interested in understanding the effect of adding PEG to a silica sol-gel matrix for the purpose of making high quality inverse opal structures, schematized in Fig. 2.1. The properties of the inverse opal structures as a function of PEG molecular weight and loading in the sol are of primary interest but issues other than the composition of the hybrid matrix can play a role in the quality of the resulting inverse opal structures.

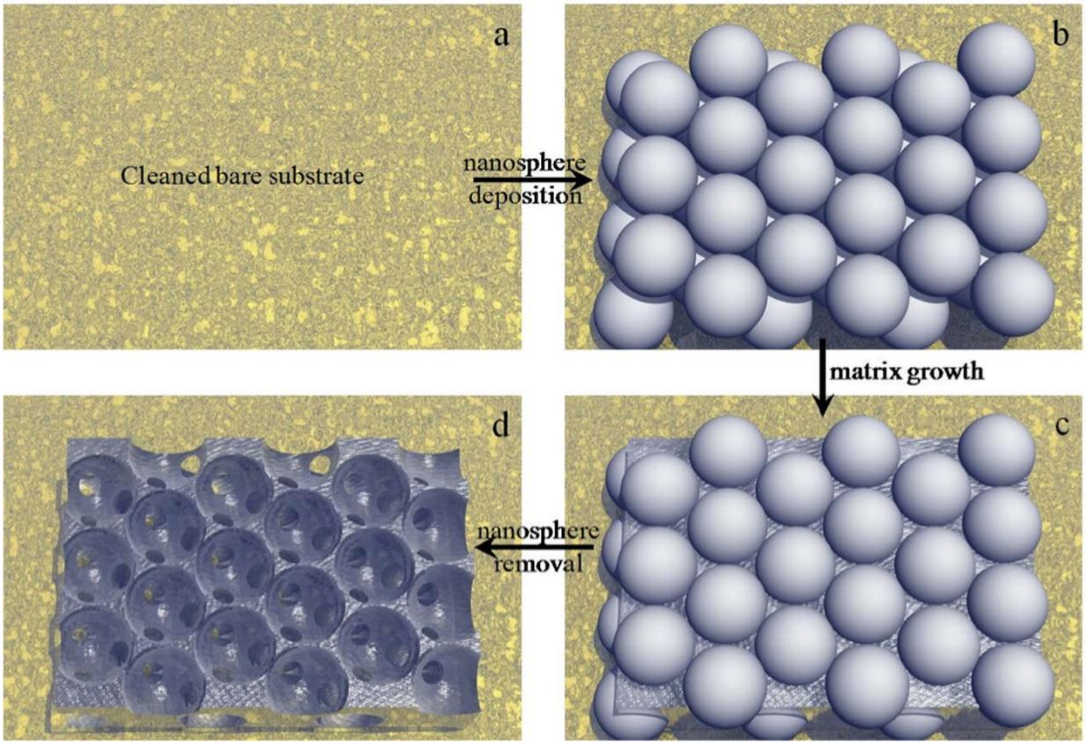

Figure 2.1 Schematic of the construction of an inverse opal structure. In this work, a) The support is a porous alumina membrane. b) The nanospheres are polystyrene and template self-assembles. c) The matrix material is formed using silica sol gel d) The nanosphere template is removed by toluene.

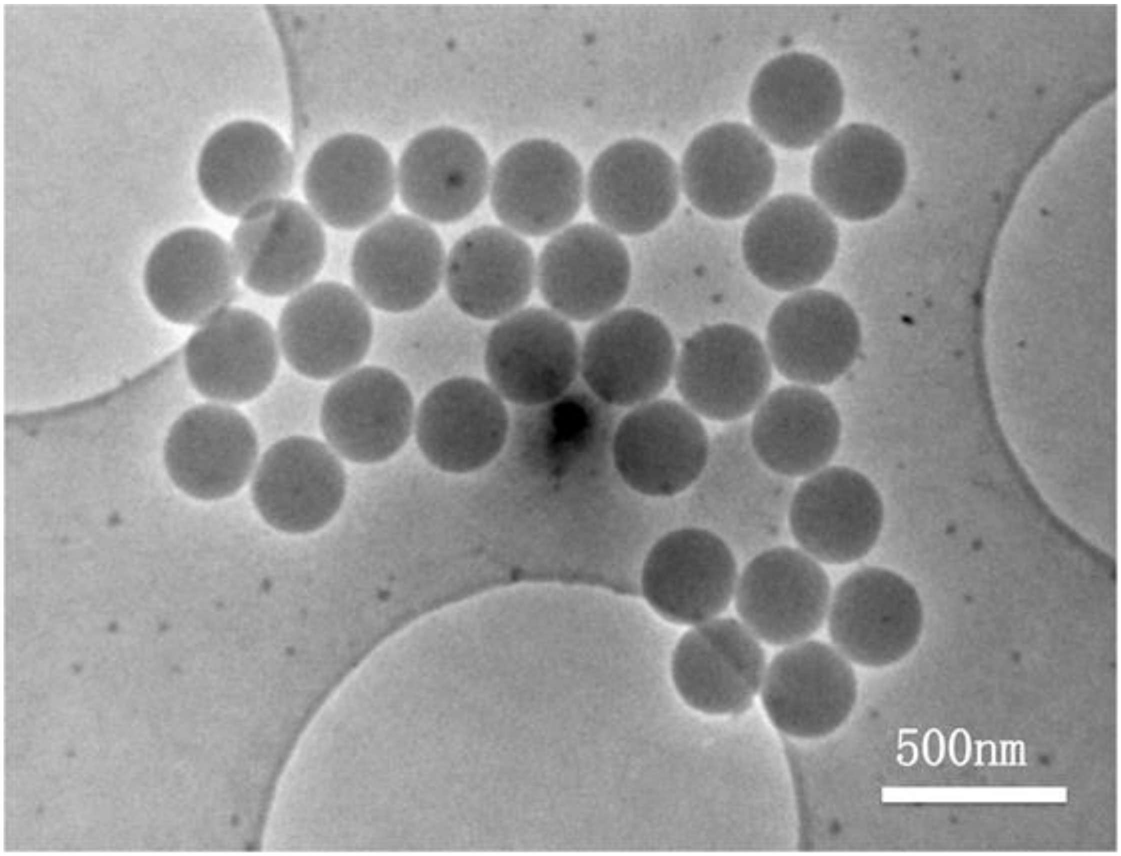

Figure 2.2 TEM image of the polystyrene nanospheres used in this work. The nanospheres appear as dark circles, with the larger light circles being openings in the TEM grid.

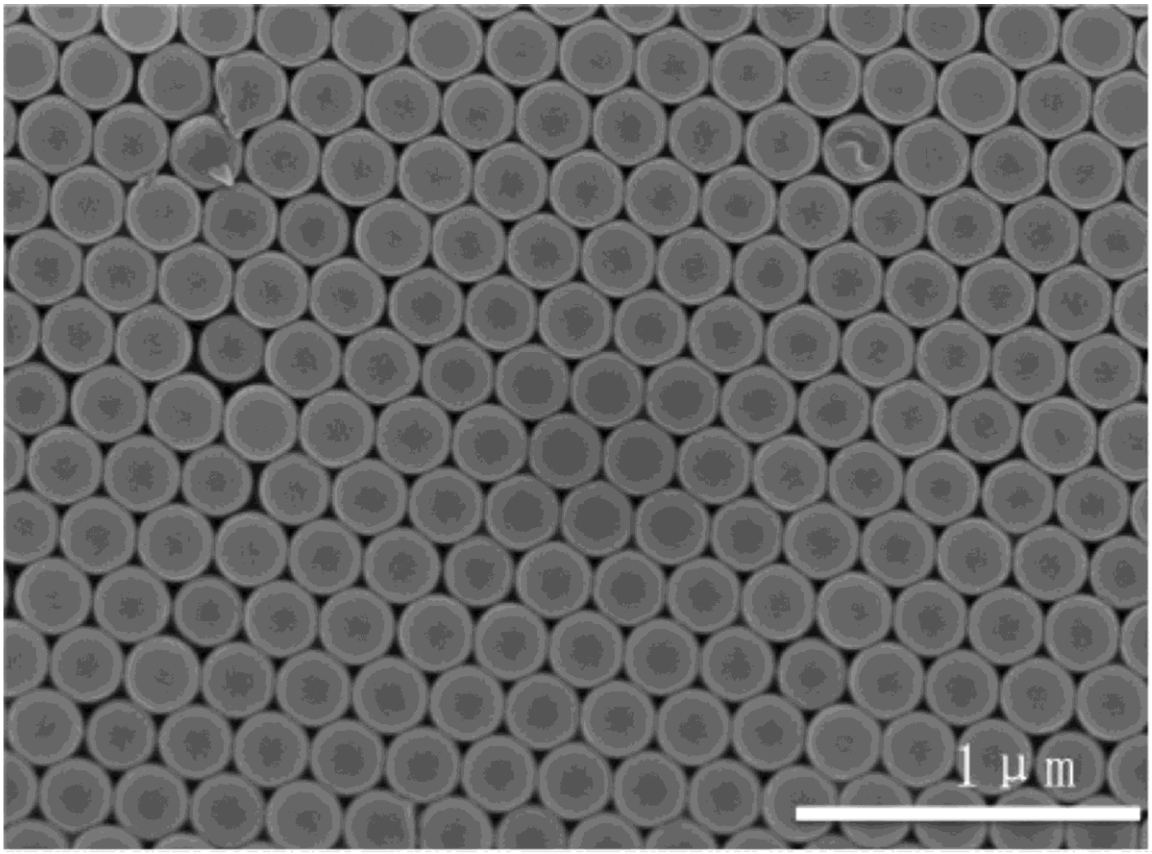

Figure 2.3 SEM image of a colloidal crystal template formed by the polystyrene nanospheres.

A key factor in the growth of high quality inverse opal structures is the monodispersity and surface properties of the polystyrene nanospheres used. Polystyrene colloidal spheres with an average size of 290 ± 30 nm were prepared using emulsifier-free emulsion polymerization (Fig. 2.2).[12] From these nanospheres the template was self-assembled by evaporation (Fig. 2.3).[13] The sol-gel precursor mixture was aspirated into the nanosphere template and the sol-gel reaction was allowed to proceed, resulting in the formation of a silica matrix. Once the matrix was formed, the polystyrene nanospheres were removed by dissolution and a 3D nanoporous inverse opal structure resulted.

2.4.1 Effect of PEG loading on the hybrid matrix.

To investigate the effect of PEG in silica-PEG hybrid materials, the nanoporous matrices have been fabricated using silica precursor only and silica precursor mixed with 10% PEG (M_n = 2,000 g/mol). For the silica-only matrix (Fig. 2.4), significant cracks were formed in the structure and these were associated with matrix curing and consequent contraction. With the addition of PEG, the uniformity of the nanoporous matrix improves significantly, as can be seen in Fig. 2.5. In the SiO_2-PEG composite system, any covalent chemical interaction between the polymer and silica network must be through Si-O-C covalent bonds at the polymer chain termini, and hydrogen bonding may also occur between ether oxygens in the polymer backbone and free silanol groups in the silica matrix.[18] We note that the propensity for the Si-O-C bonds to form will differ for the PEG of M_n = 750 g/mol because it is present as the methyl ether, while the higher molecular weight PEGs exist in the hydroxyl-terminated form. These interactions allow the silica sol-gel to produce a matrix with fewer defects while retaining properties of the polymer,

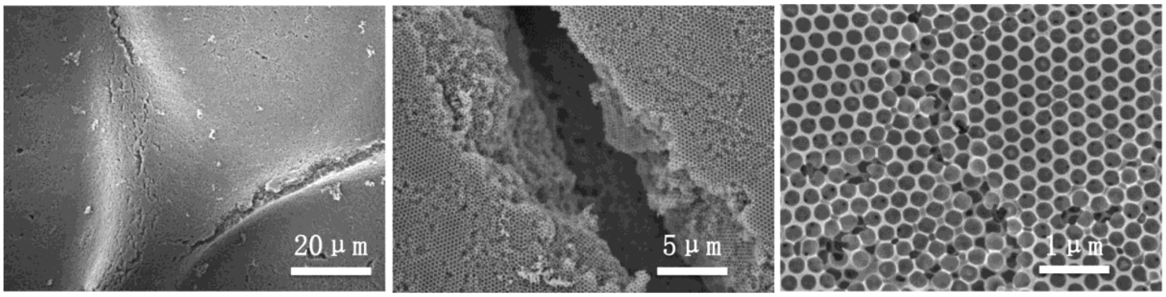

Figure 2.4 SEM images of an inverse opal formed using silica sol gel chemistry with no added PEG. The magnifications are (left to right) 1200, 5000, and 23000, with corresponding scale bars indicating 20 μm, 5 μm, and 1 μm.

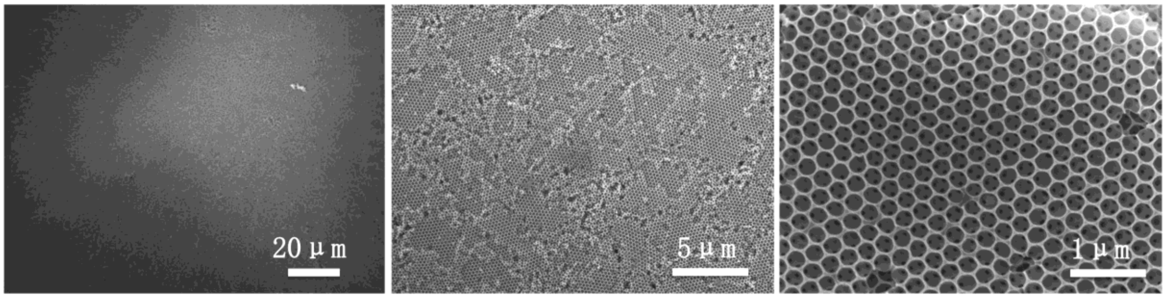

Figure 2.5 SEM images of an inverse opal formed using silica sol gel chemistry with no added PEG. The magnifications are (left to right) 1200, 5000, and 23000, with corresponding scale bars indicating 20 μm, 5 μm, and 1 μm.

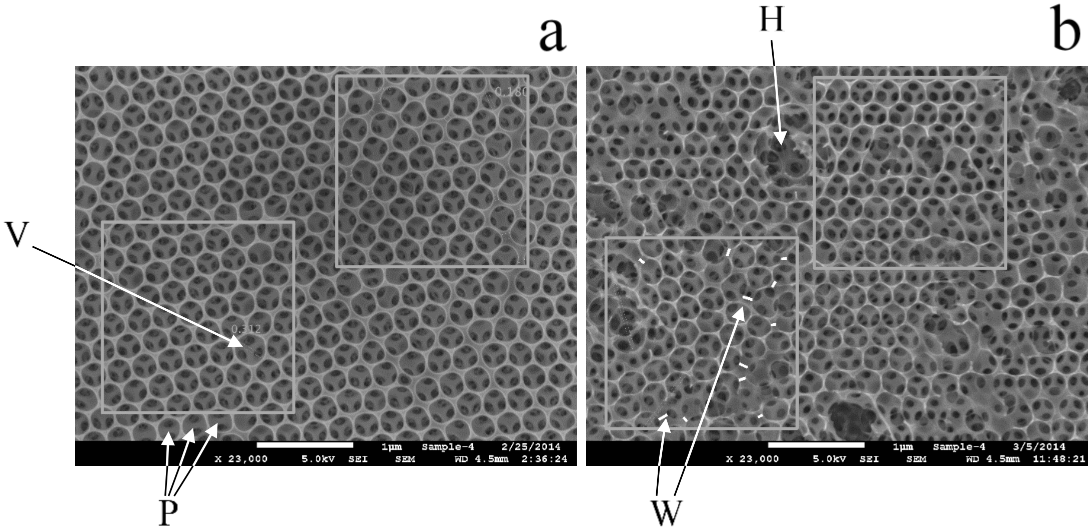

Figure 2.6 Types of defects characterized for inverse opal structures. (a) an inverse opal structure characterized primarily by type V and P defects. (b) an inverse opal structure that contains type H and W defects in addition to type V and P defects. The boxed areas are representative selected areas (2 μm x 2 μm) in which defect type densities were counted.

such as elasticity and mechanical robustness.[19] The central question is why the addition of PEG to the silica sol-gel mitigates the formation of defect structures. It is likely that the presence of PEG occupies a sufficient number of silanol groups that the silica matrix does not "cure" (*i.e.* form Si-O-Si bonds) fully, thereby reducing contraction in the formed material and leading to increased elasticity. We will explore this possibility using FTIR and thermogravimetric analysis (*vide infra*).

To evaluate the nature of the matrix enhancement produced by the addition of PEG to the silica sol-gel, it is important to consider both the chemical structure and the thermal properties of the resulting hybrid material. We consider first the effect of PEG loading in hybrid, sol-gel solutions. We have made hybrid systems for deposition on a nanoparticle scaffold with PEG

loadings of 0 wt%, 10 wt%, 20 wt% and 30 wt% (M_n = 2,000 g/mol). Although the addition of PEG improves the quality of the matrix, increasing the polymer loading results in the appearance of defects on its surface, as is seen by comparing Figs. 2.4 and 2.5.

At this point it is important to consider how the characterization of defects can be organized for such systems. Clearly, defect structures exist on several different length scales and to speak simply of a defect density is a misleading oversimplification. For this reason we identify five different types of defects. These are cracks, void defects, pore defects, hole defects and wall defects. Cracks are breaks in the inverse opal structure and can range from macroscopic (Fig. 2.4, center) to more localized in extent (Fig. 2.4, right). For the inverse opal structures we report here, the expected void diameters are from 0.23-0.26μm. Voids are considered to be defective if their diameters are less than 0.20 μm or greater than 0.29μm ("V", Fig. 2.6a). In certain instances, void defects are of sufficient size to encompass more than one void, causing disruption of inter-void walls both in-plane and between planes of the inverse opal structure (“H”, Fig. 2.6b). Such defects are termed hole defects. In a regular inverse opal structure based on a hexagonal close packed nanosphere multilayer structure, there are three pores that can be seen in each void. These pores correspond to the three point contacts made by each nanosphere in the scaffold with its under-layer, and interlayer dislocations or mis-registrations cause disruptions in this pattern. When a void has more or less than three pores, it is characterized as a pore defect (“P”, Figs. 2.6a,b). The fifth type of defect is termed a wall defect (“W”, Figs. 2.6a,b). The normal thickness of the walls between voids is less than 0.045 μm and wall thickness greater than 0.05μm are considered to be defective. We have not placed a lower bound on this type of defect because the partial or complete absence of a wall leads to a hole-type defect.

Defect densities were determined by counting the number of defects of each type per unit area (Table 2.1). Such a reporting of defect density relies on the measurement of multiple samples to provide reasonable accuracy. The structures we report are reproducible in terms of defect densities for each composition, despite the uniqueness of each individual structure. The addition of PEG to the sol gel significantly decreases the appearance of cracks in the inverse opal structure and depending on the density of pore defects. The most regular inverse opal structure, in terms of P type defects, appears for 10 wt% PEG, with substantial degradation in the regularity of the structure for higher polymer loadings. The pore defect density increases with that of wall defects. It appears (Fig. 2.7) that the wall thickness of the inverse opal structures depends on the polymer loading and we understand this in the context of PEG altering the surface tension of the sol gel precursor solution, a factor which influences the size of the pores formed. As noted above, the interactions between PEG and the silica matrix are covalent (chain-end) bonds and hydrogen bonds between the polymer ether oxygens and free silanol groups in the silica matrix. PEG is a linear polymer and morphological effects relating to the molecular weight of the polymer represent a balance between H-bonding and terminal group effects. Because of the relative contribution of each interaction, we assert that it is changes in the extent of H-bonding interactions that are responsible for the observed changes in morphology. Specifically, the presence of the polymer in the hybrid matrix serves to relax strain imposed on the silica matrix by the formation of Si-O-Si bonds. If the polymer content of the material is too high, however, it can limit the extent of Si-O-Si bond formation to the point where the integrity of the matrix is compromised. While it is not possible to quantify this effect because of the complexity and molecular scale disorder in the hybrid matrix, we attempt to characterize this balance phenomenologically through FTIR and thermogravimetric means.

One issue that is useful to consider is the relative size of the species and features in the matrix. The nanospheres used to form the scaffold structures for the formation of the matrix are *ca*. 290 nm diameter. The radius of gyration for PEG provides a qualitative measure of the expected spatial extent of the PEG-containing features in the hybrid matrix. The hydrodynamic radius of PEG in water has been determined to be *ca*. 4 nm for M_n = 20,000.[20] Given that the PEG polymers we use are all lower molecular weight, the radius of gyration will be less than 4 nm, and in any event this length scale is much shorter than

Table 2.1 Densities of different types of defects as a function of PEG loading.

Number/µm²	**Cracks**	**Void defects**	**Pore defects**	**Hole defects**	**Wall defects**
0wt%*	0.17±0.2	0.8±0.7	13.5±2.5	0	1.5±0.3
10wt%	0	1.2±1.3	3.9±1.7	0	3.0±1.9
20wt%	0	0.4±0.3	14.5±1.2	0	2.5±0.7
30wt%	0	0.6±0.4	14.0±1.7	0	4.2±2.1

Uncertainties are reported as ± 1σ for six individual determinations.

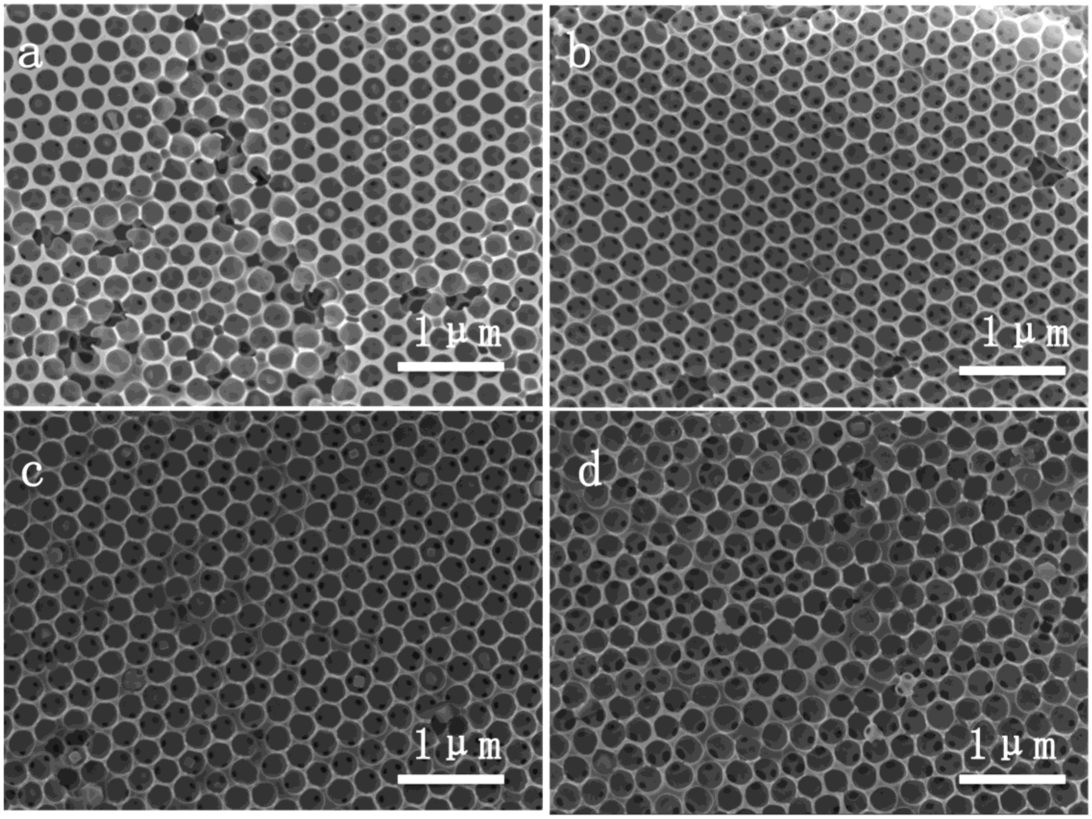

Figure 2.7 SEM images of inverse opal structures resulting from the addition of PEG (Mn = 2000 g/mol) to the sol used in matrix formation. a) 0 wt% PEG, b) 10 wt% PEG, c) 20 wt% PEG, d) 30 wt% PEG.

that of the physical features that characterize the inverse opal structure. Thus the defects seen in the hybrid matrix structure for higher molecular weight polymers cannot be attributed directly to the increase in polymer molecular weight. Rather, we believe it is the extent of matrix "curing" that is achievable for the different polymer molecular weights that is responsible for the differences we observe. We turn next to consideration of the molecular-scale organization of the hybrid matrix.

ATR-FTIR: One of the more sensitive structural probes for the hybrid matrices considered here is vibrational spectroscopy. Attenuated total reflectance (ATR) infrared spectra of the silica-PEG hybrid matrix, as an inverse opal structure, are shown in Fig. 2.8 as a function of PEG loading. The spectra are for hybrid matrices containing 0 wt%, 10 wt%, 20 wt% and 30 wt% PEG (M_n = 2,000 g/mol), as indicated. Also shown is the ATR-FTIR spectrum of PEG (top). Based on the spectra of PEG and of silica, we can assign the Si-O-Si asymmetric stretching mode at 1067 cm^{-1} and at 1108 cm^{-1} (shoulder), and the C-O-C symmetric stretching band at 1097 cm^{-1}. By increasing the PEG loading, the C-O-C peak shifts from 1030 cm^{-1} to 1100 cm^{-1}, consistent with the introduction of PEG into the silica sol-gel system. The CH_2 bending and wagging modes appear at 841 cm^{-1}, 1146 cm^{-1}, 1279 cm^{-1}, 1341 cm^{-1} and 1467 cm^{-1}, and the CH_2 asymmetric stretch at 2882 cm^{-1}.[15,21] The peak at 950 cm^{-1} is assigned to the silanol Si-O symmetric stretch and the peak at 958 cm^{-1} is $-CH_2$ rocking.[15,21] The absence of a peak in the vicinity of 3500 cm^{-1} indicates that there are few residual silanol functionalities that are not involved in H-bonding. What is important to note is the changes associated with the addition of PEG to the hybrid matrix. We focus primarily on the CH stretching region because that is the most information-rich in terms of the polymer-silica interactions. For both silica (only) and PEG (only), there are no significant spectral features in the vicinity of 3700 cm^{-1} and we understand this in terms of the comparative absence of silanol groups for silica and small number of terminal functionalities for PEG. For 20 wt % and 30 wt % PEG in silica, there are measurable bands in the 3700 cm^{-1} region, indicating the presence of unassociated silanol functionality in the silica matrix.[22] For 10 wt % PEG, there is relatively little feature in this region, suggesting much less unassociated silanol functionality. This finding is consistent with only modest structural disruption being imposed by 10 wt % PEG, but higher PEG loadings giving rise to structural disruption that is more extensive, presumably by preventing Si-O-Si linkages from being formed to their fullest extent. We assert that it is the inability to form Si-O-Si linkages extensively that is correlated with the increase in structural defects in the inverse opal structures. Taken collectively, the ATR-FTIR show that the PEG incorporates into the sol-gel matrix and that the organization of both the polymer and the silica matrix depends on the amount of polymer present.

Thermogravimetric Analysis (TGA) analysis can be useful in evaluating the structural integrity of the hybrid matrix. Approximately 10 mg of the inverse opal on the porous alumina substrate was heated to 750 ºC in an alumina pan.[23] Because the inverse opal samples were bound to the porous alumina substrate, it is not possible to know the mass of each component, and the weight loss curves were normalized to the same baseline in order to compare trends in the data (Figs. 2.9 and 2.10). The absolute weight loss is not the focus of these results. The TGA measurements provide information on the relative thermal stability of the silica-PEG inverse opal matrix as a function of matrix composition. There are clear trends in the TGA data.

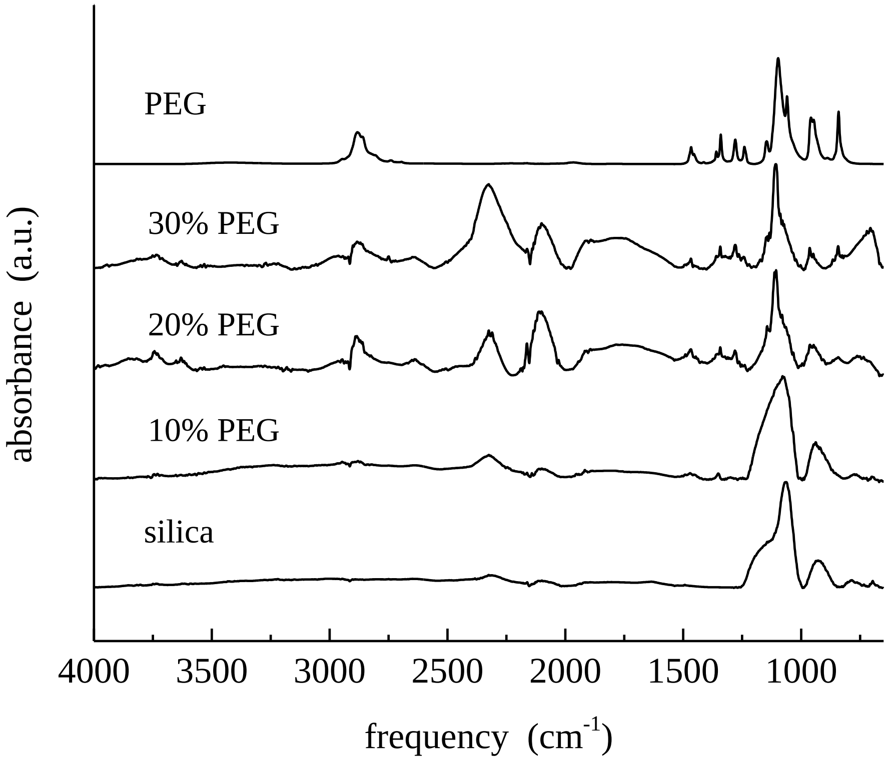

Figure 2.8 Infrared spectra of (bottom to top) 0 wt%, 10 wt%, 20 wt% and 30 wt% PEG (Mn=2,000 g/mol) in silica-PEG inverse opal matrix, and pure PEG (Mn = 2000 g/mol).

The first feature of note is that the thermal profile for PEG is a clean step-wise change at ~ 380 ºC, indicative of the decomposition of the polymer backbone. For the silica matrix, however, there is a more gradual change with increasing temperature. We attribute this loss to the progressive dehydration of silanol groups and, the formation of Si-O-Si linkages where it is structurally feasible. It is worth noting that the addition of PEG increases the thermal stability of the silica sol-gel prior to curing, and for temperatures below ca. 300 ºC. This result is different with the traditional organic-inorganic hybrids, which exhibit increased thermal stability with increasing inorganic component content. A likely explanation for our results is incomplete curing of the silica-sol gel. The samples were cured for 2 hours at 200 ºC and TGA trace changes were observed. The network might experience further condensation and form larger scale networks. During further curing at 200 ºC, the reaction of "dangling" bonds to form the bridging bonds is possible.[24] The thermal decomposition curves for silica and the hybrid matrix with 10 wt% PEG are similar, and both are different than the (similar) curves for 20 and 30 wt%. We understand these differences in terms of the extent of structural disruption within the hybrid matrix imposed by the presence of PEG. What is somewhat surprising is the similarity of the TGA data for the silica matrix and the hybrid matrix with 10 wt% PEG. These two matrices are characterized by the greatest difference in macroscopic morphology while retaining the greatest similarity in terms of thermal properties. This is a matter that remains under investigation. The overall trend in the TGA data as a function of matrix composition is that the thermal properties progress qualitatively from being silica-like to being PEG-like, but the trend is not a smooth function of matrix composition.

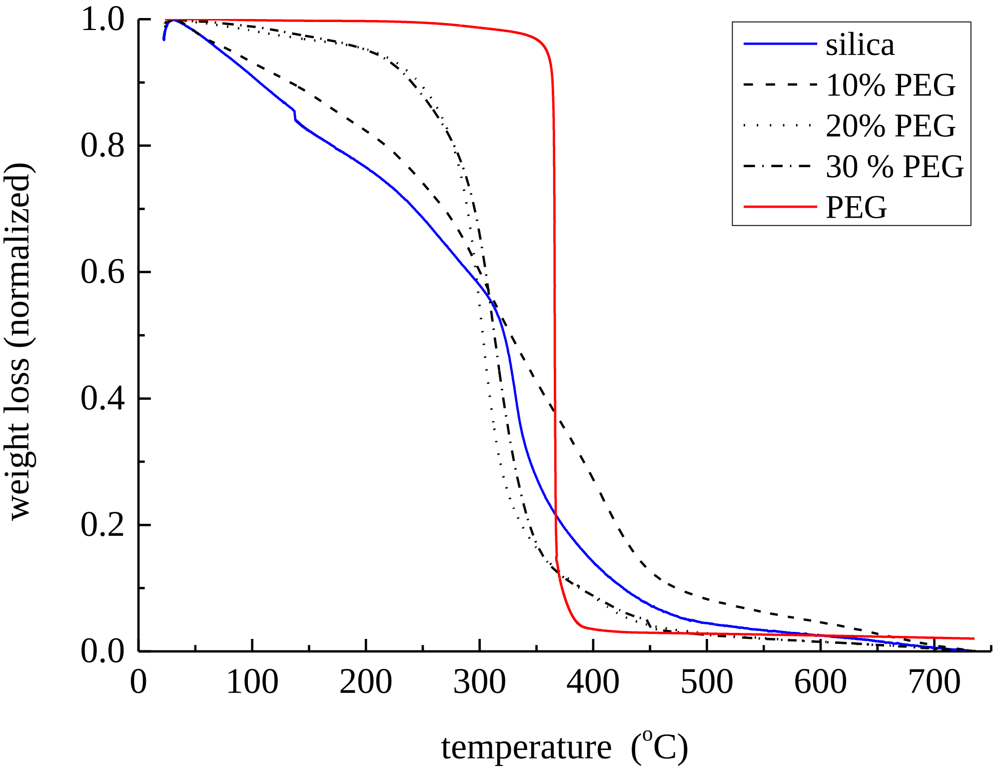

Figure 2.9 Thermogravimetric analysis of silica-PEG inverse opal structures with PEG loadings of 0 wt%, 10 wt%, 20 wt%, 30 wt% and pure PEG, without curing at 200 ºC for two hours.

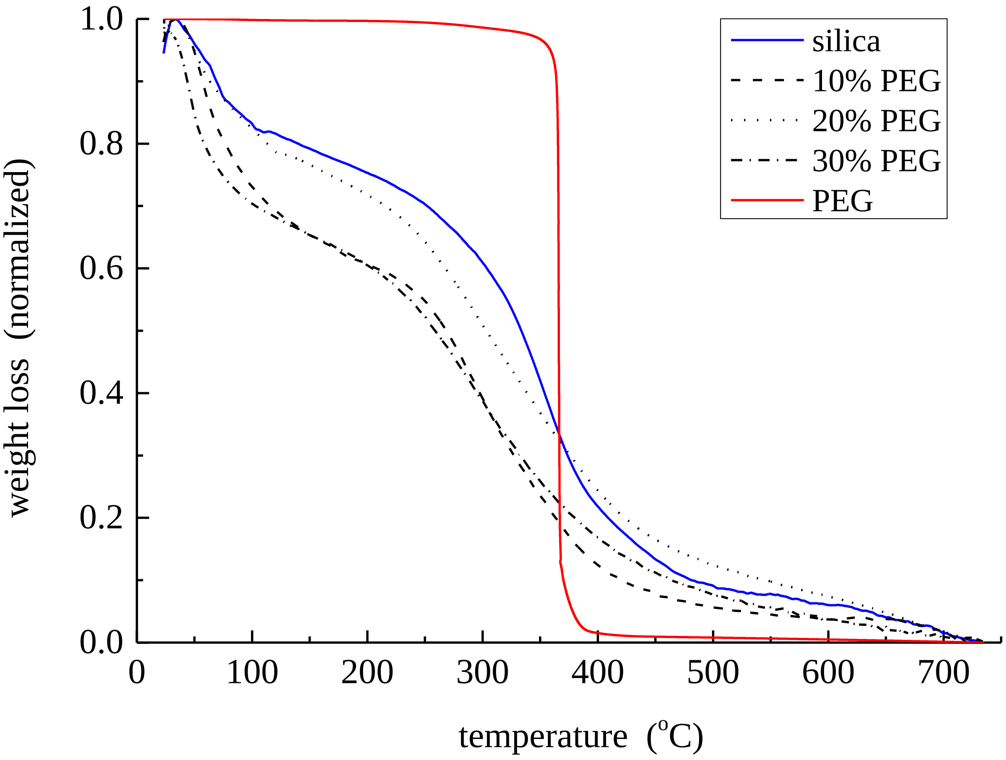

Figure 2.10 Thermogravimetric analysis of silica-PEG inverse opal structures with PEG loadings of 0 wt%, 10 wt%, 20 wt%, 30 wt% and pure PEG, after initial curing at 200oC for 2 hours.

2.4.2 Effect of PEG molecular weight on the hybrid matrix.

In addition to the effect of matrix composition, it is also important to consider the effect of PEG molecular weight on the morphology and properties of the hybrid matrix. To evaluate the PEG molecular weight dependence, we used PEG with molecular weights of 750 g/mol, 2,000 g/mol, 10,000 g/mol, each at 10 wt% loading in the sol-gel solution. It is shown in Table 2 that no cracks appear with PEG of any molecular weight loading in matrix. Increasing the molecular weight of PEG in the hybrid matrix influences the resulting matrix structure, as shown in Fig 2.11. The number of void, wall and pore defects for 10,000 g/mol PEG loading is lower than is seen for PEG of 2,000 g/mol, although this is not clear based on casual inspection. The reason for this is that the larger hole area takes the space that would have been occupied by regular voids, and the actual number of void, wall and pore defects that result from this vacancy are not counted. This finding does not mean that highest molecular weight PEG necessarily minimizes the defect density in these materials. Rather, we find that once the molecular weight of the PEG increases to 10,000 g/mol, the walls between voids cannot connect consistently and relatively large holes are formed that are sufficiently deep to access lower layers of the structure. For these systems, hole defects become a critical issue that affects the utility of these materials.

We understand the effect of molecular weight in the same context as that of the mass loading. The only expected difference between these two variables is the ratio of end group (Si-O-C) bonds to silanol H-bonds, but the effect of adding more polymer to the matrix (i.e. increasing the number of H-bonds between silanol groups and the polymer backbone) will be the same, and this is found to be the case experimentally.

While it is clear from the SEM micrographs that the organization of the inverse opal structures depends on the composition of the hybrid matrix, attempting to quantitate such organization poses a challenge. Three-dimensional, periodic micro/nanostructured materials such as inverse opals diffract photons from the lattice of dielectric planes. When the refractive index is large enough, a complete photonic band gap is formed in which Bragg diffraction inhibits a range of wavelengths from propagating through the photonic crystal. This condition can result in the localization of photons and the bands are manifested as brightly colored reflections and an optical filtering effect.[25,26] The optical properties of these materials are influenced by their structural parameters, specifically the topology, symmetry, defect density and refractive index contrast inside the photonic crystal determine its optical properties.[26] We can assess the extent of structural organization and defect density by examining the reflective properties of the samples.[27] Through the use of an integrating sphere reflectance accessory to a UV-visible spectrometer, reflectance measurements of opaque solids or powders, and total transmittance scans of translucent films and scattering creams can be recorded. The data presented in Fig. 2.12 show the UV-visible reflectance spectrum of inverse opal structures containing PEG with molecular weights of 750 g/mol, 2,000 g/mol and 10,000 g/mol. The highest contrast peak (*ca*. 270 nm) is observed for the inverse opal made with PEG of $M_n = 750$ g/mol. Increasing the molecular weight of PEG produces a peak, with wavelength consonant with the diameter of the void spaces (*ca*. 290 nm), that is characterized by broad shoulders, consistent with the existence of larger size scale void regions, or defects. It is important to note that the data for the hybrid matrix containing 10 wt% PEG of $M_n = 750$ g/mol is characterized by

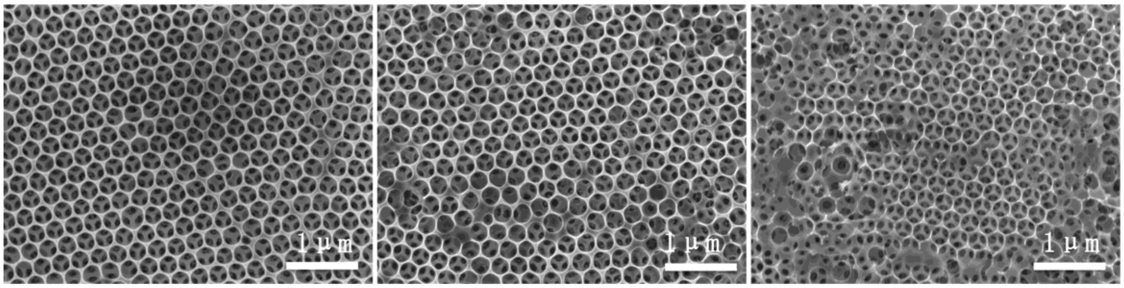

Figure 2.11 SEM images of inverse opal structure made with 10 wt% PEG of different molecular weights (from left to right): 750 g/mol, 2,000 g/mol and 10,000 g/mol.

Table 2.2 Defect densities as a function of PEG molecular weight (10 wt. % loading)

Number/μm^2	**Cracks**	**Void defects**	**Pore defects**	**Hole defects**	**Wall defects**
M_n=750g/mol[a]	0	0.08±0.13	2.16±1.30	0	0.75±0.89
M_n=2000g/mol	0	1.17±1.33	3.92±1.71	0	2.96±1.91
M_n=10000g/mol	0	0	2.42±0.82	1.29±0.43	1.29±0.9

[a] PEG is methoxy-terminated.

Uncertainties are reported as ± 1σ for six individual determinations.

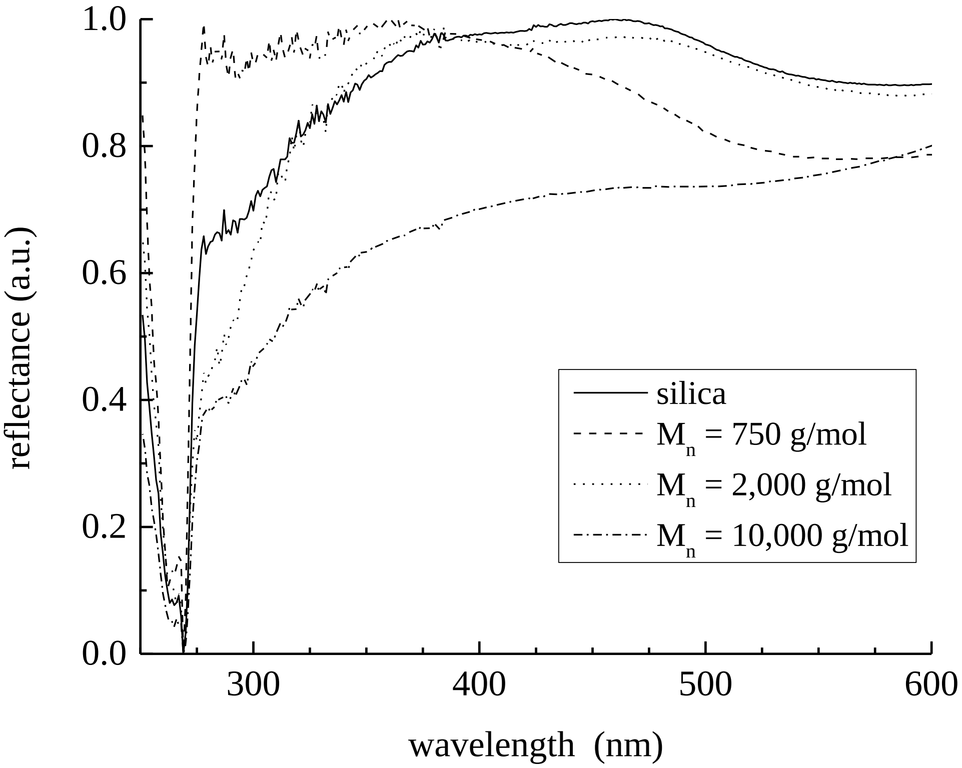

Figure 2.12 Normalized UV- visible reflectance spectra of inverse opal structures with PEG of Mn = 750 g/mol, 2,000 g/mol and 10,000 g/mol. Data were acquired using an integrating sphere

a band with a much less prominent shoulder than that seen for the inverse opal structure made using silica sol-gel only.We attribute the morphology differences of nanoporous structure correlation with the molecular weight to the micro-scale phase separation. Studies on the silica-PEG hybrid by Jung *et al.*[19] (in non-inverse opal structural format) indicate that such differences are considered to be the result of micro-scale phase separation related to the volume of trapped PEG. Takahashi's results[28] showed the characteristic length scale of phase separation depends strongly on the amount of polymer, the molecular weight of the polymer, the solvent composition and the pH. The phase separation that occurs in the silica-PEG sol-gel clearly influences the morphology of resulting inverse opal structure, and the critical H-bonding interactions between the polymer and the silica regions of the matrix are the chemical means by which these separated nano-domains interact. Phase separation mechanisms of silica-PEG/PEO hybrid bulk materials (in non-inverse opal strucutural format) has been studied since 1990s by Surviet et al. [29]and Wilkes et al.[30] For shorter polymer chains, like PEG 750, the chance of being encapsulated or forming a mixed phase with condensed TEOS is higher than it is for longer polymer chains. For a longer chain such as PEG 10,000, the formation of an oligomer-rich phase and condensed TEOS clusters is more likely. Therefore, compositional heterogeneity may be seen more readily at the surface of the matrix formed with higher molecular weight PEG.[30] ATR infrared spectra of the silica-PEG inverse opal structures were also studied as a function of PEG molecular weight (Fig. 2.13). Increasing polymer loading and molecular weight both appear to have a structurally perturbative effect on these composite materials. The observed bands (a composite of silica and PEG bands in the ~1000 cm^{-1} – 1200 cm^{-1} region) undergo a shift to higher frequency with the increasing PEG molecular weight. In

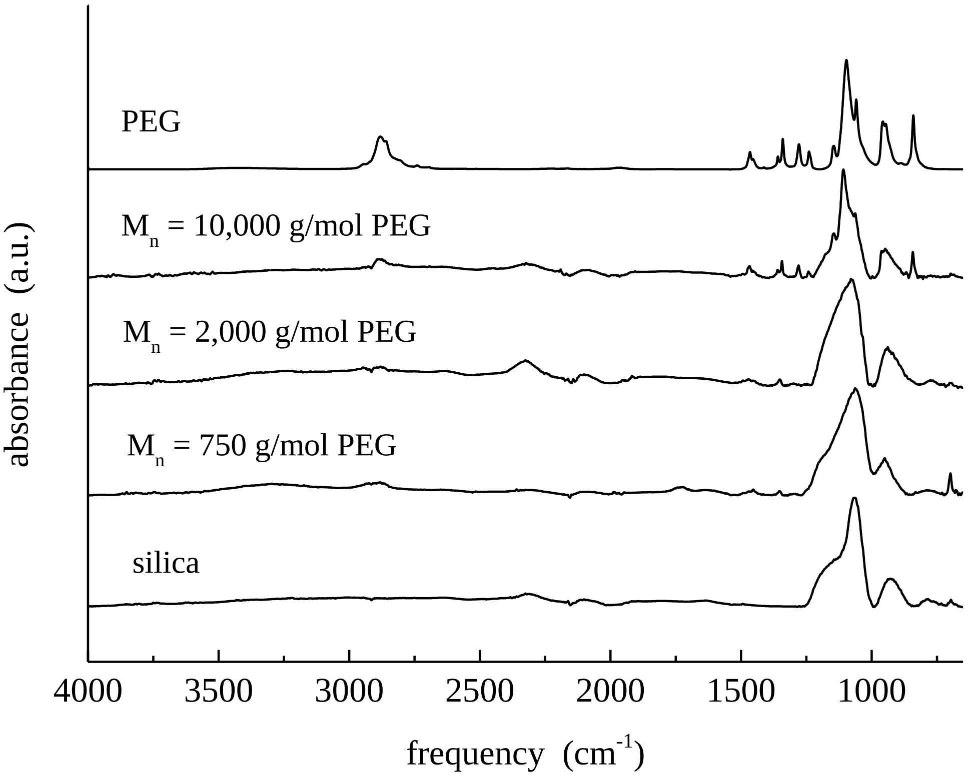

Figure 2.13 ATR spectra of 10 wt% PEG with Mn = 750 g/mol, 2,000 g/mol, 10,000 g/mol, and pure PEG (Mn = 2,000 g/mol), respectively, from the bottom to top.

analogy with the data shown in Fig. 6, the peaks at 1180 cm^{-1}, 1276 cm^{-1}, 1345 cm^{-1} and 2900 cm^{-1} confirm the presence of PEG. While these data do not address the issue of spatial heterogeneity directly, they provide evidence that there is strong interaction between the two phases, as would be expected based on the SEM data on these systems.

2.5 Conclusion

Traditional silica sol gel inverse opal structures form significant cracks and defects during the curing process due to shrinkage of the matrix. Addition of poly(ethylene glycol) to the silica sol-gel mitigates cracking and allows for the formation of a matrix containing comparatively few defects. Five kinds of defect density were investigated quantitatively. The morphology of the hybrid matrix depends on the amount of PEG added and its molecular weight. Increases in polymer loading beyond 10 wt. % or the use of higher molecular weight PEG leads to structural disruption of the inverse opal matrix structure. The conformation of interactions between the polymer and silica network components mediates the morphological and thermal properties of the hybrid matrix material.

This work points the way to the use of other more structurally versatile polymers as potential components in hybrid matrix structures. In addition to the matrix components, there are also structural and physical issues to be addressed, including more thorough characterization of the polymer-matrix interactions and the interactions between the matrix and its support. These issues will be important for further improvements in the construction of low-defect hybrid matrix inverse opal materials.

REFERENCES

REFERENCES

1. Judeinstein, P.; Sanchez, C. Hybrid Organic-Inorganic Materials: A Land of Multidisciplinarity. J. Mat. Chem. 1996, 6, 511-525.

2. Schottner, G. Hybrid Sol-Gel-Derived Polymers: Applications of Multifunctional Materials. Chem. Mater. 2001, 13, 3422-3435.

3. Mammeri, F.; Le Bourhis, E.; Rozes, L.; Sanchez, C. Mechanical Properties of Hybrid Organic-Inorganic Materials. J. Mat. Chem. 2005, 15, 3787-3811.

4. Pierre, A.; Rigacci, A. In Aerogels Handbook; Aegerter, M. A., Leventis, N., Koebel, M. M., Eds.; Springer New York: 2011, p 21-45.

5. Shea, K. J.; Loy, D. A. Bridged Polysilsesquioxanes. Molecular-Engineered Hybrid Organic-Inorganic Materials. Chem. Mater. 2001, 13, 3306-3319.

6. Stein, A.; Schroden, R. C. Colloidal Crystal Templating of Three-Dimensionally Ordered Macroporous Solids: Materials for Photonics and Beyond. Curr. Opin. Solid State & Mat. Sci. 2001, 5, 553-564.

7. Guliants, V. V.; Carreon, M. A.; Lin, Y. S. Ordered Mesoporous and Macroporous Inorganic Films and Membranes. J. Membr. Sci. 2004, 235, 53-72.

8. Zeng, F.; Sun, Z. W.; Wang, C. Y.; Ren, B. Y.; Liu, X. X.; Tong, Z. Fabrication of Inverse Opal Via Ordered Highly Charged Colloidal Spheres. Langmuir 2002, 18, 9116-9120.

9. Velev, O. D.; Jede, T. A.; Lobo, R. F.; Lenhoff, A. M. Microstructured Porous Silica Obtained Via Colloidal Crystal Templates. Chem. Mater. 1998, 10, 3597-3602.

10. Hench, L. L.; West, J. K. The Sol Gel Process. Chem. Rev. 1990, 90, 33-72.

11. Ciriminna, R.; Fidalgo, A.; Pandarus, V.; Beland, F.; Ilharco, L. M.; Pagliaro, M. The Sol-Gel Route to Advanced Silica-Based Materials and Recent Applications. Chem. Rev. 2013, 113, 6592-6620.

12. Fang, J. F.; Xuan, Y. M.; Li, Q. A. Preparation of Polystyrene Spheres in Different Particle Sizes and Assembly of the Ps Colloidal Crystals. Sci. China-Tech. Sci. 2010, 53, 3088-3093.

13. Hatton, B.; Mishchenko, L.; Davis, S.; Sandhage, K. H.; Aizenberg, J. Assembly of Large-Area, Highly Ordered, Crack-Free Inverse Opal Films. Proc. Nat. Acad. Sci. USA 2010, 107, 10354-10359.

14. Velev, O. D.; Lenhoff, A. M. Colloidal Crystals as Templates for Porous Materials. Curr. Opin. Coll. Int. Sci. 2000, 5, 56-63.

15. Vong, M. S. W.; Bazin, N.; Sermon, P. A. Chemical Modification of Silica Gels. J. Sol-Gel Sci. Tech. 1997, 8, 499-505.

16. Sun, Z. K.; Deng, Y. H.; Wei, J.; Gu, D.; Tu, B.; Zhao, D. Y. Hierarchically Ordered Macro-/Mesoporous Silica Monolith: Tuning Macropore Entrance Size for Size-Selective Adsorption of Proteins. Chem. Mater. 2011, 23, 2176-2184.

17. Gornowich, D. B.; Blanchard, G. J. Enhancement of Enzyme Activity by Confinement in an Inverse Opal Structure. J. Phys. Chem. C 2012, 116, 12165-12171.

18. Wen, J. Y.; Wilkes, G. L. Organic/Inorganic Hybrid Network Materials by the Sol-Gel Approach. Chem. Mater. 1996, 8, 1667-1681.

19. Jung, H. Y.; Gupta, R. K.; Seo, D. W.; Kim, Y. H.; Whang, C. M. Preparation and Characterization of Hybrid Silica-Poly(Ethylene Glycol) Sonogel. Bull. Korean Chem. Soc. 2002, 23, 884-890.

20. Linegar, K. L.; Adeniran, A. E.; Kostko, A. F.; Anisimov, M. A. Hydrodynamic Radius of Polyethylene Glycol in Solution Obtained by Dynamic Light Scattering. Colloid J. 2010, 72, 279-281.

21. Jung, H. Y.; Gupta, R. K.; Oh, E. O.; Kim, Y. H.; Whang, C. M. Vibrational Spectroscopic Studies of Sol-Gel Derived Physical and Chemical Bonded Ormosils. J Non-Cryst Solids 2005, 351, 372-379.

22. Griffith, G. W. Quantitation of Silanol in Silicones by Ftir Spectroscopy. Ind. Eng. Chem. Prod. Res. Dev. Rev. 1984, 23, 590-593.

23. Grandi, S.; Magistris, A.; Mustarelli, P.; Quartarone, E.; Tomasi, C.; Meda, L. Synthesis and Characterization of Sio2-Peg Hybrid Materials. J. Non-Cryst. Solids 2006, 352, 273-280.

24. Yoldas, B. E. Hydrolysis of Titanium Alkoxide and Effects of Hydrolytic Polycondensation Parameters. J. Mat. Sci. 1986, 21, 1087-1092.

25. Blanco, A.; Chomski, E.; Grabtchak, S.; Ibisate, M.; John, S.; Leonard, S. W.; Lopez, C.; Meseguer, F.; Miguez, H.; Mondia, J. P.; Ozin, G. A.; Toader, O.; van Driel, H. M. Large-Scale Synthesis of a Silicon Photonic Crystal with a Complete Three-Dimensional Bandgap near 1.5 Micrometres. Nature 2000, 405, 437-440.

26. Li, Y.; Piret, F.; Leonard, T.; Su, B. L. Rutile Tio2 Inverse Opal with Photonic Bandgap in the Uv-Visible Range. J. Coll. Int. Sci. 2010, 348, 43-48.

27. Rengarajan, R.; Mittleman, D.; Rich, C.; Colvin, V. Effect of Disorder on the Optical Properties of Colloidal Crystals. Phys. Rev. E 2005, 71

28. Takahashi, R.; Nakanishi, K.; Soga, N. Aggregation Behavior of Alkoxide-Derived Silica in Sol-Gel Process in Presence of Poly(Ethylene Oxide). J. Sol-Gel Sci. Tech. 2000, 17, 7-18.

29. Surivet, F.; Lam, T. M.; Pascault, J. P.; Pham, Q. T. Organic Inorganic Hybrid Materials .1. Hydrolysis and Condensation Mechanisms Involved in Alkoxysilane-Terminated Macromonomers. Macromol. 1992, 25, 4309-4320.

30. Huang, H.-H.; Wilkes, G. Structure-Property Behavior of New Hybrid Materials Incorporating Oligomeric Poly(Tetramethylene Oxide) with Inorganic Silicates by a Sol-Gel Process. Polym. Bull. 1987, 18, 455-462.

CHAPTER 3: Catalytic assessment of glucose conversion with porous glass frit-supported glucose oxidase

3.1 Introduction

Low defect density polymer-sol gel composite inverse opal structures have been described in Chapter 2. The high surface area and the porosity of inverse opals offer great potential for catalytic applications. The Blanchard group has reported on an enhancement in enzyme activity due to confinement in a silica inverse opal structure.[1] Enhancement of the turnover rate of glucose oxidase (GOx) bound to an inverse opal structure was observed relative to GOx bound to a planar silica surface and free in solution. Both the pore size and void volume of inverse opal structures are controllable through the size of the (polymer) spheres used during the formation of the inverse opal scaffold. These physical properties are important in terms of the probability of a substrate-enzyme reaction event occurring. A key limitation to this approach is the existence of cracks and other structural defects in inverse opal materials.

The work presented in Chapter 2 demonstrated improved quality silica-based inverse opal structures through the reduction in visible defects afforded by using a hybrid matrix, an advance that is expected to facilitate other applications of these materials. However, the comparative fragility of inverse opal matrices and porous alumina supports, and the relatively complicated fabrication protocols pose challenges to the utilization of these materials on large and/or industrial scales. To accomplish our goals of performing heterogeneous catalytic reactions in support of biomass refinery processes, several catalyst support materials have been demonstrated, including mesoporous silica,[2] silica nanospheres,[3] zeolites[4] and polymeric matrixes.[5] Several physical requirements obtain for practical catalyst supports, including the ability to withstand reactant flow through the porous medium, relatively high surface area, ease of permeability, physical and chemical stability, the ability to functionalize the surface of the support to allow binding of enzymes and other catalysts to the support surface, facile device fabrication and easy post-reaction cleanup. We proposed the use of porous glass filter frits as catalyst supports based on their structural integrity, commercial availability, range of available pore sizes, ability to be chemically functionalized, relatively high surface area combined with porosity, high thermal, chemical and mechanical stability, and reusability.[6]

In this Chapter, we demonstrate that GOx confined in a porous glass filter frit is a practical, functional catalyst support and the turnover rate is comparable to the enzyme being supported on a silica inverse opal matrix.[7] The extent of spatial confinement is related directly to the catalytic reaction turnover rate. The dimensional irregularity of the porous frit material could lead to a number of deleterious phenomena. For example, the large pore regions could lead to either loss of enzyme or lack of exposure to reactant, and small pore regions could inhibit the diffusion of either enzyme during functionalization or reactant during the flow reaction, diminishing the rate of reaction.[5] The diameter(s) of the pores in the porous catalyst supports determine the average residence time of a molecule within the matrix and, during this residence time, the reactant molecule will execute diffusional motion.

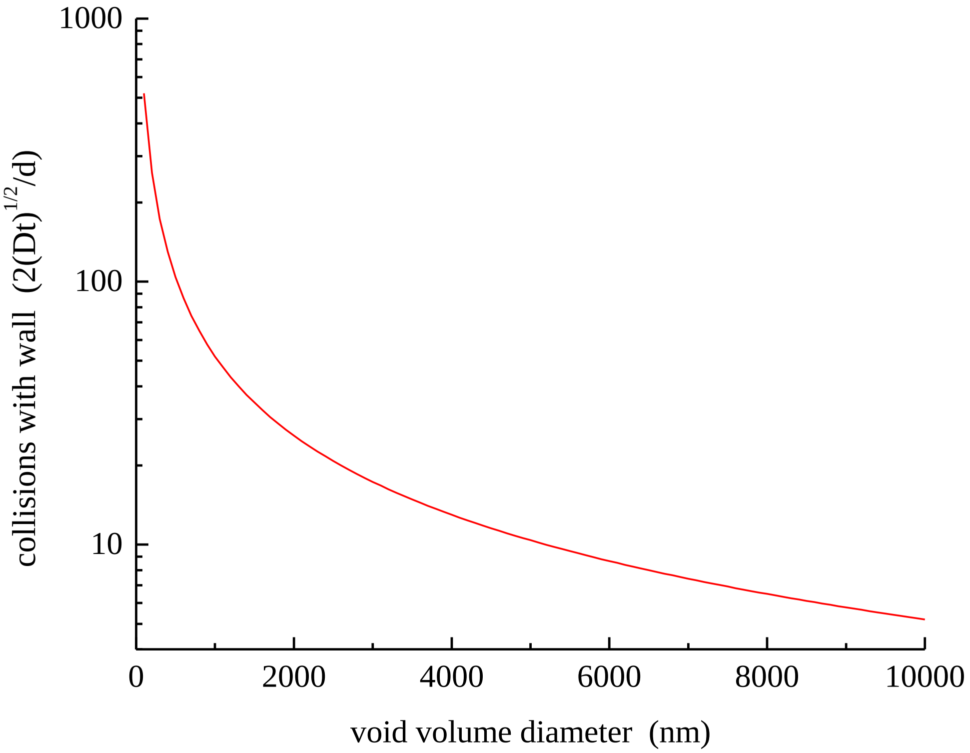

Figure 3.1 Dependence of number of collisions of reactant with walls of a confined volume as a function of the size of the confining volume. Number of collisions with the wall is proportional to the probability of a catalytic reaction event occurring.

The characteristic diffusion length is $2(Dt)^{1/2}$, where D is the diffusion constant, represents the average distance the reactant molecule travels while in the void space (Fig. 3.1). We can estimate the probability of a reactive substrate-enzyme interaction in a flow-through system by plotting the number of expected molecule-surface interactions expected ($2(Dt)^{1/2}/d$) as a function of pore diameter, d. The smaller pore size, the more reactant-pore-surface interactions are experienced and the higher the probability of a catalytic reaction event occurring. We have found that both enzymes and metallic nanoparticles can be incorporated into porous glass frits and they can exhibit relatively efficient catalytic behavior under flowing reaction conditions. In this Chapter we focus on the incorporation of GOx into the porous glass frit supports and characterize the efficiency of its catalytic reaction with glucose.

3.2 Experimental

Chemicals: (3-Aminopropyl)triethoxysilane (APTES, ≥99%, Sigma-Aldrich), glutaraldehyde (50 wt% in water, Sigma-Aldrich), toluene (≥99.5%, Mallinckrodt), glucose oxidase from *Aspergillus Niger* (GOx, lyophilized powder, Aldrich), β-D-glucose (ACS reagent grade, Fluka), sodium acetate buffer (50 mM sodium carbonate, sodium bicarbonate, sodium hydroxide, acetate acid in MilliQ water, pH 4), hydrogen peroxide (30% (w/w) in water, Fisher Chemical), ferrous sulfate heptahydrate (ACS reagent grade, Sigma-Aldrich)

Enzyme immobilization. Glass filter frits (25 mm diameter, 3.5 mm thickness, grade E, Ace Glass) were cleaned with piranha solution (3 parts 18 M H_2SO_4 to 1 part 30% H_2O_2) for one hour and soaked in 0.05 M hydrochloric acid solution overnight to remove any residual hydrogen peroxide in the pores. The glass frits were heated in an oven to 70 °C to remove moisture, followed by immersion in 10% (v/v) APTES in toluene for 30 minutes at 35 °C. The dried and aminosilanized glass frits were exposed to 1% (v/v) aqueous glutaraldehyde solution. The resulting supports were immersed in a 1 mg/mL GOx solution in sodium acetate buffer (pH 4) for 24 hours at 4 °C. The resulting GOx-modified glass frit support was stored in sodium acetate buffer at 4 °C when not in use.

Flow-through experiment. 100 mM β-D-Glucose in sodium acetate buffer (pH 4) was flowed through the enzyme-functionalized glass frit which was mounted in an in-house-made Teflon® flow cell. Reactant flow was controlled by a syringe pump operating at flow rates of 25 μL/min or 50 μL/min at room temperature. Eluent aliquots were collected every 20 minutes.

Glucose oxidase assay. β-D-Glucose is oxidized to D-gluconolactone with glucose oxidase, and spontaneously hydrolyzed to the D-gluconic acid and H_2O_2. Fenton's assay[8] was used to determine the H_2O_2 produced by the oxidation of glucose and thereby evaluate the enzyme catalytic activity. Fenton's reagent (FR) is 1 mM ferrous sulfate in sodium acetate buffer (pH 4). Glucose assay based upon the interaction between glucose oxidase and Fenton reagent is depicted by Woodward:[9]

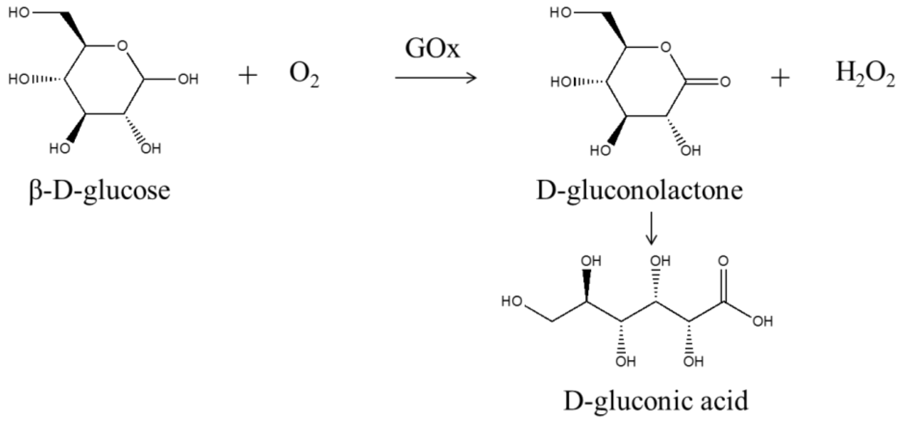

$$H_2O_2 + 2Fe^{2+} + 2H^+ \rightarrow 2Fe^{3+} + 2H_2O$$

Hydrogen peroxide oxidizes Fe^{2+} to Fe^{3+} resulting in an increase in a near UV absorbance which is measured at 340 nm. The molar absorptivity of this band has been quantitated before ($\varepsilon = 3{,}000$ L/mol-cm).[9] A 1.5 mL aliquot of Fenton reagent and 1.5 mL aliquot of buffer solution was mixed and added to a quartz cuvette along with 0.2 mL of the collecting sample to perform the assay. A calibration curve was generated with standard samples of hydrogen peroxide solution to quantitate the conversion of glucose.

Ultraviolet-visible spectroscopy (UV-Vis). UV-visible absorbance data were acquired using an ATI UNICAM UV2 UV/visible spectrometer. Data were acquired over the wavelength range of 250 nm to 400 nm at a scan rate 600 nm/min. Spectral resolution of the measurement was set to 1 nm.

Thermogravimetric Analysis (TGA). Glass frits that had been reacted with glucose oxidase were analyzed thermogravimetrically from 20 °C to 800 °C to determine the weight of the enzyme on the support. Samples were broken into small pieces and dried under N_2(g) before measurement. TGA measurements were performed using a Perkin Elmer TGA 7 instrument with a thermal ramp rate of 15 °C/min. from 30 °C to 120°C, under a dry N_2(g) atmosphere. Samples were maintained isothermally at 120 °C for 30 minutes to remove moisture, and then ramped to 800 °C at 15 °C/min.

3.3 Result and Discussion

Enzyme immobilization and quantification. Enzymes are biocatalysts that are not only essential to life, but several have found use in large-scale industrial processes because of their combined efficiency and selectivity for specific reactants and products. The use of enzymes is challenged by several limitations, however, including limited stability in some instances, high cost, relatively complicated separation steps for reaction clean-up, reusability, and loss of enzyme activity.[10] The immobilization of enzymes on support structures may overcome several of these drawbacks and allow the use of enzymes in multi-step cascade process, which is the ultimate goal of this research effort. The immobilization of enzymes minimizes post-reaction cleanup by facilitating the separation of the enzyme from the product, and increases the operational stability of the enzyme through the reduction of denaturing by reaction products or other agents. Immobilization can help to stabilize the activity of enzymes during reactions. There are, however, several possible issues that can occur with the immobilization of an enzyme. One such issue is denaturation of the enzyme on exposure to the chemical agents used for immobilization.[6] It is also possible that the enzyme binds to the support in such a manner that the active site is blocked, precluding substrate access.[11] It is also known that binding of the enzyme to a support can result in a structural conformation that is less than optimally active, reducing the efficiency of reaction.[12] It is thus important to investigate immobilization methods and techniques for a particular system to optimize the activity and effectiveness of the resulting bound system.

There have been several methods reported for enzyme immobilization. These include enzyme entrapment or encapsulation, self-immobilization by cross-linking, and support binding.[13] Each method has its own advantages and limitations. For entrapment or encapsulation, the enzyme is protected from the external environment, thereby minimizing issues related to mechanical shear and solvents, but this method limits mass transport and contact with substrate molecules.[14] Enzymes can be immobilized on prefabricated supports by means of physisorption, van der Waals interactions, hydrogen bonding, ionic binding or covalent bonding. Such immobilization can provide rigidity, but can also be limited by dissociation of the enzyme from the support. For self-immobilization, enzymes are aggregated through cross-linking agents without residing on the support surface. The carrier-free aggregates can grow up from 1 to 100 µm, which is too large to exit through the pores.[14] The enzyme aggregates or crystals can be physically separated from the reaction medium, but such aggregation runs the risk of rendering the enzyme active sites inaccessible.

Previous work demonstrated a novel immobilization method using a silica inverse opal matrix as the support structure for enzyme binding.[1] In this work, rather than using an inverse opal as the support, the enzyme is bound directly to a porous glass frit using the same immobilization chemistry that was used for binding to the inverse opal structure; the support structure is aminated with APTES, followed by glutaraldehyde, and then cross-linked through amino moieties on enzymes (*e.g.* Asn, Arg, Gln).[15-16]

3.3.1 Assessment of glucose conversion with glass frit-supported GOx.

A typical UV-visible absorbance spectrum of the Fenton assay is shown in Fig. 3.2 to demonstrate the absorbance maximum at 340 nm. Although higher monotonic background absorbance was observed at shorter wavelengths, the absorbance feature at 340 nm is used to quantify the conversion of glucose by GOx because the shorter wavelength background is associated with $FeSO_4$ in solution and does not change quantifiably on exposure to H_2O_2.[9] Solutions of known H_2O_2 concentration were used to establish calibration for Fenton's reagent so that catalytic glucose oxidation with GOx could be quantitated. Fig. 3.3 contains the best-fit calibration line for this analysis with a slope of 0.162 a.u./mM, an intercept of 0.0139 a.u./mM and $R^2 = 0.999$.

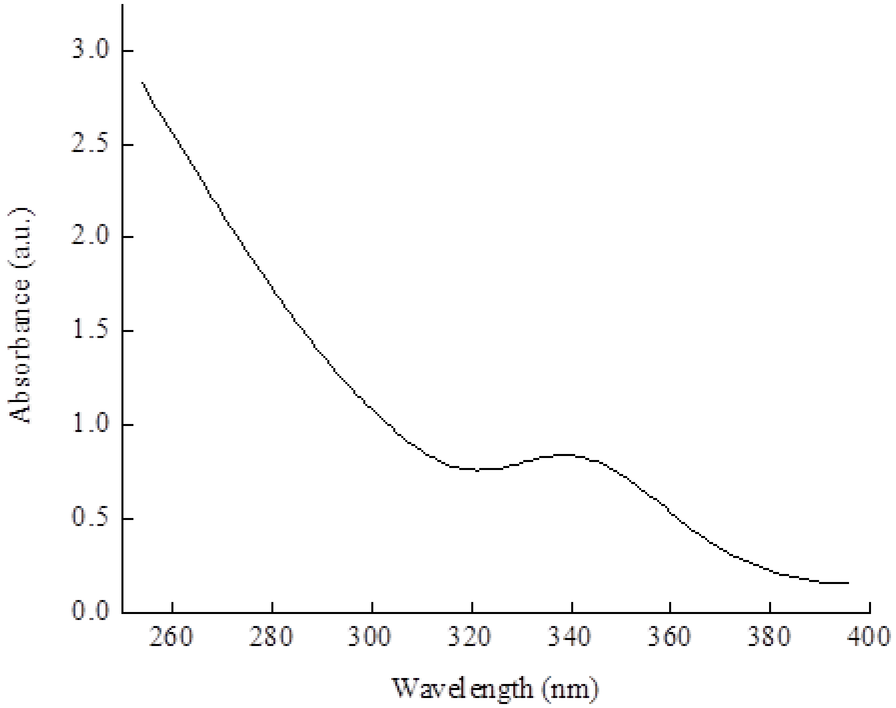

Figure 3.2 UV-visible spectrum of Fenton's reagent showing the analytical band maximum at 340 nm and a broad increasing background associated with FeSO4(aq) at shorter wavelengths.

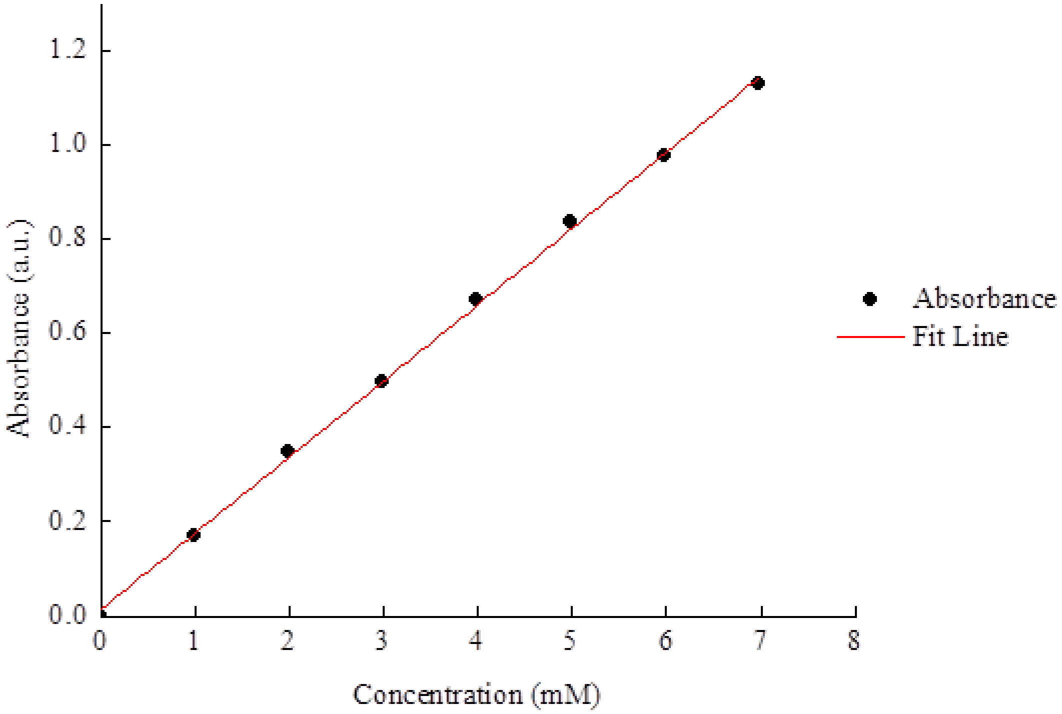

Figure 3.3 Fenton reagent calibration curve generated using known concentrations of H2O2. Absorbance was measured at 340 nm.

A solution of 100 mM β-D-glucose was flow-through a glass frit containing immobilized GOx and aliquots was collected and analyzed by Fenton's assay. The percentage conversion of 100 mM β-D-glucose to D-gluconic acid is calculated based on the production of H2O2 (Fig. 3.4). Approximately 6% of the β-D-glucose substrate has been catalyzed by GOx at the beginning of the flow-through reaction and this efficiency decreased with the increasing time for both flow rates studied (25 μL/min and 50 μL/min). This finding indicates that glucose can pass through the catalyst-decorated support structure without reacting because the reaction kinetics are comparatively slow. Comparing these results to those reported previously using an inverse opal support reveals the same extent of conversion (*ca.* 6%) of the feedstock. The catalytic efficiency of the immobilized GOx is the same for both supports even though the pore size of inverse opal support (0.2 - 1 μm) is much smaller than that of the glass frit (4 - 8 μm). One possible explanation is that the reaction is kinetically limited, and it is also possible that a simple geometric estimate of the relevant pore size and length scale may be too simplistic to account for the geometric features of these support structures.[7] Regardless of the actual reason, the commercial glass frit support is fully appropriate for use in a flow-through catalytic format. In addition, the glass frit support available commercially and is more amenable to physical and chemical manipulation than inverse opal structures on a porous alumina support.

Since the work reported earlier did not show results of β-D-glucose conversion as a

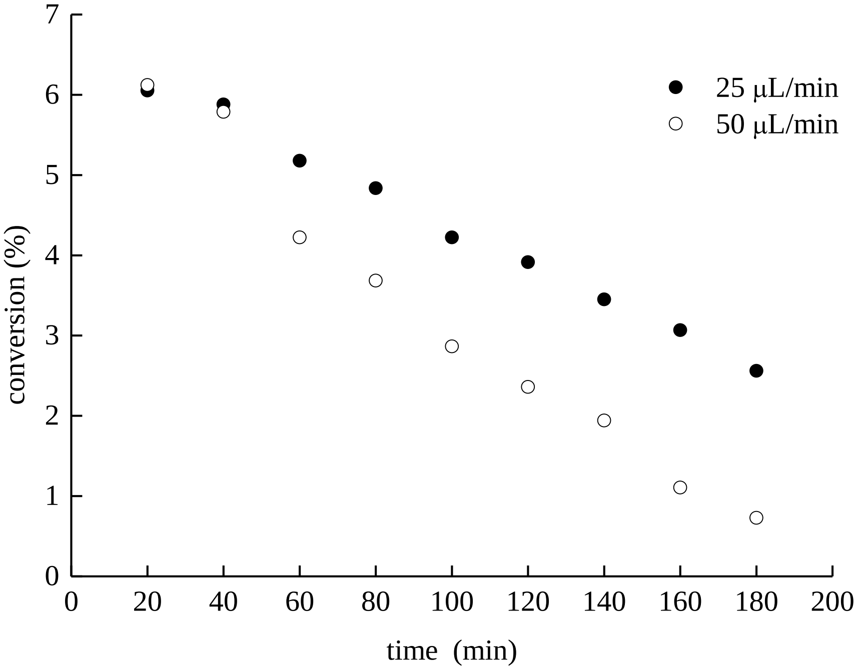

Figure 3.4 Conversion of β-D-glucose as a function of reaction run time at the flow rates indicated.

function of (flow-through) reaction time,1 no direct comparison can be made regarding the catalytic performance of the two supports over time. In this work, comparing GOx performance on a glass frit support at different flow rates (25 and 50 μL/min) reveals a clear flow rate-dependence (Fig. 3.4). The time-dependent decrease in β-D-glucose conversion for 25 μL/min flow rate is much slower than the same data acquired at a flow rate of 50 μL/min. Over a 180 min run time, the β-D-glucose conversion decreased to a level of 2.5% at flow rate of 25 μL/min, and 0.7% conversion at flow rate of 50 μL/min. These results are consistent with the residence-time dependence of the probability of substrate-enzyme interaction (Fig.3.1). There are several possible reasons for the decline in β-D-glucose conversion with increasing reaction run time, such as removal of the immobilized enzyme or denaturation/degradation of enzyme due to product (H_2O_2) formation. If the reaction kinetics are slow, then substrate is effectively saturated and the reaction is proceeding under pseudo-first order kinetics, where the product formed is directly proportional to the amount of GOx available for reaction.[17] It has been reported that GOx exhibits first-order deactivation kinetics and the slope of the time-dependence yields the first-order rate constant.[18] Oxygen was found to increase the deactivation rate constant and the product of the glucose to gluconic acid reaction catalyzed by GOx, H_2O_2, was found to deactivate the GOx more effectively than O_2.[19] Malikkides[20] concluded that the mechanism of immobilized GOx deactivation is dominated by H_2O_2 attack of the glucose-GOx complex. The accumulation of reaction products in the porous support structure can thus serve to facilitate enzyme degradation.

3.3.2 Assessment of turnover rate

Turnover rate (s^{-1}) is used to evaluate the enzymatic activity of GOx, which is defined as the number of molecules of a specified product made per catalytic site and per unit time.[21] It is known that there are two active site in the dimeric GOx protein.[22] To calculate the turnover rate of the reaction, the GOx loading in the system was quantified using thermogravimetric analysis. The glass frit supports containing immobilized GOx were weighed and broken into pieces for the TGA measurement. These data showed a weight loss of 0.28% ± 0.06% for a single glass frit sample (2.92 g) after heating to 800 °C. These data indicate that the GOx loading on the glass frit support is *ca.* 8.28 mg or 3.11×10^{16} GOx molecules. This loading on the glass frit support is substantially higher than that found on the inverse opal/PAS support, 35 μg or 1.32×10^{14} GOx molecules. Despite this difference in absolute loading, the (initial) conversion of β-D-glucose was substantially the same for both supported systems, *ca.* 6% of 100 mM glucose solution. This result reveals a much lower turnover rate (*ca.* 50 s^{-1}) for GOx immobilized on a glass frit compared to a turnover rate of 11,500 s^{-1}) for GOx immobilized on an inverse opal/PAS support. On the glass frit support, it appears that a significant fraction of the enzyme is either inactive or inaccessible to the substrate.

3.4 Conclusion

GOx immobilized on a porous glass frit support and an inverse opal/PAS support both produce *ca.* 6% initial catalytic conversion of β-D-glucose. The inverse opal support structure, however, requires multiple steps of fabrication, is physically fragile and incapable of operating as a free-standing support for flow-through catalytic reactions. Replacing the inverse opal support with a porous glass frit overcomes the physical limitations of the inverse opal structure and produces the same reaction efficiency, albeit at the expense of somewhat greater amounts of catalyst being required. The porous glass frit structure is also of use for catalytic systems that use metal nanoparticles, as we consider in Chapters 4 and 5 of this dissertation.

REFERENCES

REFERENCES

1. Gornowich, D. B.; Blanchard, G. J., Enhancement of Enzyme Activity by Confinement in an Inverse Opal Structure. *Journal of Physical Chemistry C* **2012,** *116* (22), 12165-12171.

2. Lei, C. H.; Shin, Y. S.; Liu, J.; Ackerman, E. J., Entrapping enzyme in a functionalized nanoporous support. *Journal of the American Chemical Society* **2002,** *124* (38), 11242-11243.

3. Li, H.; He, J.; Zhao, Y. F.; Wu, D.; Cai, Y. Y.; Wei, Q.; Yang, M. H., Immobilization of glucose oxidase and platinum on mesoporous silica nanoparticles for the fabrication of glucose biosensor. *Electrochimica Acta* **2011,** *56* (7), 2960-2965.

4. Wang, J.; Walcarius, A., Zeolite containing oxidase-based carbon paste biosensors. *Journal of Electroanalytical Chemistry* **1996,** *404* (2), 237-242.

5. Bezerra, C. S.; Lemos, C. M. G. D.; de Sousa, M.; Goncalves, L. R. B., Enzyme immobilization onto renewable polymeric matrixes: Past, present, and future trends. *Journal of Applied Polymer Science* **2015,** *132* (26).

6. Hartmann, M.; Kostrov, X., Immobilization of enzymes on porous silicas - benefits and challenges. *Chemical Society Reviews* **2013,** *42* (15), 6277-6289.

7. Gornowich, D. B. Design, fabrication, and utilization of silica inverse opal structures for flow-through catalyst supports. PhD Thesis, Michigan State University, 2013.

8. Fenton, H. J. H., LXXIII.-Oxidation of tartaric acid in presence of iron. *Journal of the Chemical Society, Transactions* **1894,** *65* (0), 899-910.

9. Woodward, J.; Wagner, M.; Lennon, K. W.; Zanin, G.; Scott, M. A., Coupling of glucose oxidase and Fenton's reaction for a simple and inexpensive assay of β-glucosidase. *Enzyme and Microbial Technology* **1985,** *7* (9), 449-453.

10. Zucca, P.; Sanjust, E., Inorganic Materials as Supports for Covalent Enzyme Immobilization: Methods and Mechanisms. *Molecules* **2014,** *19* (9), 14139-14194.

11. Gornowich, D. B., Private Communication. 2013.

12. Sassolas, A.; Blum, L. J.; Leca-Bouvier, B. D., Immobilization strategies to develop enzymatic biosensors. *Biotechnology Advances* **2012,** *30* (3), 489-511.

13. Talbert, J. N.; Goddard, J. M., Enzymes on material surfaces. *Colloids and Surfaces B: Biointerfaces* **2012,** *93*, 8-19.

14. Brady, D.; Jordaan, J., Advances in enzyme immobilisation. *Biotechnology Letters* **2009,** *31* (11), 1639.

15. Betancor, L.; López-Gallego, F.; Hidalgo, A.; Alonso-Morales, N.; Mateo, G. D.-O. C.; Fernández-Lafuente, R.; Guisán, J. M., Different mechanisms of protein immobilization on glutaraldehyde activated supports: Effect of support activation and immobilization conditions. *Enzyme and Microbial Technology* **2006,** *39* (4), 877-882.

16. López-Gallego, F.; Betancor, L.; Mateo, C.; Hidalgo, A.; Alonso-Morales, N.; Dellamora-Ortiz, G.; Guisán, J. M.; Fernández-Lafuente, R., Enzyme stabilization by glutaraldehyde crosslinking of adsorbed proteins on aminated supports. *Journal of Biotechnology* **2005,** *119* (1), 70-75.

17. Bisswanger, H., Enzyme assays. *Perspectives in Science* **2014,** *1* (1), 41-55.

18. Sadana, A., Enzyme deactivation. *Biotechnology Advances* **1988,** *6* (3), 349-IN2.

19. Krishnaswamy, S.; Kittrell, J. R., Deactivation studies of immobilized glucose oxidase. *Biotechnology and Bioengineering* **1978,** *20* (6), 821-835.

20. Malikkides, C. O.; Weiland, R. H., On the mechanism of immobilized glucose oxidase deactivation by hydrogen peroxide. *Biotechnology and Bioengineering* **1982,** *24* (11), 2419-2439.

21. Boudart, M., Turnover Rates in Heterogeneous Catalysis. *Chemical Reviews* **1995,** *95* (3), 661-666.

22. Bankar, S. B.; Bule, M. V.; Singhal, R. S.; Ananthanarayan, L., Glucose oxidase — An overview. *Biotechnology Advances* **2009,** *27* (4), 489-501.

CHAPTER 4: Demonstration of Flow-Through Catalytic Reactions using a Porous Silica Support: Reduction of p-Coumaric Acid

4.1 Abstract

We report on the synthesis and characterization of biotinylated Pd nanoparticles (NPs) and their catalytic activity for hydrogenation of p-coumaric acid. The Pd NPs were synthesized using biotin to function as a stabilizing agent and as a binder to silica surfaces treated with aminopropyltriethoxysilane (APTES). The morphology and size distribution of the Pd NPs was characterized by TEM and crystalline structure was confirmed by x-ray diffraction. Thermal stability and organic content of the Pd NPs was characterized by thermogravimetric analysis (TGA). Immobilization of the Pd NPs on a silica support was performed using the EDC coupling reaction. Continuous flow reactions were performed using aqueous and isopropanol solutions of p-coumaric acid to assess the catalytic activity and stability of the support-bound Pd NPs. At room temperature and in the absence of H_2(g), the aqueous solution afforded quantitative substrate conversion while the isopropanol solution led to deactivation of the catalyst.

4.2 Introduction

The current consumption of energy relies primarily on fossil fuels. An important goal of energy research is to devise means of energy generation based on non-carbonaceous sources. Some applications will, however, for the foreseeable future require the use of carbon-based fuels, and the sources of that fuel can, in principle, be changed to utilize renewable resources.[1] Biomass has the potential to become a significant part of the solution. The key to realizing this potential is the development of functional and comprehensive biomass refineries (biorefineries) equipped to perform the step-wise transformations required to convert a diverse range of feedstock materials classified as biomass to hydrocarbons. The paradigm shift from petroleum-derived hydrocarbons to bio-feedstock based hydrocarbons will create opportunities for the chemical processing industry.[2] The ideal biorefinery processing of biomass-derived feedstocks will enable the efficient conversion of carbohydrates and partially oxidized hydrocarbons to hydrocarbons under mild conditions, and in conformance with the principles of green chemistry.[3] Catalysis is considered a key component of the Twelve Principles of Green Chemistry.[4] Indeed, heterogeneous catalysis satisfies many of the goals of Green Chemistry by facilitating easy separation and product recovery.[5] In a bio-refinery, catalytic hydrogenation processes are among the most valuable elementary transformations. However, due to the limited solubility of hydrogen in environmentally friendly solvent systems, conventional hydrogenation processes require an excessive amount of hydrogen to be introduced at high pressure and temperature to achieve the desired conversion(s). An ideal catalyst would offer lowered reaction energy, increased selectivity, and quantitative conversion of the reactants to products.

There are, of course, a variety of ways to implement heterogeneous catalytic reactions. Among the goals of reaction design are easy recovery of the catalyst following the reaction, and facile clean-up. For many catalytic reactions, the catalyst of choice is a metal (*e.g.* Pt, Pd, Ru, Au or mixed metal NPs) and there is benefit from an atom-economy standpoint for using the catalyst in the form of nanoparticles, owing to the high surface area to volume ratio for this structural motif.[6,7,8] In this work we demonstrate a continuous-flow reactor to perform a selective catalytic hydrogenation reaction at room temperature and atmospheric pressure. Pd nanoparticles, used as the catalyst in this work, were synthesized using biotin as a stabilizing agent and crosslinker between the nanoparticles and a porous oxide catalyst support. The use of robust porous oxide supports will ultimately provide the ability to perform catalytic conversion processes in a pre-determined and controllable order by arranging different catalysts in a specific sequence. This approach to the conversion of bio-feedstock materials into desired product(s) through a sequence of elementary transformations, significantly expands the range of products attainable from a single series of supported catalysts.

4.3 Experimental Methods

Chemicals. Biotin (≥99%, TLC, lyophilized powder Sigma-Aldrich), palladium acetate (≥99.9%, trace metal basis), methanol (HPLC grade, Sigma-Aldrich), (3-amninopropyl) triethoxysilane (APTES, ≥99%, Sigma-Aldrich), N-(3-Dimethylaminopropyl)-N′-ethylcarbodiimide hydrochloride (EDC, commercial grade, powder, Sigma-Aldrich), N-hydroxysuccinimide (NHS, 98%, Sigma-Aldrich), p-coumaric acid (≥98%, HPLC, Sigma-Aldrich), isopropanol (anhydrous, Sigma-Aldrich), and hydrogen (Airgas), were used as received, without further purification. 3-(4-Hydroxyphenyl)propionic acid (hydro-p-coumaric acid, 98%, Sigma-Aldrich) were used as standards for LC/MS analysis. Propyl-4-hydroxybenzoate (≥99%, Sigma-Aldrich) was used as the internal standard. Sintered glass filter discs (25 mm diameter, 3.5 mm thickness, grade E, Ace Glass) were used as catalyst supports.

Solutions. Potassium phosphate monobasic (ACS reagent, ≥99%, Sigma-Aldrich), sodium phosphate dibasic heptahydrate (ACS reagent,98%-102%, Sigma-Aldrich), sodium chloride (ACS reagent, ≥99%, Fisher Chemical), potassium chloride ACS reagent, ≥99%, Fisher Chemical) sodium hydroxide, hydrochloride acid (12 M) and water (Milli Q) were used to make phosphate buffer (PBS buffer, pH 7). Piranha solution was made of concentrated sulfuric acid (18 M) and hydrogen peroxide (30%) with a volume ratio of 3:1 *(Caution! Strong Oxidizer!)*. Aqua regia solution was made of concentrated hydrochloride acid and nitric acid with volume ratio of 3:1 *(Caution! Strong Oxidizer!)*.

Palladium nanoparticle synthesis. Palladium acetate (0.06g) and biotin (0.2g) were dissolved in methanol (160 mL) in a 500 mL two-neck round bottom flask. The fully dissolved solution was stirred and bubbled with N_2(g) for 2 hours. The solution was then heated to 70 °C for 24 hours under flowing N_2(g).[9] Methanol was removed under vacuum using a rotary evaporator and acetone was added to effect precipitation of the NPs. The resulting precipitate was centrifuged at 4500 rpm for 8 minutes, then washed twice with acetone. Biotinylated Pd NPs were re-dispersed in PBS buffer (pH 7) for subsequent storage and use.

Palladium nanoparticle immobilization on glass frit catalyst supports. Sintered glass filter discs (glass frits) were cleaned with piranha solution and washed with water and ethanol before further use. Hydrochloric acid solution (0.5M) was used to remove hydrogen peroxide residue in glass frit pores (12 h at 60 °C). The resulting hydroxyl-rich surface was silanized using APTES in methanol (7% v/v) for 3 hours, washed with flowing isopropanol to remove unreacted reagent from the pores of the glass frit, and cured at 60 °C. Finally, biotinylated-Pd NPs activated by EDC and NHS (PBS buffer, pH 7) were flowed through the APTES-modified frit to crosslink the carboxylate group of biotin and the amino functionalities on the glass frit pore surfaces. The amount of Pd NP solution and cross-linking reagents can be adjusted to maintain NP solubility in solution[10] for the purpose of maintaining a uniform NP distribution on the support. An in-house-made Teflon® flow cell was used to hold glass frits in place for flow-through experiments.[11]

Flow-through experiment. p-Coumaric acid solutions (2 mM) were made with isopropanol and PBS buffer (pH 7), respectively, and saturated with hydrogen gas using a gas dispersion tube (fine porosity, Ace Glass). A glass frit containing immobilized Pd NPs was placed in the Teflon® flow cell and hydrogen gas was used to fill the chamber and glass pores. Feedstock solutions were flowed through glass frits using a syringe pump (NE-1000 programmable single syringe pump, New Era Pump System Inc.) at 15 μL/min. The eluent was collected at 30 minute intervals for a period of 2.5 hours. Reproducibility was evaluated by running each experiment three times. For evaluation of the reusability of the Pd NPs, the flow-through reaction was operated for a period of three days, sampling at intervals.

Sample analysis. p-Coumaric acid in IPA and PBS buffer and eluent aliquots were analyzed by UPLC-MS (Waters, Acquity BCH C_{18} column).

Transmission Electron Microscopy (TEM). TEM images were obtained using an ultra-high-resolution JEOL 2200FS transmission electron microscope located in the Center for Advanced Microscopy at Michigan State University (MSU). Acceleration voltage was 200 kV for all measurements.

Thermogravimetric Analysis (TGA). Nanoparticle samples used for TGA measurements were washed with acetone and dried prior to measurement. TGA measurements were performed using a Perkin Elmer TGA 7 instrument with a thermal ramp rate of 15 °C/min from 30 °C to 120°C, under dry nitrogen. Samples were maintained at 120 °C for 30 min. to remove moisture, and then ramped up to 800 °C at a rate of 15 °C/min.

X-ray Powder Diffraction (XRD). XRD data were collected on a Bruker D8 Advance X-ray Diffractometer with DAVINCI Design. Pd NPs were washed with acetone, dried and the agglomerates were ground into fine powder. Angle scans started at 30° and ran to 90° in steps of 0.02049°. The Pd standard (reference position: 00-001-1201) was used for the analysis of face centered cubic Pd.

Inductively coupled plasma optical emission spectrometry (ICP-OES). ICP measurements (λ_{em} = 248.9 nm) were used to determine the amount of Pd immobilized on the silica supports. Used glass frits containing immobilized Pd NPs were dissolved in 12 mL Aqua Regia solution overnight and diluted to 500 mL with MilliQ water. Pd standard solution for ICP measurements (1000 ppm, Inorganic Ventures) was used to create calibration curves.

Ultraviolet-visible spectroscopy (UV-Vis). UV-Vis absorbance data were collected using an ATI UNICAM UV2 UV/Vis spectrometer. For these measurements, the wavelength was scanned from 200nm to 400nm at a scan rate 600 nm/min. Resolution for all measurements was 1 nm.

4.4 Results and Discussion

4.4.1 Nanoparticle Characterization.

The synthesis of Pd NPs stabilized by biotin has been reported previously by the Ofoli Group.[9] Biotin functions not only as the stabilizing ligand for Pd NPs but also as a crosslinker between the porous silica surface and the Pd NPs. The thioether functionalities on biotin bind strongly to metals such as Pd and serve as a stabilizer to control the size and uniformity of the nanoparticles. In the synthesis procedure, palladium acetate and biotin were dissolved in methanol and refluxed at 70 °C for 24 hours. The

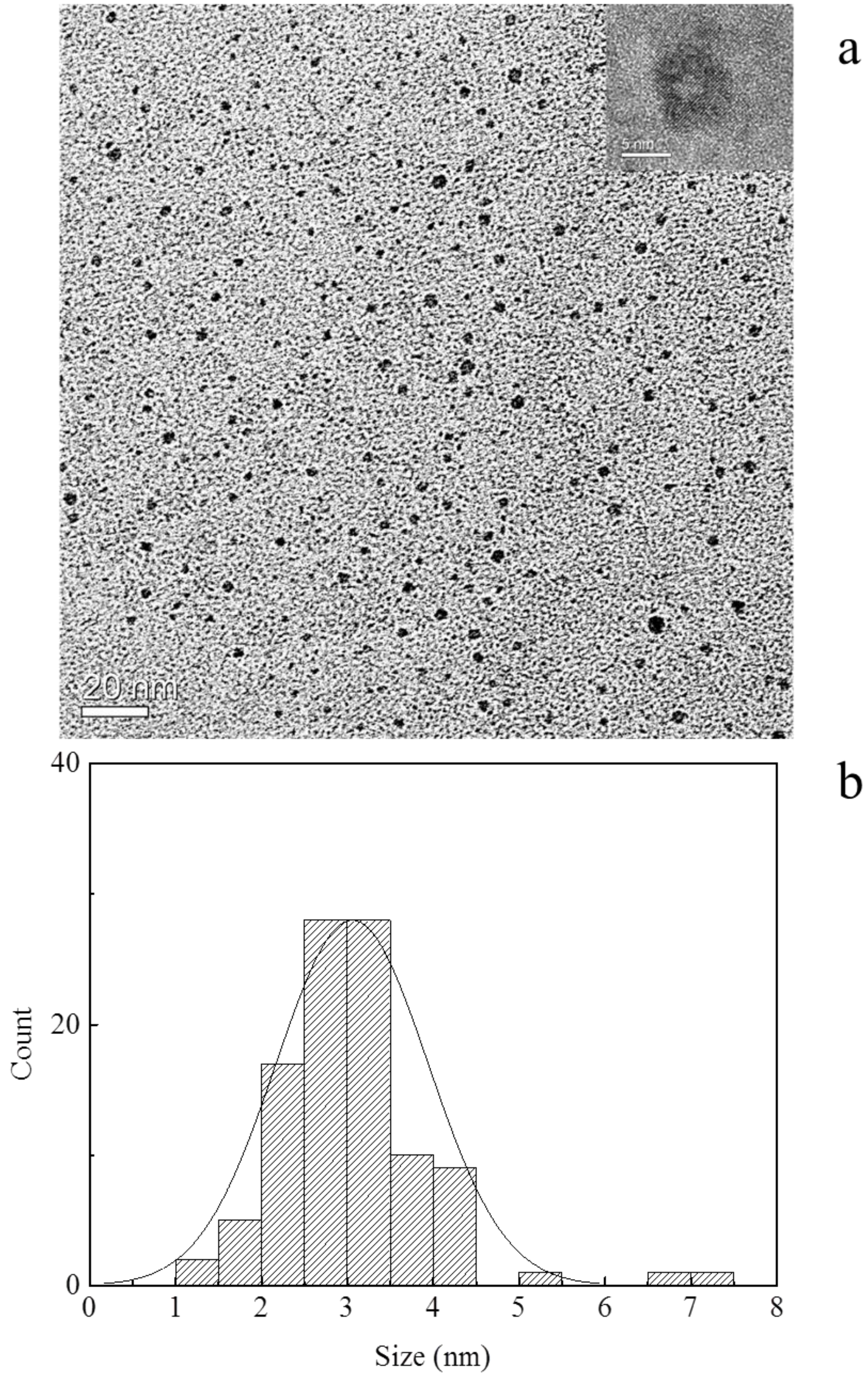

Figure 4.1 a) TEM images of biotinylated Pd NPs show the morphology of nanoparticles and the lattice of a single particle (inset). b) A histogram of the average size and size distribution of the Pd NPs shown in (a).

color changed from yellow to dark brown during the course of the reaction, indicating the formation of Pd NPs.

TEM images (Fig. 4.1a) show the as-synthesized Pd NPs with an average size of 3.1±0.9 nm and the histogram (Fig. 4.1b) shows the size distribution from 1.5 nm to 4 nm, determined by the measurement of more than 100 NPs. A few Pd NPs were found to be greater than 5 nm diameter. The NPs with diameters less than 5 nm diameter were used for catalysis experiments due to their high surface area-to-volume ratio. As-prepared Pd NPs were used as heterogeneous hydrogenation catalysts for phenolic compounds.

XRD was used to confirm the crystal structure of biotinylated Pd NPs. Fig. 4.2 presents X-ray diffraction results with 2θ peaks at 39.5°, 67.5°, 81.0° and a peak shoulder at 46°. A Pd standard pattern (reference position: 00-001-1201) is also shown for comparison. These peaks correspond to the (111), (220) and (311) planes of a fcc lattice, indicating the as-prepared nanoparticles have face-centered cubic structure.[12] The peak shoulder at 46° corresponds to the (200) plane, which is poorly resolved from the (111) peak. Peak broadening was observed due to the nanocrystalline nature of the NPs. Based on the Scherrer Equation,[13] the peak width is inversely proportional to crystal size. In addition, the diffraction angles are shifted slightly toward lower values compared to the JCPDS standards for bulk Pd (40.4°, 46.7°, 68.4°, 82.3°). We interpret this to mean the Pd-Pd interatomic distance expands in our nanocrystalline structures due to the presence of an organic ligand associated with the surface Pd atoms, and the relatively high fraction of Pd surface atoms in the NP. Our findings are reminiscent of those reported for polymer-capped Pd nanoparticles.[12]

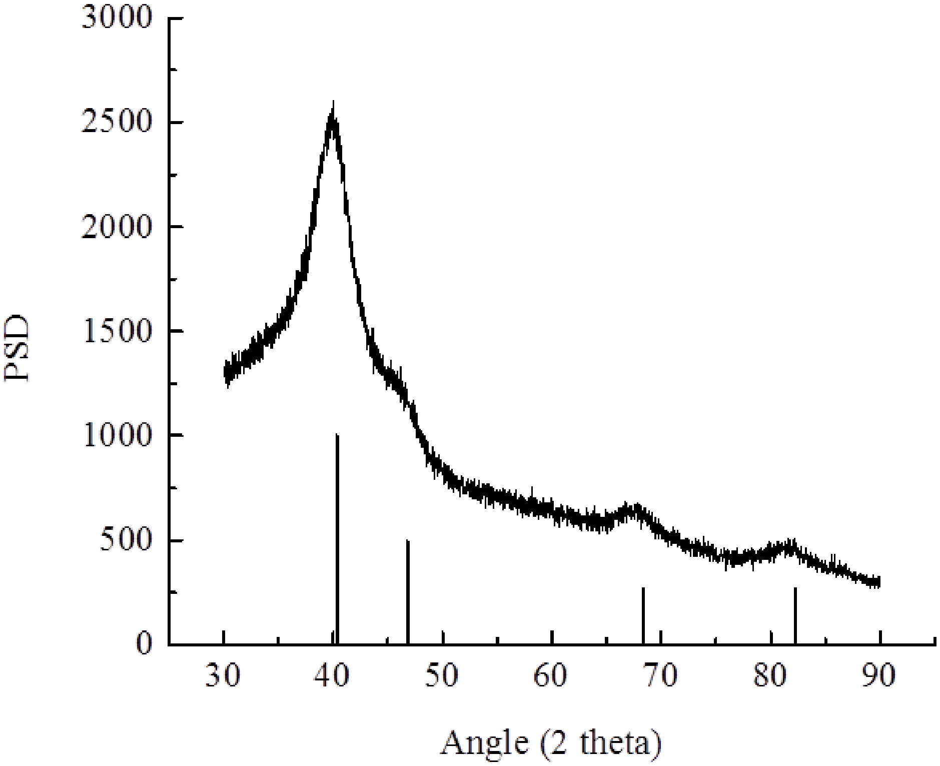

Figure 4.2 X-ray diffraction data of biotinylated Pd NPs. JCSPD standard of Pd black are shown for comparison.

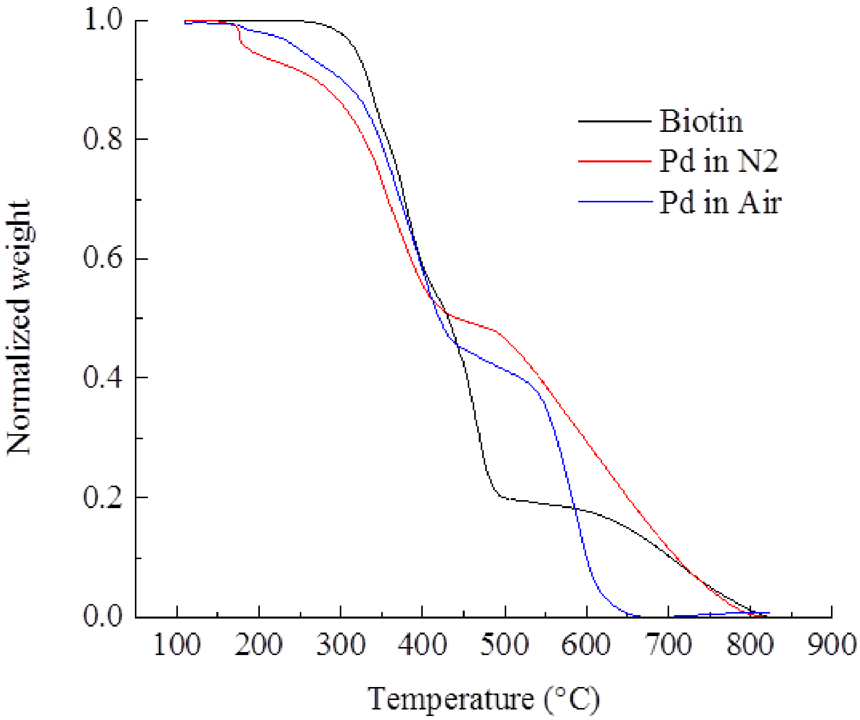

Figure 4.3 Thermogravimetric (TGA) data shows the normalized weight loss of biotin (black), biotinylated Pd NPs in nitrogen (red) and biotinylated Pd NPs in air (blue).

TGA measurements were performed to understand the thermal stability of biotinylated palladium nanoparticles, thermal degradation behavior and content of the stabilizing agent on the surface of the Pd NPs.[14] Initial masses of biotinylated Pd NPs were corrected for sample weight after holding for 30 min at 120 °C to remove moisture. The mass loss from 120 °C to 800 °C can provide an estimate of the mass of biotin bound to the Pd NPs. The decomposition temperature of biotin is 300 °C, determined as the onset of the mass loss for its thermogram (Fig. 4.3). When comparing the weight loss of biotinylated Pd NPs to the thermal decomposition of biotin, the decomposition temperatures are in agreement. However, the weight loss curves of biotinylated nanoparticles in N_2 exhibit a two-step decomposition at 325 °C and 525 °C. The as-prepared NPs show excellent thermal stability at high temperature, which enables wide usability of as-synthesized biotinylated Pd NPs.

In an attempt to derive quantitative information from the TGA data, measurements were made in triplicate (three samples). From these data we find the average residual mass to be 37.5% ± 1.8% of the initial mass (after heating to 120 °C for 30 min), indicating that 62.5% mass of the biotinylated Pd NPs is associated with the organic stabilizing agent. The calculated nanoparticle molar ratio of biotin (lost mass) to Pd NPs (residual mass) is much less than the input reactant molar ratio (3:1), indicating that a large fraction of the biotin used in the reaction does not reside on the surface of the Pd NPs. We cannot determine whether this result corresponds to incomplete coverage of the Pd NPs because we do not have quantitative information on the fraction of Pd reactant that was incorporated into Pd NPs.

4.4.2 Surface immobilization on a porous silica surface

Water-soluble carbodiimides, such as 1-ethyl-3-(3-dimethylaminopropyl)carbodiimide) (EDC), are some of the most widely used cross-linking reagents. EDC reacts with the carboxylic acid functionality of biotin to form an unstable o-acylisourea intermediate in aqueous solution. Water–soluble sulfo-NHS is used in EDC coupling protocols to improve the efficiency of forming dry-stable intermediates. The sulfo-NHS ester formed by EDC and sulfo-NHS coupling is hydrophilic and reactive groups that couple rapidly with amines on target molecules are considerably more stable in aqueous solution than the o-acylisourea intermediate, while allowing efficient coupling to primary amines on the silica surface. The porous silica surface was hydroxyl-rich after cleaning with piranha solution and aminosilanization with APTES. An amide bond is formed between biotin attached to the nanoparticles and the aminosilanized glass frit surface, as shown in Fig.4.4. EDC and sulfo-NHS coupling can also be performed in a single reaction vessel to bind the biotinylated Pd NPs.[15] The reaction with EDC and sulfo-NHS is most efficient in the pH of 4.5 to 7.2.[10] Reaction of sulfo-NHS-activated species with primary amines is most efficient in the pH range of 7 to 8 in phosphate buffer.[10] For optimum results in a single-vessel reaction, phosphate buffer at pH 7 is used for both activation of the biotinylated Pd NPs and (flowing) immobilization of NPs on the porous silica frit.

The effectiveness of nanoparticle immobilization on surfaces has been assessed with X-ray photoelectron spectroscopy (XPS) and FTIR by Lin.[16] The biotinylated Pd NPs were immobilized on glass surfaces by the formation of covalent amide bonds between activated biotin and the amine functionalities on the silica surface. In the work reported

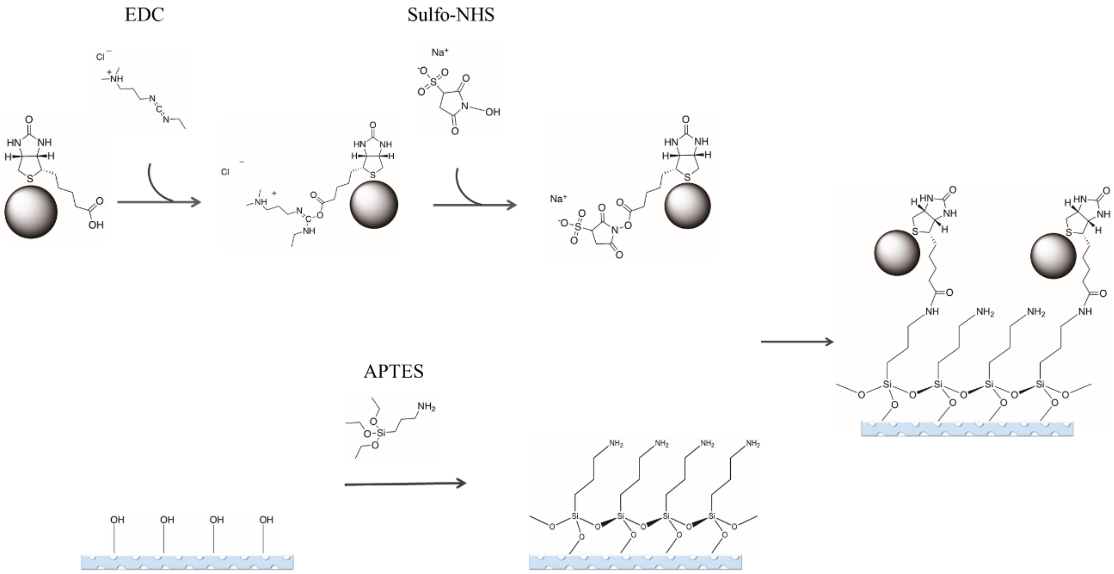

Figure 4.4 Surface immobilization of biotinylated palladium nanoparticles on a porous glass frit support.

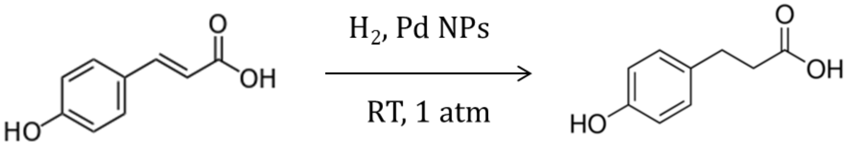

Figure 4.5 Hydrogenation reaction of p-coumaric acid to hydro-p-coumaric acid with PdNP catalyst at room temperature and one atmosphere pressure.

here, dark brown nanoparticles can be seen against the white porous glass frit, indicating nanoparticles are either immobilized on the silica surface or are trapped in pores. A uniform surface color indicates that Pd NPs are dispersed evenly, minimizing the possibility of incomplete reaction due to passage of reactant solution through catalyst-poor regions. Treatment with aqua regia was used to digest the Pd NPs,[17] and inductively coupled plasma atomic emission spectroscopy (ICP-AES) was used to quantify the amount of Pd immobilized on the glass frit. The average mass of Pd on the glass frit is 0.30 ± 0.06 mg. For a frit (of the same dimension) that produced complete conversion of the coumaric acid reactant, the Pd content of the frit was found to be only 0.09 mg. It thus appears that 0.3 mg of Pd NPs is not required to achieve full conversion. Due to the high surface area-to-volume ratio and known catalytic activity of the surface atoms, Pd NPs are more efficient than bulk catalyst. A detailed study of the relationship between Pd NP loading and catalytic activity is beyond the scope of this work and will require further study. For the purposes of this work, the Pd NP catalyst loaded onto a porous glass frit is an effective catalyst that is capable of full reactant conversion.

4.4.3 Hydrogenation of p-coumaric acid

The biotinylated Pd NPs were evaluated for catalytic activity in the heterogeneous hydrogenation reaction with p-coumaric acid. A flow reactor made in-house was used to hold the catalyst support in place and reactions were performed under ambient conditions. p-Coumaric acid was used as the substrate and the hydrogenation reaction is shown in Fig. 4.5. The conversion of p-coumaric acid was used as a measure of the efficiency of the catalytic reaction. Percent conversion was defined as

$$conversion\ (\%) = \frac{moles\ of\ substrate\ consumed}{moles\ of\ substrate\ supplied} \times 100$$

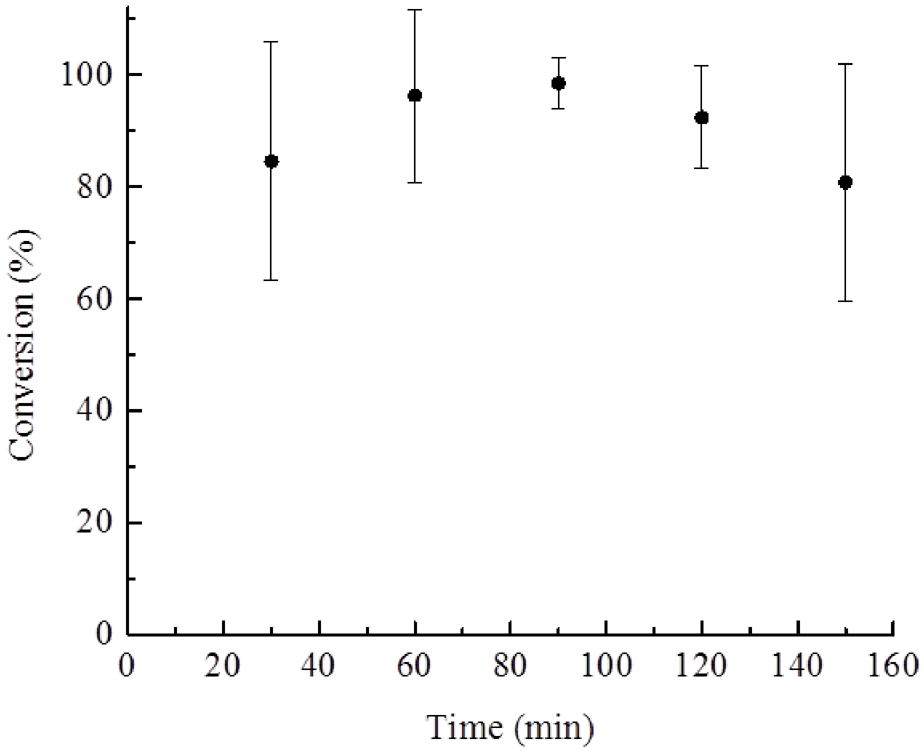

Figure 4.6 Conversion of p-coumaric acid to p-hydrocoumaric acid in phosphate buffer solution as a function of reaction time.

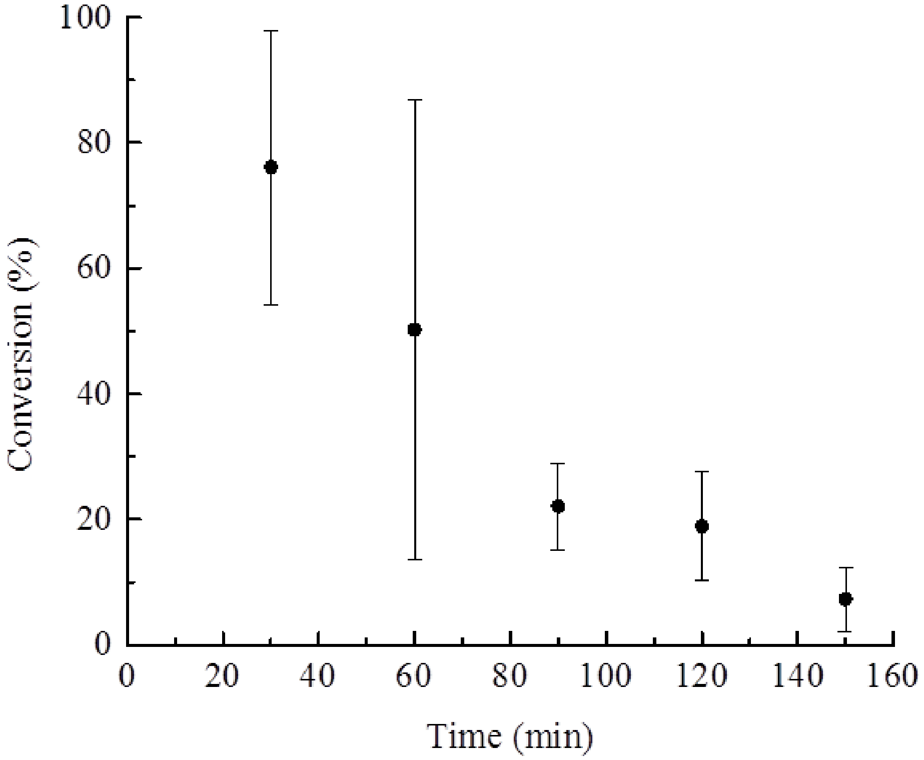

Figure 4.7 Conversion of p-coumaric acid to p-hydrocoumaric acid in isopropanol as a function of reaction time.

H_2(g) was flowed through the glass frit in the reactor to fill the frit pores and reactor chamber, to achieve the maximum possible liquid-catalyst-gas interaction. The tortuous paths of the pores in the glass frit can be considered three-dimensional "microchannels" to improve the efficiency of gas-liquid-solid phase interactions due to the large interfacial areas and the short path(s) required for molecular diffusion.[18] Substrate solutions were saturated with H_2(g) to increase the amount of hydrogen present in the reacting solution and to protect the Pd NP catalyst from poisoning by oxidation. As a control, no hydro-p-coumaric acid product was detected in the product aliquots when flowing reactant through the glass frit without immobilized-Pd NPs, demonstrating that no hydrogenation reaction occurred in the absence of catalyst. Phosphate buffer (pH = 7) and isopropanol were used as the solvent systems for the reaction to determine which provided higher yield. The fractional conversions of the p-coumaric acid hydrogenation reaction in phosphate buffer and isopropanol at a flow rate of 15μL/min under ambient conditions are shown as a function of reaction run time in Figs. 4.6 and 4.7, respectively. At all stages of the reaction, the product was exclusively hydro-p-coumaric acid for both aqueous and organic solvent; no reaction intermediates or side products were observed. In PBS buffer, the conversion of p-coumaric acid started at *ca*. 85% for the first 30 min and then remained stable at over 90% after 90 minutes of run time. Conversion and reproducibility were observed to decrease slightly after 160 min run time.

In comparison to the reaction in aqueous solvent, the conversion of p-coumaric acid in isopropanol is shown in Fig. 4.7. The reaction starts at *ca*. 80% conversion for the first 30 min, similar to the performance in phosphate buffer, but in contrast to the buffer solution system, the reaction experiences a 70% decrease in conversion over the next 100 min. For the reaction aliquot acquired at 60 min run time, there is poor reproducibility over three runs, and this result is reflective of the system transitioning from high efficiency to low efficiency during this time window. Variability in the efficiency of the catalytic reaction may be related to the chemical state (*i.e.* poisoning) of the catalytic NPs.

For the catalytic hydrogenation of p-coumaric acid in aqueous medium, the yield remains above 80% conversion. In contrast, the catalytic conversion efficiency drops to *ca*. 10% in isopropanol. As noted above, one possible explanation for this behavior is poisoning of the catalyst. Based on the IUPAC-NIST gas solubility database,[19] the mole fractions of oxygen and hydrogen in the aqueous solution are *ca*. 2.5×10^{-5} and 1.5×10^{-5}, respectively, under ambient conditions. The effect of ionic species in the phosphate buffer is negligible for the salt concentrations used here.[20] In isopropanol, the mole fractions of oxygen and hydrogen are 7.87×10^{-4} and 2.66×10^{-4}, respectively.[19] Although the solubility of hydrogen is around 18 times higher in isopropanol than in aqueous solution, the solubility of oxygen is 31 times higher in isopropanol. The relatively enhanced solubility of oxygen in isopropanol suggests that re-dissolution of oxygen during the reaction in preference to hydrogen is seen in the competition between reaction and oxidation at the Pd NP surface.[21,22] This conclusion is supported by a continuous flow-experiment of p-coumaric acid in phosphate buffer that is interrupted by the introduction of air (via syringe) during the course of the run. While the conversion efficiency would recover, there was an initial significant reduction in conversion efficiency. It has been reported that Pd/silica is deactivated over time for hydrogenation and hydrodeoxygenation reactions of phenolic compounds,[23] consistent with our findings. In that work, the loss of active sites rendered any subsequent reactant adsorption non-reactive, and that was considered to be a primary route of catalyst deactivation. It was also reported that heterogeneous catalytic gas phase reactions were characterized by inhibition or poisoning by the presence of a small concentration of oxygen.[24]

4.4.4 Assessment of Pd NP catalytic stability

Catalyst stability was evaluated under continuous flow of p-coumaric acid in phosphate buffer through a glass frit containing immobilized Pd NPs over a 58 hour reaction run time. Fig. 4.8 shows the conversion of substrate as a function of reaction time. Reactant conversion started at 95% for the first 50 min aliquot and maintained essentially quantitative conversion for the next 250 min, then the conversion dropped to zero by 1700 min run time. Complete deactivation of Pd NPs occurs by 28 hours of run time. As a hydrogenation catalyst, the biotinylated Pd NPs demonstrated the ability to react stably for more than one day without an external source of hydrogen at room temperature and at atmosphere pressure.

A three dimensional array of UV-visible spectra is shown in Fig. 4.9. These data are the absorbance data of collected aliquots as a function of reaction time. The collection time range was 3500 min. Spectra from 220 nm to 300 nm were displayed along the x-axis and time increases in the two-dimensional plane of the absorbance

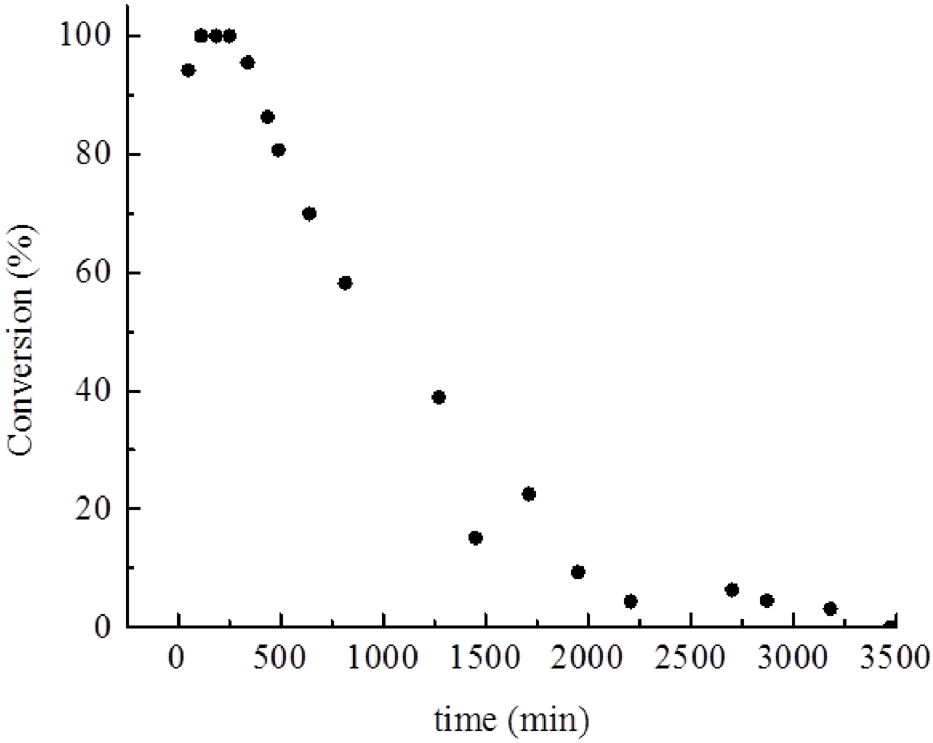

Figure 4.8 Long-term reaction conversion efficiency.

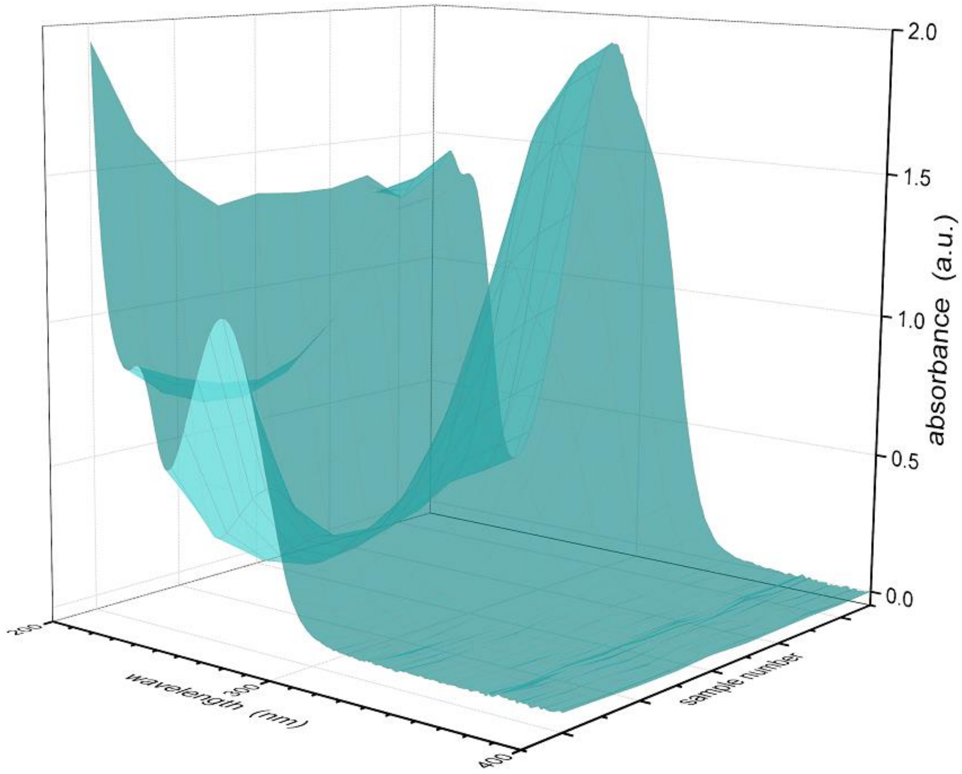

Figure 4.9 Three-dimensional UV-visible spectra of collected aliquots as a function of reaction time. The total time range is 3500 min.

spectra. The absorbance maxima of p-coumaric acid and hydro-p-coumaric acid are 283 nm and 260 nm, respectively, and spectra of the reactant and product correspond to the last and first sample aliquots reported in the time sequence. These data indicate that the reactant was converted quantitatively to hydro-p-coumaric acid at the beginning of the flowing reaction and the catalyst was fully deactivated by the end of the run. For the aliquots collected during the 28 hour run, it is apparent from the absorbance spectra that the peak positions undergo a shift from 260 nm to 283 nm with the 260 nm band decreasing to a minimum value, and a corresponding rise in intensity of the 283 nm band. The spectral minimum is seen for the 340 min aliquot, which undergoes 95% conversion to hydro-p-coumaric acid. Then the spectra shift to the red and increase in absorbance, indicating the passage of p-coumaric acid through the catalyst-loaded frit unreacted.

4.5 Conclusions

We have developed a robust flow-through catalyst support with biotinylated Pd NPs immobilized on porous silica and have demonstrated its utility through a heterogeneous hydrogenation reaction. The as-synthesized biotinylated Pd NPs were characterized as having face-centered cubic crystal structure with an average size of 3 nm and the organic stabilizing capping agent making up 67 wt% of the NP mass. The Pd NPs were immobilized on the aminosilanized silica surface using biotin, with the thioether moiety of biotin binding to the Pd NP surface and the carboxylic functionality forming an amide bond to the aminosilane. We have demonstrated the catalytic production of hydro-p-coumaric acid from p-coumaric acid and have characterized this reaction in aqueous and organic solvent systems. In aqueous buffer, the reaction yielded >95% conversion with good reproducibility in a 340 min reaction time under ambient conditions. In isopropanol solvent, however, the conversion of p-coumaric acid decreased to *ca*. 25% over the course of a 150 min reaction time. This decrease in conversion can be understood in the context of catalyst deactivation, likely due to NP surface contamination. The stability of the Pd NP catalyst in aqueous solvent was evaluated as a function of flow reaction time, with the Pd NPs becoming fully deactivated during 28h of run time in the absence of an external H_2 source.

The next steps in this work will be to gain control over the regulation and delivery of $H_2(g)$ to reaction system,[25] to evaluate the versatility of this approach to catalytic flow-through reactions, and to incorporate this flow-reaction system into a multi-step reactor. Of significance in this work is that we achieved hi conversion and reproducibility for a multiphase reaction, lifting the limitation of heterogeneous hydrogenation reactions that require high temperature and high pressure to operate efficiently due to the limited solubility of hydrogen in the liquid phase reactant stream.

REFERENCES

REFERENCES

1. Huber, G. W.; Dumesic, J. A., An overview of aqueous-phase catalytic processes for production of hydrogen and alkanes in a biorefinery. *Catal Today* **2006,** *111* (1-2), 119-132.

2. Ragauskas, A. J.; Williams, C. K.; Davison, B. H.; Britovsek, G.; Cairney, J.; Eckert, C. A.; Frederick, W. J.; Hallett, J. P.; Leak, D. J.; Liotta, C. L.; Mielenz, J. R.; Murphy, R.; Templer, R.; Tschaplinski, T., The path forward for biofuels and biomaterials. *Science* **2006,** *311* (5760), 484-489.

3. Simonetti, D. A.; Dumesic, J. A., Catalytic Production of Liquid Fuels from Biomass-Derived Oxygenated Hydrocarbons: Catalytic Coupling at Multiple Length Scales. *Catal Rev* **2009,** *51* (3), 441-484.

4. Anastas, P. T.; Warner, J. C., *Green Chemistry: Theory and Practice*. Oxford University Press: New York; Oxford [England];, 1998.

5. Irfan, M.; Glasnov, T. N.; Kappe, C. O., Heterogeneous Catalytic Hydrogenation Reactions in Continuous-Flow Reactors. *ChemSusChem* **2011,** *4* (3), 300-316.

6. Raimondi, F.; Scherer, G. G.; Kotz, R.; Wokaun, A., Nanoparticles in energy technology: Examples from electrochemistry and catalysis. *Angew Chem Int Edit* **2005,** *44* (15), 2190-2209.

7. Bhattacharjee, S.; Dotzauer, D. M.; Bruening, M. L., Selectivity as a Function of Nanoparticle Size in the Catalytic Hydrogenation of Unsaturated Alcohols. *J Am Chem Soc* **2009,** *131* (10), 3601-3610.

8. Song, H.; Rioux, R. M.; Hoefelmeyer, J. D.; Komor, R.; Niesz, K.; Grass, M.; Yang, P. D.; Somorjai, G. A., Hydrothermal growth of mesoporous SBA-15 silica in the presence of PVP-stabilized Pt nanoparticles: Synthesis, characterization, and catalytic properties. *J Am Chem Soc* **2006,** *128* (9), 3027-3037.

9. Lin, R.; Freemantle, R. G.; Kelly, N. M.; Fielitz, T. R.; Obare, S. O.; Ofoli, R. Y., In situ immobilization of palladium nanoparticles in microfluidic reactors and assessment of their catalytic activity. *Nanotechnology* **2010,** *21* (32).

10. Hermanson, G. T., Chapter 4 - Zero-Length Crosslinkers. In *Bioconjugate Techniques (Third edition)*, Academic Press: Boston, 2013; pp 259-273.

11. Gornowich, D. B.; Blanchard, G. J., Enhancement of Enzyme Activity by Confinement in an Inverse Opal Structure. *The Journal of Physical Chemistry C* **2012,** *116* (22), 12165-12171.

12. Teranishi, T.; Miyake, M., Size control of palladium nanoparticles and their crystal structures. *Chem Mater* **1998,** *10* (2), 594-600.

13. Patterson, A. L., The Scherrer formula for x-ray particle size determination. *Phys Rev* **1939,** *56* (10), 978-982.

14. Mahdavi, H.; Sahraei, R., Synthesis and Application of Hyperbranched Polyester-Grafted Polyethylene (HBPE-g-PE) Containing Palladium Nanoparticles as Efficient Nanocatalyst. *Catalysis Letters* **2016,** *146* (5), 977-990.

15. Bartczak, D.; Kanaras, A. G., Preparation of Peptide-Functionalized Gold Nanoparticles Using One Pot EDC/Sulfo-NHS Coupling. *Langmuir* **2011,** *27* (16), 10119-10123.

16. Lin, R. Rational design of colloidal noble metallic nanocatalysts and development of a microfluidic platform for fundamental assessment of catalytic activity. Michigan State University, PhD Thesis, 2013.

17. Balcerzak, M., Sample digestion methods for the determination of traces of precious metals by spectrometric techniques. *Anal Sci* **2002,** *18* (7), 737-750.

18. Kobayashi, J.; Mori, Y.; Okamoto, K.; Akiyama, R.; Ueno, M.; Kitamori, T.; Kobayashi, S., A microfluidic device for conducting gas-liquid-solid hydrogenation reactions. *Science* **2004,** *304* (5675), 1305-1308.

19. Clever, H. L.; Battino, R.; Miyamoto, H.; Yampolski, Y.; Young, C. L., IUPAC-NIST Solubility Data Series. 103. Oxygen and Ozone in Water, Aqueous Solutions, and Organic Liquids (Supplement to Solubility Data Series Volume 7). *J Phys Chem Ref Data* **2014,** *43* (3).

20. Sato, T.; Hamada, Y.; Sumikawa, M.; Araki, S.; Yamamoto, H., Solubility of Oxygen in Organic Solvents and Calculation of the Hansen Solubility Parameters of Oxygen. *Industrial & Engineering Chemistry Research* **2014,** *53* (49), 19331-19337.

21. Moulijn, J. A.; van Diepen, A. E.; Kapteijn, F., Catalyst deactivation: is it predictable? What to do? *Appl Catal a-Gen* **2001,** *212* (1-2), 3-16.

22. Bartholomew, C. H., Mechanisms of catalyst deactivation. *Appl Catal a-Gen* **2001,** *212* (1-2), 17-60.

23. de Souza, P. M.; Rabelo-Neto, R. C.; Borges, L. E. P.; Jacobs, G.; Davis, B. H.; Resasco, D. E.; Noronha, F. B., Hydrodeoxygenation of Phenol over Pd Catalysts. Effect of Support on Reaction Mechanism and Catalyst Deactivation. *ACS Catalysis* **2017,** *7* (3), 2058-2073.

24. Almquist, J. A.; Black, C. A., The poisoning action of oxygen on iron catalysts for ammonia synthesis. *J Am Chem Soc* **1926,** *48*, 2814-2820.

25. Zhang, X.; Blanchard, G. J., Flow-Through Catalytic Reaction of Cinnamaldehyde using a Porous Silica Support. *Phys. Chem. Chem. Phys.* **2017,** *in review (companion manuscript)*.

CHAPTER 5: Flow-Through Catalytic Reaction of Cinnamaldehyde using a Porous Silica Support

4.6 Abstract

The focus of this work is to utilize immobilized Pd NP catalyst to perform heterogeneous hydrogenation of cinnamaldehyde, an α,β-unsaturated compound. We presented the fabrication and characterization of biotinylated Pd NPs and their deposition onto a porous silica support in the companion manuscript and report in this work on the use of the supported Pd NP system as a catalyst for the chemoselective hydrogenation of cinnamaldehyde in aqueous buffer and isopropanol. Under ambient conditions, full conversion of cinnamaldehyde to hydrocinnamyl alcohol can be achieved in aqueous buffer solution, while performing the reaction in isopropanol results in the deactivation of the catalyst over a 150 min reaction time. To overcome this limitation for isopropanol as a solvent, we designed a flow system in which hydrogen gas can be periodically introduced into the reaction vessel and support. The flow-through system allows the use of Pd NP catalyst in isopropanol.

4.7 Introduction

The production of fossil fuels has environmental and economic consequences, and some of these may be ameliorated by the use of hydrocarbons derived from waste biomass. Central to the use of biomass for the generation of hydrocarbons is the ability to perform efficient heterogeneous hydrogenation reactions. Catalysis is essential to the realization of this goal. Any refinery-like process that utilizes biomass as feedstock has two main requirements; the catalyst systems used must be efficient and highly selective, and it would be preferable if these reactions were to proceed under ambient conditions. We have chosen to study the chemoselective hydrogenation of aromatic unsaturated aldehydes because of the potential utility of the products and the utility of this type of reaction. Cinnamaldehyde is considered to be a model substrate for the reduction of aromatic α,β-unsaturated aldehydes.[1] Cinnamaldehyde can be hydrogenated selectively to hydrocinnamaldehyde, cinnamyl alcohol, hydrocinnamyl alcohol, and propyl benzene.[2] Among the numerous reduction products, hydrocinnamaldehyde and cinnamyl alcohol, the products considered here, are important for the fine chemicals, flavors, fragrance and pharmaceuticals industries.[3-4]

For heterogeneous catalytic hydrogenation of cinnamaldehyde, supported Pd,[5] Pt,[6] and Ru[7] nanoparticle (NP) catalysts have been reported to be efficient catalysts, in part because of their high surface area-to-volume ratio. Under mild conditions, Pd is the most active catalyst for aromatic aldehyde reduction.[8] Pd NPs have been confined in multiple porous catalyst supports, such as carbon nanotubes,[5] zeolites,[9] and sol gel[10] matrices. The binding of catalytic NPs in porous materials is advantageous in that it combines the high surface area-to-volume ratio of NPs with the comparatively high accessibility of the NP to reactant streams and the minimization of aggregation phenomena, allowing a relatively high fraction of the NPs to be exposed to reactive species.[11] In this work, we used commercially available porous glass frits as NP catalyst supports because of their wide availability and favorable physical and chemical properties. The Pd NPs synthesized in our lab were in the 2 nm to 5 nm diameter range and were immobilized on the glass frit as described in the companion paper.[12] We find that cinnamaldehyde, like coumaric acid, undergoes lower efficiency conversion to hydrogenation products in isopropanol than in aqueous buffer solution with Pd NP catalyst under flow-through reaction conditions.

However, in this work, hydrogen was introduced to the reaction at regular intervals to mitigate the conditions that lead to the low conversion efficiency seen in isopropanol solvent.

4.8 Experimental Methods

Chemicals. Biotin (≥99%, TLC, lyophilized powder, Sigma-Aldrich), palladium acetate (≥99.9%, trace metal basis, Sigma-Aldrich), methanol (HPLC grade, Fisher), (3-amninopropyl)triethoxysilane (APTES, ≥99%, Sigma-Aldrich), N-(3-dimethylaminopropyl)-N′-ethylcarbodiimide hydrochloride (EDC, commercial grade, powder, Sigma-Aldrich), N-hydroxysuccinimide (NHS, 98%, Sigma-Aldrich), cinnamaldehyde (natural, ≥95%, FG, Aldrich), isopropanol (anhydrous, Sigma-Aldrich), and hydrogen (Airgas), were used as received, without further purification. Hydrocinnamaldehyde (≥95%, FG, FCC, Sigma-Aldrich), cinnamyl alcohol (98%, Sigma-Aldrich), hydrocinnamyl alcohol (3-phenyl-1-propanol, 98%, Sigma-Aldrich) were used as standards for LC/MS and GC/MS analysis. Tetradecane (≥99%, Aldrich) was used as an internal standard. Sintered glass filter discs (25 mm diameter, 3.5 mm thick, grade E, Ace Glass) were used as catalyst supports.

Solutions. Potassium phosphate monobasic (ACS reagent, ≥99%, Aldrich), sodium phosphate dibasic heptahydrate (ACS reagent, 98%-102%, Sigma-Aldrich), sodium chloride (ACS reagent, ≥99%, Fisher Chemical), potassium chloride (ACS reagent, ≥99%, Fisher Chemical), sodium hydroxide (ACS reagent, Fisher Chemical), hydrochloric acid (12M, Columbus Chemical Industries) and water (Milli Q) were used to make phosphate buffer (PBS buffer, pH = 7). Piranha solution was made of concentrated sulfuric acid and hydrogen peroxide in a 3:1 volume ratio *(Caution! Strong Oxidizer!)*. Aqua regia was made of concentrated hydrochloride acid and nitric acid with volume ratio of 3:1 *(Caution! Strong Oxidizer!)*. Cinnamaldehyde solutions were made with isopropanol and PBS buffer (pH 7) and both were bubbled with $H_2(g)$ using a gas dispersion tube (fine porosity, Ace Glass).

Palladium nanoparticle synthesis and immobilization. The synthesis of Pd NPs and their immobilization on glass frit catalyst supports has been described in the companion paper.[12] Palladium acetate (0.06g) and biotin (0.2g) were dissolved in methanol (160 mL), stirred and bubbled with $N_2(g)$ for 2 hours in a 500 mL two-neck round bottom flask. The solution was heated to 70 °C for 24 hours under $N_2(g)$.[13] Solvent was removed under vacuum using a rotary evaporator and nanoparticles were precipitated with acetone, then centrifuged at 4500 rpm for eight minutes, then washed in acetone. As-synthesized biotinylated-Pd NPs were re-dispersed in PBS buffer (pH 7).

Flow-through catalytic reaction system. 2mM Cinnamaldehyde solutions were made with isopropanol and PBS buffer (pH 7) and both were bubbled with $H_2(g)$ using a gas dispersion tube (fine porosity, Ace Glass). For each reaction, a glass frit containing immobilized Pd NPs was placed in the Teflon® flow cell and hydrogen gas was used to fill the reaction chamber and glass frit pores. Feedstock solutions were flowed through catalyst-loaded glass frits using a syringe pump (NE-1000 programmable single syringe pump, New Era Pump System Inc.) at a flowrate of 15 μL/min. The eluent was collected every 30 minutes. Reproducibility was evaluated using three repetitions of individual runs.

A two-position microelectric valve actuator (VICI Valco) was used to control periodic input of $H_2(g)$ during the flow-through reaction. The valve was switched to input an aliquot of H_2(g) every 10 minutes. A metering check valve (Swaglok stainless steel low flow metering valve) was installed upstream of reactor chamber to control pressure fluctuations and the flow rate of the feedstock solution.

Sample analysis. Cinnamaldehyde in isopropanol solvent and eluent aliquots were analyzed by GC-MS (Agilent 5975B, 30m VF-5ms column) from 60°C to 350°C at rate of 40°C /min. Cinnamaldehyde in PBS buffer and eluent aliquots were extracted with ethyl acetate and analyzed by GC-MS (Agilent 5975 C, 30m DB-waxetr column) from 60°C to 280°C at rate of 40°C/min.

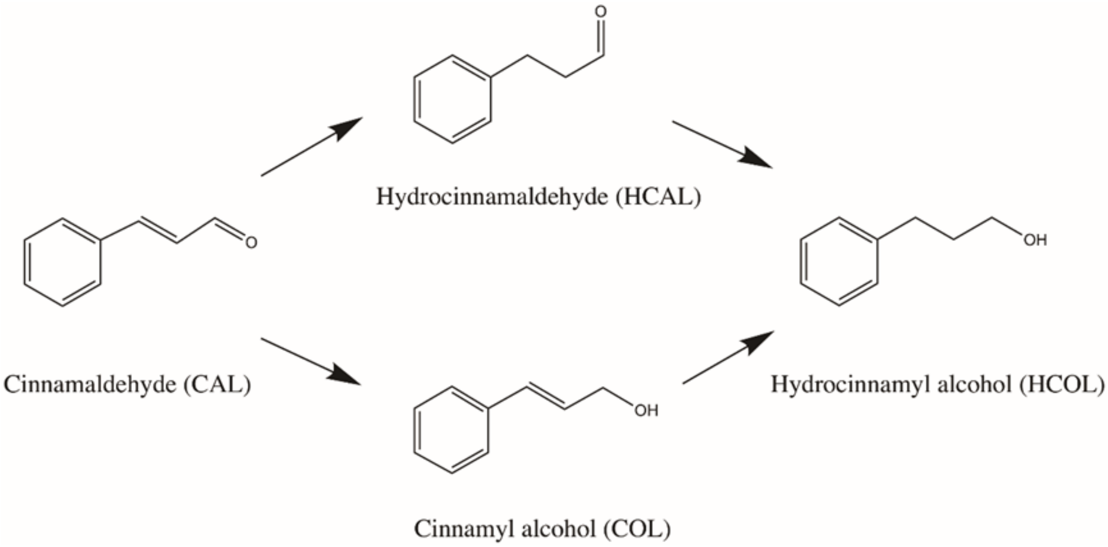

Scheme 0.1 Hydrogenation of cinnamaldehyde to hydrocinnamaldehyde, cinnamyl alcohol and hydrocinnamyl alcohol.

4.9 Results and Discussion

In the companion article, we described in detail the Pd NP synthesis and characterization of morphology, size distribution, thermal properties and composition. The effectiveness of surface immobilization on glass frit supports was demonstrated in that work. We have evaluated this supported catalyst system for activity and selectivity for the catalytic hydrogenation of cinnamaldehyde. We consider the individual reactions below.

4.9.1 Hydrogenation of cinnamaldehyde

The catalytic activity and selectivity of as-synthesized Pd NPs were assessed for the heterogeneous hydrogenation of α,β-unsaturated aldehydes, using cinnamaldehyde as the substrate. A key issue is the ability to demonstrate chemoselective hydrogenation of cinnamaldehyde to hydrocinnimaldehyde, cinnamyl alcohol or hydrocinnamyl alcohol, depending on whether one of the C=C bonds is hydrogenated or the C=O bond is hydrogenated, or if both undergo reaction,[1] as is depicted in Scheme 5.1. Hydrocinnamaldehyde and cinnamyl alcohol are formed via two parallel reaction pathways and the relative selectivity for each pathway depends on the catalyst, the solvent and the reaction conditions. Hydrocinnamyl alcohol is formed consecutively through hydrogenation of both hydrocinnamaldehyde and cinnamyl alcohol, and is a stable reaction product under the reaction conditions.[2] Cinnamaldehyde in either aqueous buffer solvent or isopropanol was flowed through a porous glass catalyst support containing immobilized Pd NP catalyst under ambient conditions. The conversion of cinnamaldehyde was used to evaluate the efficiency of the catalytic reaction. Selectivity for the various possible products was used to evaluate the chemoselective properties of the biotinylated Pd NPs. Conversion for each reaction was defined as

$$Conversion\ (\%) = \frac{moles\ of\ substrate\ consumed}{moles\ of\ substrate\ introduced} \times 100$$

Selectivity toward one of the products was defined as

$$Selectivity\ (hydrocinnamaldehyde, \%) = \frac{moles\ of\ hydrocinnamaldehyde}{total\ moles\ of\ product(s)} ?\,100$$

$$Selectivity\ (cinnamyl\ alcohol, \%) = \frac{moles\ of\ cinnamyl\ alcohol}{total\ moles\ of\ product(s)} \times 100$$

$$Selectivity\ (hydrocinnamyl\ alcohol, \%) = \frac{moles\ of\ hydrocinnamyl\ alcohol}{total\ moles\ of\ product(s)} \times 100$$

The conversion of cinnamaldehyde in phosphate buffer solution is presented in Fig 5.1 as a function of reaction run time. The conversion started at *ca*. 88% and was stable at >90% during 150 min running time. Error bars show the reproducibility of this reaction across three runs for each sample. The selectivity of this reaction toward the various possible products was also evaluated. The selectivity of the reaction for hydrocinnamaldehyde and hydrocinnamyl alcohol is shown in Fig 5.2 as fraction of all products detected. Although 100% selectivity for is single compound was not achievable through this hydrogenation reaction, over 80% selectivity for hydrocinnamaldehyde can be maintained through 150 min of reaction run time.

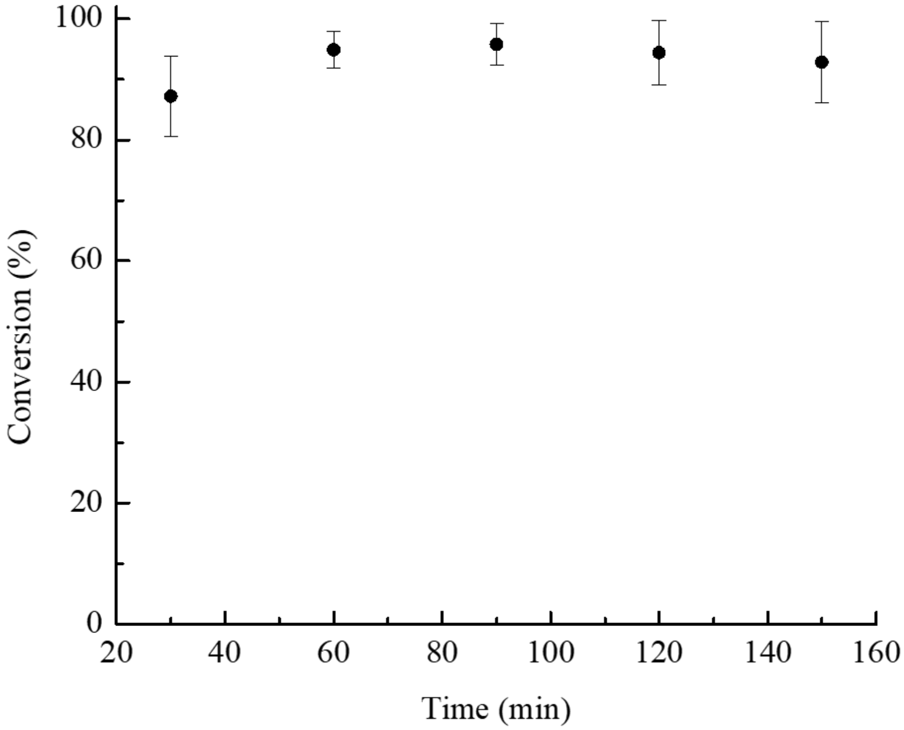

Figure 0.1 Conversion of cinnamaldehyde in phosphate buffer solution as a function of reaction run time.

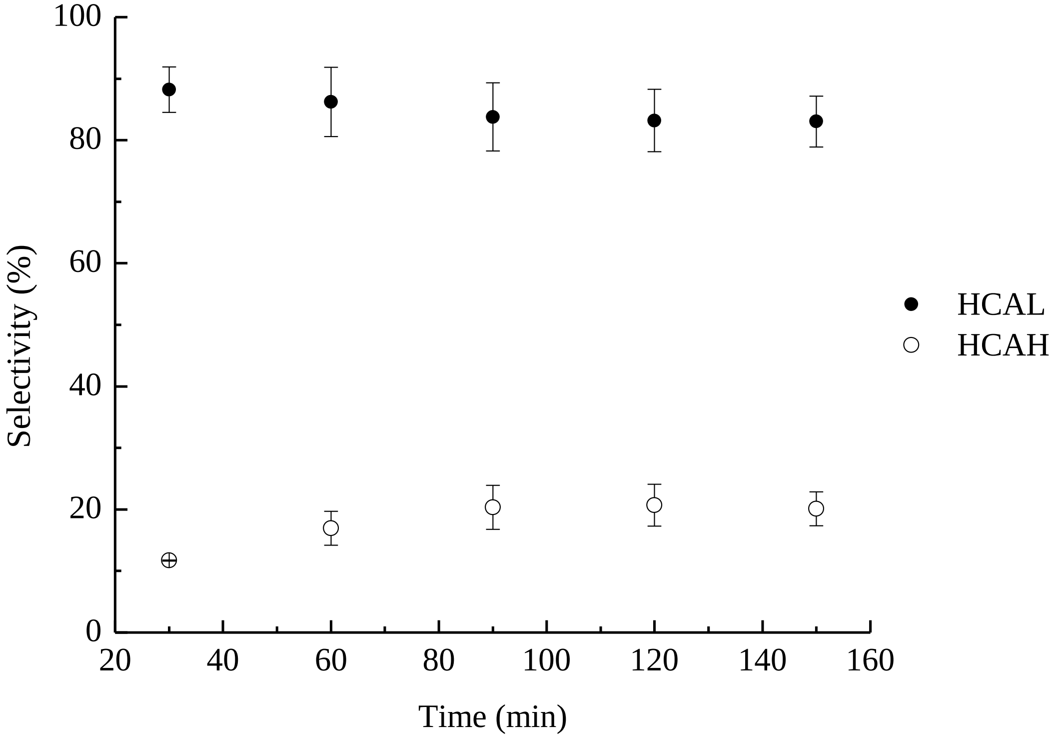

Figure 0.2 Selectivity of the catalytic reaction for hydrocinnamaldehyde (•) and hydrocinnamyl alcohol (o) in phosphate buffer solution as a function of reaction run time.

The selectivity for hydrocinnamyl alcohol started near 90% and then dropped to *ca*. 80% and remained stable at that level. Pd is known to be more prone to hydrogenation of C=C double bonds than C=O bonds, compared to other transition metals.[8] Pd on activated carbon is highly selective in the hydrogenation of cinnamaldehyde to hydrocinnamaldehyde (90% selectivity at 90% cinnamaldehyde conversion).[14] Compared to Pd NPs on activated carbon, the biotinylated Pd NPs on silica is highly active, achieving full conversion more rapidly (30 min flow under ambient conditionsvs. more than 2 hour reaction time).[5] These results underscore the utility of this approach to the immobilization of Pd NPs and this means of performing the reaction.

Comparing our results with the heterogeneous hydrogenation of phenolic compounds using an organic solvent in batch reactor mode under high pressure, we observed that the organic solvent might not be a good choice for hydrogenation reactions in our flow-through reactor under ambient conditions. The activity of biotinylated Pd NPs was investigated with cinnamaldehyde in isopropanol using our flow-through catalyst support at room temperature and atmospheric pressure. Under the same reaction conditions as were used for cinnamaldehyde in phosphate buffer, the reactant solution was saturated with H_2(g) prior to the start of the reaction and no external H_2(g) source was used during the course of the reaction. These results are shown in Fig. 5.3. The conversion of cinnamaldehyde started at *ca*. 60% for the first 30 min aliquot and decreased gradually to 25% over the 150 min reaction run time. The error bars were much larger for this reaction than for the reaction in aqueous buffer (Fig. 5.2). This finding demonstrates a loss of catalyst activity when using isopropanol solvent, which is consonant with the results for p-coumaric acid, reported in the companion paper. In terms of selectivity toward the possible hydrogenation products for the reaction in isopropanol, selectivity for hydrocinnamaldehyde starts at *ca.*70% and increases to 90% (with significant error bars, Fig. 5.4). The hydrogenation products of both the C=C and C=O bonds start at *ca.* 30% and decreased to 20% with increasing reaction run time (Fig. 5.4). Comparing these results to those obtained in aqueous buffer, the hydrogenation products experienced lower reproducibility and conversion in isopropanol than in aqueous buffer. As noted in the companion paper, in the reactor system, O_2(g) is more soluble than H_2(g) in isopropanol, leading to the poisoning of the Pd NP catalyst. In contrast to the heterogeneous hydrogenation reaction performed in a batch reactor at high pressure, our Teflon® flow reactor was not sealed and pressurized with H_2(g). The consequent exposure of the reaction system to O_2(g) may cause the oxidation and deactivation of the Pd NP catalyst during the reaction, leading the conversion to decrease gradually in the absence of an external source of H_2(g). In the companion paper, we also considered the exposure of the Pd NP catalyst to O_2(g) due to dissolution of O_2(g) from air present in the reaction stream.[15] This possibility is supported by gas solubility data from IUPAC-NIST showing that the saturation mole fraction of O_2(g) and H_2(g) in aqueous solution are *ca.* 2.5×10^{-5} and 1.5×10^{-5} under ambient conditions,[16] while in isopropanol the saturation mole fractions of O_2(g) and H_2(g) are7.87×10^{-4} and 2.66×10^{-4}, respectively.[16]

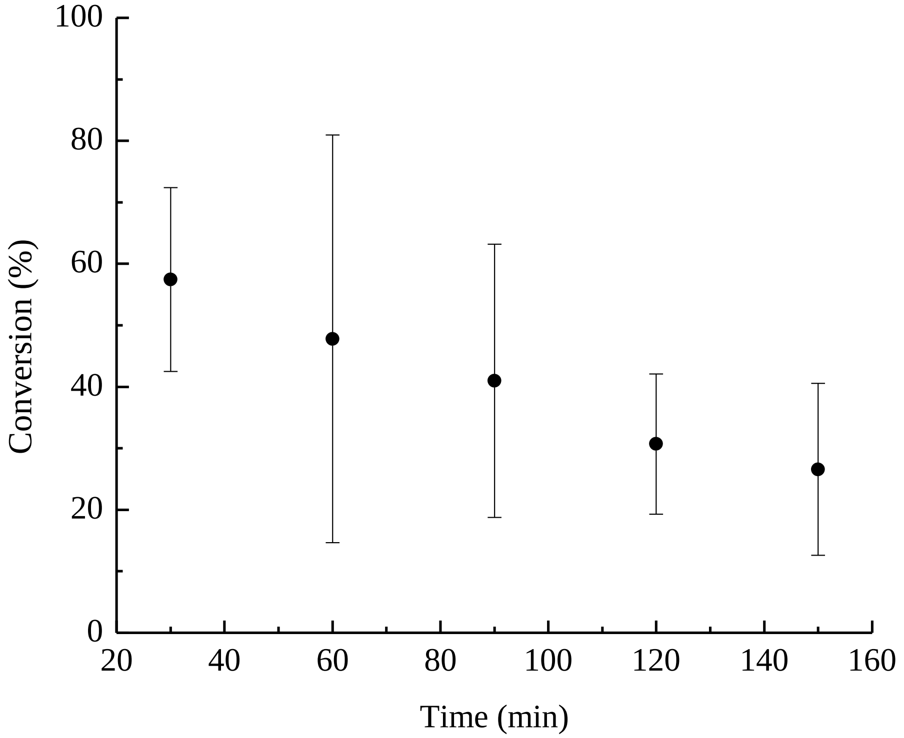

Figure 0.3 Conversion of cinnamaldehyde in isopropanol saturated with H2(g) as a function of reaction run time.

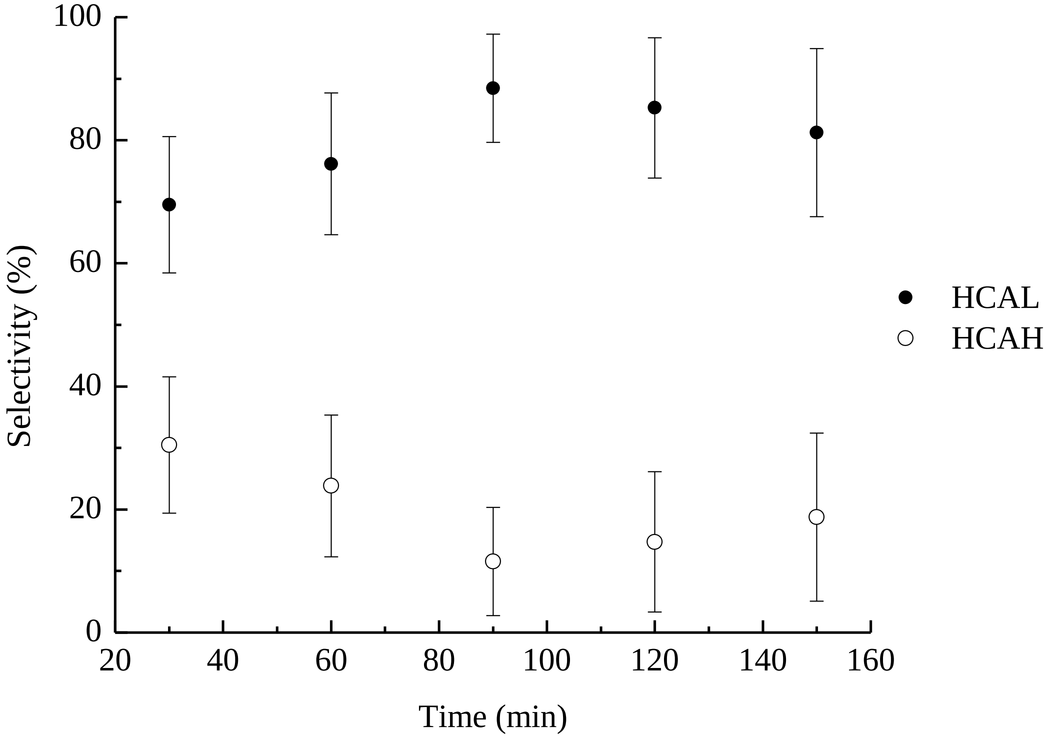

Figure 0.4 Selectivity of the catalytic reaction for hydrocinnamaldehyde (•) and hydrocinnamyl alcohol (o) in isopropanol as a function of reaction run time.

The solubility of oxygen is 31 times higher than hydrogen in isopropanol, and 18 times higher than hydrogen in aqueous buffer. On the surface of the catalyst, the oxidation of active Pd NPs is preferred over the hydrogenation reaction.[17,18]

The poisoning of catalysts is always a challenge for industrial processes. To confirm the hypothesis and address the deactivation issue of the catalysts used here, we introduce an external hydrogen source to the flowing reaction system to protect the catalyst from exposure to oxygen and deactivation. One possible route for Pd NP deactivation during a hydrogenation reaction is the blocking of metallic sites by feedstock components that contain unsaturation(s).[18] However, the reactants contain unsaturations and this potential problem can be minimized by the introduction of H_2(g). The three phase reaction system (H_2(g), liquid reactant flow stream, supported Pd NP catalyst) can be successful with well-regulated delivery of H_2(g).[19] In this work, we have used a a two-position actuator to introduce H_2(g) at regular intervals into the catalytic reaction vessel (Fig. 5.5). The introduction of cinnamaldehyde in isopropanol and H_2(g) was accomplished through two separate entrances (ports **3** and **5** of the switching valve) into the reaction vessel and the outlet was connected to position **4** of the two-position, six-port switching valve. The switching valve dynamically alternates between liquid and gas fluid paths and is controlled electronically. Feedstock solution or H_2(g) flow was chosen via manual selection between positions **A** or **B** of the controller. Through port **4**, the combined

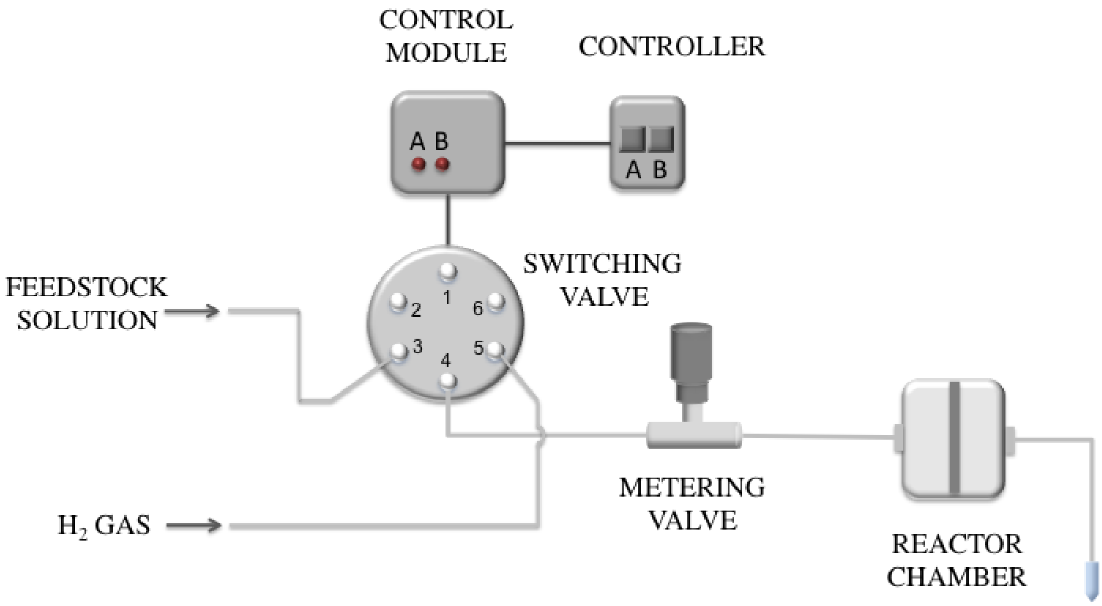

Figure 0.5 Flow system schematic showing a two-position electronically actuated control module. H2(g) and reactant feedstock solution was introduced at intervals into the system by controlling the two-position six-port switching valve. Gas flow was controlled using a pressure regulator and metering valve.

liquid and gas reactant stream flows through a metering valve to stabilize the flow rate, and the heterogeneous hydrogenation reaction occurs in the reactor chamber. Collected aliquots were analyzed using the same methods reported previously (*vide infra*). Fig. 5.6 shows the conversion of cinnamaldehyde in isopropanol over biotinylated Pd NPs as a function of reaction time. The conversion of cinnamaldehyde started around 93% and remained greater than 80% during the 150 min reaction time. In comparison, the reaction of cinnamaldehyde in isopropanol without the use of the two-position microelectric actuator system is shown in Fig. 5.7. Although the detected products of hydrocinnamaldehyde and hydrocinnamyl alcohol (Fig. 5.8) maintained the same level of selectivity (*ca.* 82% and 18%, respectively) for both reaction conditions, results are more reproducible with external $H_2(g)$ input. The introduction of $H_2(g)$ flow through reaction system prevented the exposure of the Pd NP catalyst to oxygen, slowing the deactivation of the catalyst. We note that the presence of $H_2(g)$, introduced in this manner, also served to maintain a sufficient reactant concentration to ensure relatively efficient catalytic conversion.

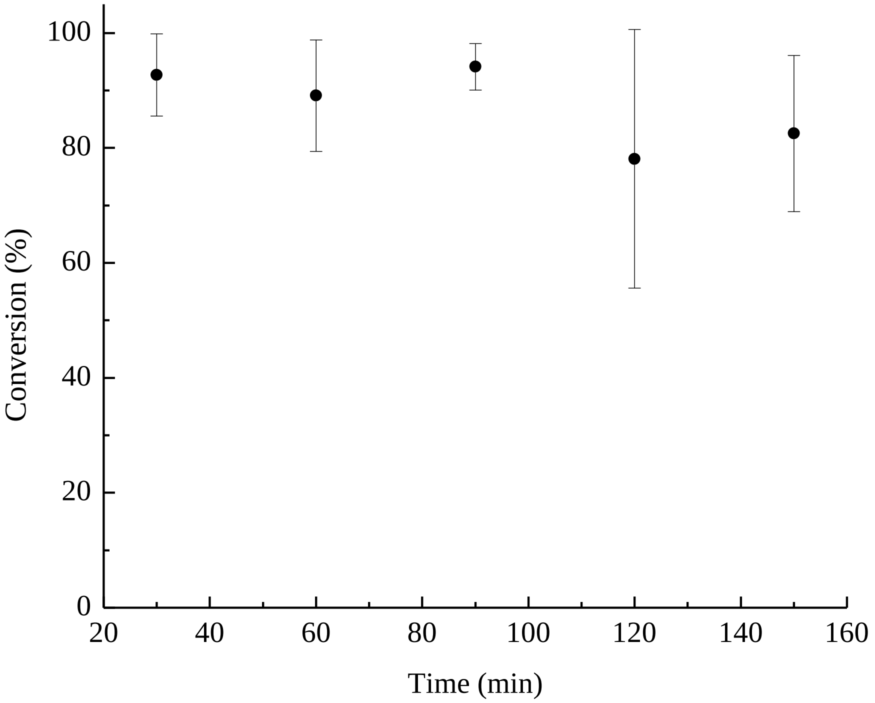

Figure 0.6 Conversion of cinnamaldehyde in isopropanol using the two-position control valve to introduce H2(g) at periodic intervals.

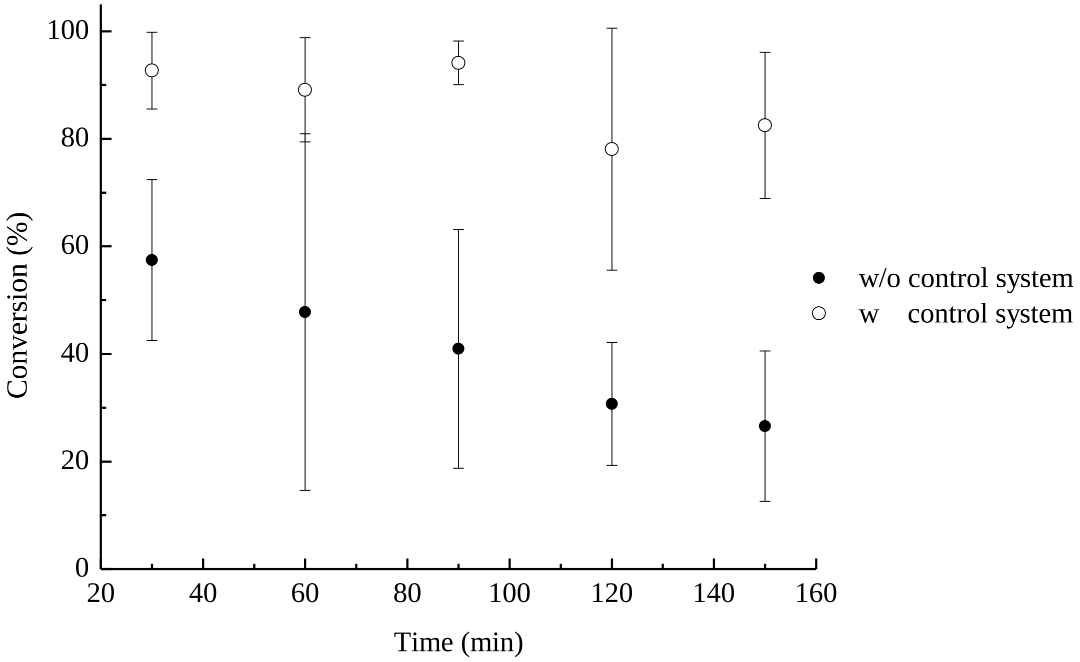

Figure 0.7 Comparison of conversion in isopropanol for use of the H2(g) control system to the reaction where H2(g) introduction does not occur at regular intervals.

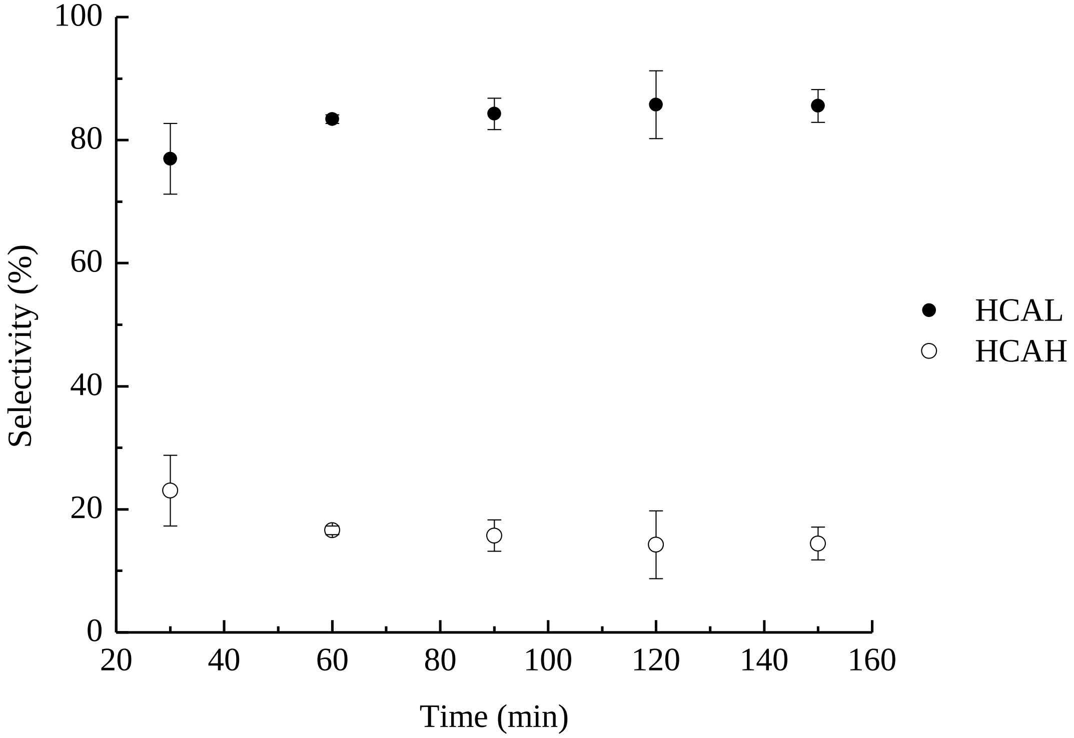

Figure 0.8 Selectivity for hydrocinnamaldehyde (•) and hydrocinnamyl alcohol (o) in isopropanol using the two-position control to introduce H2(g) at periodic intervals.

4.10 Conclusion

We have demonstrated that biotinylated Pd NPs can be immobilized on a glass frit support and used as the catalyst for heterogeneous hydrogenation reactions in a flowing reaction mode. The catalytic activity of the Pd NP catalyst was investigated to determine the conversion of cinnamaldehyde in aqueous buffer solution and isopropanol to its reaction intermediates (hydrocinnamyldehyde, cinnamyl alcohol and hydrocinnamyl alcohol). We found that the reaction efficiency differed with the identity of the solvent, and that the Pd NP catalyst was deactivated in isopropanol under ambient conditions in the flow-through reactor, likely due to oxygen exposure. The selectivity of the reaction for hydrocinnamaldehyde and hydrocinnamyl alcohol was 80% and 20 %, respectively in both aqueous and alcohol solvents. A two-position electronic actuator control system was used to maintain H_2(g) concentration in the isopropanol solvent system and thereby reduce the extent of catalyst degradation during the course of the reaction. The introduction of an external source of H_2(g) into the flowing reactant stream minimized catalyst deactivation during the course of the reaction. We anticipate that this work will be useful in demonstrating a useful approach to the protection of NP catalyst systems in flow-reactor systems.

REFERENCES

REFERENCES

1. Gallezot, P.; Richard, D., Selective Hydrogenation of α,β-Unsaturated Aldehydes. *Catal. Rev.* **1998,** *40* (1-2), 81-126.

2. Zhang, L. Q.; Winterbottom, J. M.; Boyes, A. P.; Raymahasay, S., Studies on the hydrogenation of cinnamaldehyde over Pd/C catalysts. *J. Chem. Tech. Biotech.* **1998,** *72* (3), 264-272.

3. Nagpure, A. S.; Gurrala, L.; Gogoi, P.; Chilukuri, S. V., Hydrogenation of cinnamaldehyde to hydrocinnamaldehyde over Pd nanoparticles deposited on nitrogen-doped mesoporous carbon. *RSC Advances* **2016,** *6* (50), 44333-44340.

4. Mäki-Arvela, P.; Hájek, J.; Salmi, T.; Murzin, D. Y., Chemoselective hydrogenation of carbonyl compounds over heterogeneous catalysts. *Appl. Cat. A. General* **2005,** *292*, 1-49.

5. Tessonnier, J. P.; Pesant, L.; Ehret, G.; Ledoux, M. J.; Pham-Huu, C., Pd nanoparticles introduced inside multi-walled carbon nanotubes for selective hydrogenation of cinnamaldehyde into hydrocinnamaldehyde. *Appl. Cat. A. General* **2005,** *288* (1-2), 203-210.

6. Ma, H. X.; Wang, L. C.; Chen, L. Y.; Dong, C.; Yu, W. C.; Huang, T.; Qian, Y. T., Pt nanoparticles deposited over carbon nanotubes for selective hydrogenation of cinnamaldehyde. *Catal. Commun.* **2007,** *8* (3), 452-456.

7. Coq, B.; Kumbhar, P. S.; Moreau, C.; Moreau, P.; Warawdekar, M. G., Liquid phase hydrogenation of cinnamaldehyde over supported ruthenium catalysts: Influence of particle size, bimetallics and nature of support. *J. Mol. Cat.* **1993,** *85* (2), 215-228.

8. Rylander, P. N., 14 - Hydrogenation of Aldehydes. In *Catalytic Hydrogenation Over Platinum Metals*, Academic Press: 1967; pp 238-257.

9. Mandal, S.; Roy, D.; Chaudhari, R. V.; Sastry, M., Pt and Pd nanoparticles immobilized on amine-functionalized zeolite: Excellent catalysts for hydrogenation and Heck reactions. *Chem. Mater.* **2004,** *16* (19), 3714-3724.

10. Kume, Y.; Qiao, K.; Tomida, D.; Yokoyama, C., Selective hydrogenation of cinnamaldehyde catalyzed by palladium nanoparticles immobilized on ionic liquids modified-silica gel. *Catal. Commun.* **2008,** *9* (3), 369-375.

11. Su, J.; Chen, J. S., Synthetic porous materials applied in hydrogenation reactions. *Microporous Mesoporous Matls* **2017,** *237*, 246-259.

12. Zhang, X.; Blanchard, G. J., Demonstration of Flow-Through Catalytic Reactions using a Porous Silica Support: Reduction of p-Coumaric Acid. *Phys. Chem. Chem.*

Phys. **2017,** *in review (companion manuscript).*

13. Lin, R.; Freemantle, R. G.; Kelly, N. M.; Fielitz, T. R.; Obare, S. O.; Ofoli, R. Y., *In situ* immobilization of palladium nanoparticles in microfluidic reactors and assessment of their catalytic activity. *Nanotech.* **2010,** *21* (32).

14. Cabiac, A.; Cacciaguerra, T.; Trens, P.; Durand, R.; Delahay, G.; Medevielle, A.; Plee, D.; Coq, B., Influence of textural properties of activated carbons on Pd/carbon catalysts synthesis for cinnamaldehyde hydrogenation. *Appl. Cat. A. General* **2008,** *340* (2), 229-235.

15. Bartholomew, C. H., Mechanisms of catalyst deactivation. *Appl. Cat. A. General* **2001,** *212* (1-2), 17-60.

16. Clever, H. L.; Battino, R.; Miyamoto, H.; Yampolski, Y.; Young, C. L., IUPAC-NIST Solubility Data Series. 103. Oxygen and Ozone in Water, Aqueous Solutions, and Organic Liquids (Supplement to Solubility Data Series Volume 7). *J. Phys. Chem. Ref. Data* **2014,** *43* (3).

17. de Souza, P. M.; Rabelo-Neto, R. C.; Borges, L. E. P.; Jacobs, G.; Davis, B. H.; Resasco, D. E.; Noronha, F. B., Hydrodeoxygenation of Phenol over Pd Catalysts. Effect of Support on Reaction Mechanism and Catalyst Deactivation. *ACS Catal.* **2017,** *7* (3), 2058-2073.

18. Marafi, M.; Furimsky, E., Hydroprocessing Catalysts Containing Noble Metals: Deactivation, Regeneration, Metals Reclamation, and Environment and Safety. *Energy & Fuels* **2017,** *31* (6), 5711-5750.

19. Kobayashi, J.; Mori, Y.; Okamoto, K.; Akiyama, R.; Ueno, M.; Kitamori, T.; Kobayashi, S., A microfluidic device for conducting gas-liquid-solid hydrogenation reactions. *Science* **2004,** *304* (5675), 1305-1308.

CHAPTER 6: Conclusion and future work

5.1 Overall Conclusions

The use of biomass in place of fossil fuels as a source of energy is attractive for a number of reasons.[1] The key to making such a transformation is the ability to take a range of oxidized organic species and perform sequential, selective reduction reactions on them to ultimately render hydrocarbon(s). Such a transformation requires the creation of a functional bio-refinery.[2] The goal of this project has been to develop and evaluate a catalytic platform for hydrogenation in a flow-through reaction format, a key step in comprehensive biomass conversion and processing. By integrating nanotechnology, colloid chemistry and heterogeneous catalysis, we have demonstrated efficient and selective flow-through catalytic reactions using an enzyme or metal nanoparticles as the catalyst material. The work touched on several elements central to the development of a catalytic system, including catalyst design and synthesis, support design and synthesis, and the characterization of all the materials and reaction products. Ultimately the aim of this work is to produce catalyst-containing porous "cassettes" that can be placed in a flow-through reaction configuration to perform high efficiency, specific reaction sequences. The demonstration of viable supported catalyst systems capable of reacting in multi-phase environments is the foundation for the creation of a flow-through bio-refinery system.

Following the background and introduction in Chapter 1, Chapter 2 considers the issues associated with the formation of silica inverse opal catalyst support structures and the development a composite polymer-silica sol gel matrix for the formation of inverse opal materials with comparatively low defect density. Chapter 3 reports on the use of porous glass frit supports for flow-through catalysis and comparing its functionality to that of inverse opal structures reported by Gornowich, using an immobilized enzyme catalyst.[3] Chapter 4 describes the synthesis and characterization of Pd nanoparticle for use as a catalyst and the immobilization of these NPs onto a porous glass frit support. The assessment of catalytic performance was made with the heterogeneous hydrogenation of p-coumaric acid and cinnamaldehyde in both organic and aqueous solution, as reported in Chapter 4 and Chapter 5, respectively. The primary results of the entire work are discussed briefly in this chapter.

The formation of a colloidal nanosphere template for the creation of inverse opal structures has been demonstrated for a variety inorganic oxides and composites, and each type has been used in different applications, depending on the desired composition of the resulting inverse opal.[4-5] Silica sol gel-based inverse opal structures are typically limited by the presence of structural defects and cracks formed during the matrix curing and drying steps.[6] These structural defects are thought to occur as a result of changes in the matrix material dimensions upon condensation to form the solid matrix. To overcome this problem, we created low defect hybrid inverse opal structures by adding a polymer to the curing silica matrix. The morphology of the resulting inverse opal depends on both the amount of polymer and its molecular weight.[7]

Inverse opal structures are attractive from a structural perspective in terms of the formation of uniform void and pore sizes and locations, but this class of materials suffers from two serious limitations. These are the propensity to form crack and large defect structures during formation, and the lack of physical robustness of the structure, once formed. Because inverse opal materials are not sufficiently robust to be generally useful catalyst supports, we compared their function as catalyst supports for glucose oxidase

(GOx) to the function of physically robust porous glass frits as GOx supports.[3] It was demonstrated that porous glass frit supports overcome the limitations intrinsic to inverse opal supports while yielding the same reaction efficiency. With the utility of porous glass frits as catalyst supports, we evaluated these materials for their utility in supporting metal nanoparticle catalysts. We synthesized and characterized colloidal Pd nanoparticles with well-defined morphology. Monodisperse biotinylated-Pd nanoparticles were characterized as having a predominantly face-centered cubic crystal structure with an average diameter of 3 nm and bound to the porous glass frit surface. This supported catalyst was used for heterogeneous hydrogenation in a liquid phase reactant stream under ambient conditions. The catalytic hydrogenation reactions of p-coumaric acid and cinnamaldehyde were characterized in aqueous and organic solvent systems. The reaction efficiency depended on the identity of the solvent, and Pd NPs were deactivated in isopropanol solvent in the flow-through reactors, likely due to exposure to oxygen. This limitation can be addressed through the use of a two-position microelectric actuator control system to maintain a somewhat more uniform $H_2(g)$ concentration in the reactant stream.

In summary, the nanoparticle catalysts incorporated into robust porous glass frits showed high catalytic activities for hydrogenation in a flow-through liquid phase reaction under ambient conditions. This is an essential first step in the creation of a bio-refinery system for biofeedstock conversion to hydrocarbons.

5.2 Future directions

While this work illustrated the utility of Pd NPs confined within porous oxide frits for the flow-through hydrogenation required for biomass conversion, there is clearly more work to do in terms of enhancing the catalytic efficiency and selectivity of these systems for specific classes of elementary reactions, such as deoxygenation and decarboxylation. To perform catalytic reactions needed for biomass conversion, bimetallic nanoparticles will likely find use and the exploration of this family of materials is a logical next step. Specifically, the comparison of bimetallic NPs to monometallic NPs in terms of reactions performed, and efficiency will be of critical importance.[8] Alloying two metals is known to produce nanoparticles with catalytic properties that differ from those of monometallic nanoparticles.[9] In the bimetallic nanoparticle, the atomic-level mixing and segregation will occur in such a way as to minimize the surface energy and internal strain.[10] Particle size, shape and composition, and the choice of stabilizing agent are all expected to play a role in the catalytic properties of the resulting system, and catalyst support identity as well as solvent identity will affect the catalytic performance of bimetallic nanoparticles, just as has been observed for monometallic nanoparticles.[9, 11] All of these parameters remain to be explored.

The synthesis of bimetallic nanoparticles has a rich literature.[12-14] Based on this body of knowledge, the initial choices for bimetallic nanoparticle synthesis will likely require techniques such as co-reduction, thermal decomposition and seeded-growth. Solution-based nanoparticle synthesis will be controlled by conditions such as reactant concentration and ratio, choice of stabilizing ligand, reaction temperature and time.[8, 10] The catalytic properties of the resulting bimetallic nanoparticles will be evaluated in the flow-through heterogeneous catalytic system developed in this dissertation, and it is anticipated that the specific choice of nanoparticle catalyst will determine the ability to perform reactions in the bio-refinery system that are not presently feasible using monometallic nanoparticles.

By optimizing the catalytic efficiency and selectivity of elementary reactions, the proposed flow-through catalytic reaction system will enable the conversion of biomass feedstocks to hydrocarbons.

REFERENCES

REFERENCES

1. Cherubini, F., The biorefinery concept: Using biomass instead of oil for producing energy and chemicals. *Energy Conversion and Management* **2010,** *51* (7), 1412-1421.

2. Maity, S. K., Opportunities, recent trends and challenges of integrated biorefinery: Part I. *Renewable and Sustainable Energy Reviews* **2015,** *43*, 1427-1445.

3. Gornowich, D. B.; Blanchard, G. J., Enhancement of Enzyme Activity by Confinement in an Inverse Opal Structure. *J Phys Chem C* **2012,** *116* (22), 12165-12171.

4. Holland, B. T.; Blanford, C. F.; Do, T.; Stein, A., Synthesis of Highly Ordered, Three-Dimensional, Macroporous Structures of Amorphous or Crystalline Inorganic Oxides, Phosphates, and Hybrid Composites. *Chemistry of Materials* **1999,** *11* (3), 795-805.

5. Holland, B. T.; Blanford, C. F.; Stein, A., Synthesis of Macroporous Minerals with Highly Ordered Three-Dimensional Arrays of Spheroidal Voids. *Science* **1998,** *281* (5376), 538-540.

6. Hench, L. L.; West, J. K., The sol-gel process. *Chemical Reviews* **1990,** *90* (1), 33-72.

7. Zhang, X.; Blanchard, G. J., Polymer Sol–Gel Composite Inverse Opal Structures. *ACS Applied Materials & Interfaces* **2015,** *7* (11), 6054-6061.

8. Toshima, N.; Yonezawa, T., Bimetallic nanoparticles-novel materials for chemical and physical applications. *New Journal of Chemistry* **1998,** *22* (11), 1179-1201.

9. An, K.; Somorjai, G. A., Nanocatalysis I: Synthesis of Metal and Bimetallic Nanoparticles and Porous Oxides and Their Catalytic Reaction Studies. *Catalysis Letters* **2015,** *145* (1), 233-248.

10. Wang, D.; Li, Y., Bimetallic Nanocrystals: Liquid-Phase Synthesis and Catalytic Applications. *Advanced Materials* **2011,** *23* (9), 1044-1060.

11. Dang-Bao, T.; Pla, D.; Favier, I.; Gómez, M., Bimetallic Nanoparticles in Alternative Solvents for Catalytic Purposes. *Catalysts* **2017,** *7* (7), 207.

12. Papa, F.; Negrila, C.; Miyazaki, A.; Balint, I., Morphology and chemical state of PVP-protected Pt, Pt–Cu, and Pt–Ag nanoparticles prepared by alkaline polyol method. *Journal of Nanoparticle Research* **2011,** *13* (10), 5057.

13. Shore, M. S.; Wang, J.; Johnston-Peck, A. C.; Oldenburg, A. L.; Tracy, J. B., Synthesis of Au(Core)/Ag(Shell) Nanoparticles and their Conversion to AuAg Alloy Nanoparticles. *Small* **2011,** *7* (2), 230-234.

14. Xia, B.; He, F.; Li, L., Preparation of Bimetallic Nanoparticles Using a Facile Green Synthesis Method and Their Application. *Langmuir* **2013,** *29* (15), 4901-4907.